



COPYRIGHTED BY

Tania Mukherjee

April, 2013

**Time-lapse scenario modeling and VSP analysis for an EOR reservoir in  
Oman**

---

A Dissertation

Presented to

the Faculty of the Department of Earth and Atmospheric Sciences

University of Houston

---

In Partial Fulfillment

of the Requirements for the Degree

Doctor of Philosophy

---

By

Tania Mukherjee

April, 2013

# **Time-lapse scenario modeling and VSP analysis for an EOR reservoir in Oman**

---

Tania Mukherjee

APPROVED:

---

Dr. Robert R. Stewart, Supervisor  
Department of Earth and Atmospheric Sciences

---

Dr. John P. Castagna  
Department of Earth and Atmospheric Sciences

---

Dr. Robert Wiley  
Department of Earth and Atmospheric Sciences

---

Dr. Albena Mateeva  
Shell International Exploration and Production Inc.

---

Dean, College of Natural Sciences and Mathematics

## **Acknowledgements**

Dr. Robert Stewart, my dissertation supervisor, guided me throughout the process, corrected my mistakes, and showed me the right way. I sincerely thank him for his guidance and support. I appreciate his patient proofreading of this dissertation.

I thank Albena Mateeva for her technical input, ideas, and suggestions. I thank Dr. John Castagna and Dr. Robert Wiley for useful comments, suggestions, and encouragement in my study. I want to also extend my gratitude to Kurang Mehta for his valuable technical suggestions.

I thank Shell International Exploration & Production, Inc. who sponsored my research and provided the data, tools, and financial support to complete my research. I would like to especially thank Jorge Lopez from Shell for his utmost involvement, support, and interest in this project. I want to mention my regards to Denis Kiyanshchenko for his technical input in processing. Special regards to Paul Hatchel for his time-lapse attribute codes and notes, which I found very useful.

I sincerely thank PDO and the Oman Ministry of Oil and Gas for the general collaboration on reservoir surveillance with Shell and their kind permission to publish this work.

I thank all AGL members for their consistent help and support.

I find myself very lucky to have Prasenjit, my fiancée, who always was very patient and kind, and reminded me of the goodness of life when I was not at my best. He motivated me constantly and happily read and edited my dissertation.

I thank my friends here who make me feel “home away from home” and made my Ph.D. journey into a rewarding one.

Finally, but most importantly, I thank my parents and my brother for their encouragement, support, and confidence in me during my Ph.D. study. Without their encouragement, the completion of my dissertation would not have been possible.

**Time-lapse scenario modeling and VSP analysis for an EOR reservoir in  
Oman**

---

An Abstract of a Dissertation

Presented to

the Faculty of the Department of Earth and Atmospheric Sciences

University of Houston

---

In Partial Fulfillment

of the Requirements for the Degree

Doctor of Philosophy

---

By

Tania Mukherjee

April, 2013

## ABSTRACT

Extensive reservoir modeling analysis and VSP processing are undertaken for a pilot steam injection project in Oman to understand the relationship between reservoir properties and seismic properties and how that changes with steam injection. Effects of different permeability distributions in steam-flooded reservoir models are analyzed in terms of their seismic response. A full-wave walkway time-lapse VSP is designed and processed to investigate possible 4D anomalies. Fluid substitution modeling (Gassmann's substitution) is used to calculate modified petrophysical properties after initial steam injection. Prediction results in a 5 percent lower  $V_p$  and 2 percent lower density. Predicted modifications in petrophysical parameters are sufficient to produce observable 4D effects in PP VSP. Time-lapse anomalies get enhanced when the near-surface VSP data are excluded. In this case, multiple and shear-wave suppression may actually compromise the observed 4D effects. Use of the muted upgoing wave-field for migration enhances the 4D amplitudes, but compromises the lateral resolution. The predicted PP time-lapse results and time-lapse attribute maps are similar to real field VSP results. The PS reflections in the present case are restricted to produce any measurable changes (for smaller angle gathers). I predict that a 6 percent decrease in density (due to steam saturation) may be sufficient for the Oman oil field to produce measurable changes in both PP and PS amplitudes for walkway VSP.

# CONTENTS

Acknowledgements.....	iii
Abstract.....	vi
Contents.....	vii
List of Tables.....	xi
List of Figures.....	xii

## **Chapter One: Introduction**

1.1 Motivation and objectives.....	1
1.2 VSP.....	4
1.3 Study area and geology and field development.....	6
1.4 Previous work.....	12
1.4.1 Steam injection.....	12
1.4.2 Time-lapse 3DVSP.....	15
1.5 Scope of modeling and synthetic studies.....	20
1.6 Modeling software processing and interpretation software.....	21
1.7 Dissertation outline.....	21

## **Chapter Two: Rock physics**

2.1 Introduction.....	23
2.2 The reservoir.....	28
2.3 Well logs and temperature logs.....	30
2.4 Velocity and density change after steam injection.....	34
2.5 Lambda-Mu-Rho plot.....	36

2.6	Rock and fluid model.....	38
2.7	Fluid properties.....	38
2.8	Rock velocities as function of density.....	41

### **Chapter Three: “Closing the Loop” for reservoir model update**

3.1	Introduction .....	43
3.2	Methodology.....	47
3.2.1	Import model .....	47
3.2.2	Import horizons, wells, and real surface seismic data.....	48
3.2.3	Add realistic overburden/underburden .....	48
3.2.4	Insert fluid and rock properties.....	48
3.2.5	Resample , depth-to-time conversion, and generate synthetic seismic.....	49
3.3	Description and analysis of scenarios .....	50
3.4	Time-lapse attributes and analysis.....	58
3.5	Comparison between scenarios.....	62
3.6	Results and conclusions.....	72

### **Chapter Four: Processing and interpretation of PP walkaway VSP model data**

4.1	Introduction.....	73
4.2	WFD models for walkaway VSP.....	73
4.3	Model generation .....	74
4.4	VSP acquisition geometry.....	77
4.5	Zero-offset VSP processing .....	80

4.6	Time shifts.....	87
4.7	TL analysis.....	87
4.8	VSP Imaging for baseline and monitor.....	88
4.9	TL attributes.....	96
4.10	Modified VSP flow for TL processing.....	98
4.11	Ray tracing .....	99
4.12	Results and interpretation .....	100

## **Chapter Five: PS reflectivity analysis for steam induced layering**

5.1	PP and PS in steam flood zones.....	103
5.2	PS reflections in walkway synthetic VSP.....	104
5.3	Theoretical reflectivity analysis (PP and PS).....	106
5.4	Factors that controls PS reflections.....	111
5.5	Two-layer elastic modeling for theoretical validation.....	111
	5.5.1 Modeling parameter.....	112
	5.5.2 Data description and event identification.....	114
	5.5.3 Data preparation to extract amplitudes.....	115
	5.5.4 Theoretical validation.....	119
5.6	Three-layer steam modeling with variable steam thickness.....	120
5.7	Three-layer steam modeling with variable steam saturation and steam width.....	122
5.8	Amplitude as a function of shot offset.....	123
5.9	Interpretation.....	127

5.10 Summary.....	128
<b>Chapter Six: Conclusions and recommendations.....</b>	<b>130</b>
<b>References .....</b>	<b>136</b>
<b>Appendix A: Lateral Fresnel zone calculation of PS VSP.....</b>	<b>142</b>

## LIST OF TABLES

Table 1.1:	Classification of EOR methods. Highlights show commercially successful methods (Ali and Thomas, 1994).....	11
Table 2.1:	Petrophysical parameters from the reservoir.....	29
Table 2.2:	Oil properties of “A” field, Oman.....	39
Table 4.1:	WFD modeling flow to generate seismic data .....	74
Table 4.2:	Acquisition geometry of VSP.....	77
Table 4.3:	Standard VSP processing flow for corridor stack.....	81
Table 5.1:	Two-layer modeling parameters.....	109
Table 5.2:	VSP acquisition parameters for PS modeling.....	113
Table 5.3:	Fluid properties used inputs of Gassmanns substitution.....	121

## LIST OF FIGURES

Figure 1.1:	Schematic diagram of a VSP survey (DiSiena et al., 1984).....	5
Figure 1.2:	Location map of the he “A” in south Oman ( <a href="http://www.map.com">www.map.com</a> ).....	7
Figure 1.3:	Stratigraphic column in field "A".....	8
Figure 1.4:	EOR target for different hydrocarbons (Thomas, 2008).....	8
Figure 1.5:	Conceptual section of the steam flood process.....	9
Figure 1.6:	Pattern design in field "A". The hexagon at the bottom right represents the first pattern (1P).....	10
Figure 1.7:	Steam injection profile in the first pattern. The fifteen month time-lapse monitoring period is shaded .....	14
Figure 1.8:	Graph showing the first pattern shape and well locations. In red are the maximum temperatures recorded at the time of the monitor survey in July 2010. Dotted blue lines show the location of the cross-well seismic profiles.....	14
Figure 1.9:	The surface seismic image (left), the 3DVSP images obtained after interferometric deconvolution (middle) and space-domain up-down deconvolution (right). All are plotted along southeast-northwest cross-well profile. Green (resp. blue) lines are density (resp. P-wave velocity) logs (Kiyashchenko and Maamari, 2010).....	16

Figure 1.10: 3DVSP baseline (left) and difference (right) images (with well projections) for east-west traverse crossing the pattern .....18

Figure 1.11: RRR map at the top Haradh reservoir level. White circles are cold wells and red ones are hot. Red arrows indicate the anomaly extent interpreted from cross-well tomography and white ones from cross-well reflection images; b) the top Haradh relief; and, c) a wedge-type geometry visible with the cross-well seismic image for north-south profile (Kiyashchenko et al., 2011).....19

Figure 2.1: Concept of temperature dependence of P- and S-wave velocities of heavy oil at two different frequencies: ultrasonic and low. The temperature dependence can be approximately described by three main stages; liquid, quasi-solid, and solid states (after Han et al., 2008).....26

Figure 2.2: Ultrasonic P- and S-wave velocities of the heavy oils as a function of temperature. The color corresponds to the API gravity (after Kato, 2010).....27

Figure 2.3: An idealized model of steam-flood fluid flow (left). A rapid high-pressure cold front is expected to lead the injector flow, trailed by hot oil, hot water and hot steam zones. The relative dimensions of each zone may not be to scale, and complexities such as mixed phases and gravity overrides are neglected. Right graph showed predicted steam-flood P-wave velocity

	changes compared to initial reservoir conditions as a function of dimensionless radial distance (after Lumley, 1995).....	27
Figure 2.4:	P- and S-wave velocities and VP/VS changes caused by the steam injection in heavy oil reservoir (After Kato et al., 2008).....	28
Figure 2.5:	Structural map showing the Haradh Formation that went under EOR (western structural high in the X-section) in yellow (Shell internal reports).....	30
Figure 2.6:	Well log from injector showing gamma, density and velocity (compressional and shear) velocities .....	31
Figure 2.7:	$V_P$ versus $V_S$ crossplot. Red cluster is the EOR target .....	32
Figure 2.8:	$V_P / V_S$ versus Gamma crossplot. The yellow cluster is the EOR target. The shale intervals (1000-1030 m and 1030-1060 m) show a wide range of scatter.....	32
Figure 2.9:	Temperature profiles from the observation wells showing differential temperatures over the months. The first two wells showed temperature rise within the reservoir, whereas another well (situated south of the injector) remained cold. ....	33

Figure 2.10:	Compressional and shear velocity log before (marked as baseline) and computed velocities after (marked as monitor) steam injection.....	35
Figure 2.11:	Change in $V_P/V_S$ due to steam injection. Monitor velocities are computed from the baseline velocities, which are measured at the injector before steam injection .....	36
Figure 2.12:	LMR plots for the injector well. Target zone is plotted again after recalculating with changed parameters due to steam.....	37
Figure 2.13.a:	Brine properties as a function of temperature and pressure.....	39
Figure 2.13b:	Oil properties as a function of temperature and pressure .....	40
Figure 2.13c:	Properties of fresh water and steam as a function of temperature and pressure.....	40
Figure 2.14:	Crossplot of velocity versus density for the oil bearing zone (upper panel) and water bearing zone (lower panel). Equations used are $V_P = +5477.116 * \text{density} - 9074.37$ and $V_P = 5477.116 * \text{density} - 9074.34$ . .....	42
Figure 3.1:	Schematic diagram of “Closing-the-Loop” flowchart.....	44
Figure 3.2:	The steam injection pattern outline: ‘P’ is producer wells; ‘O’ is observation wells; and ‘I’ is injector well. Red indicates hot wells at the time of monitor surveys. ....	46

Figure 3.3:	Temperature profiles and maps of Reference Model for two time vintages: a) temperature profile for baseline 2009; b) map view of temperature for baseline 2009 at the reservoir level; c) temperature profile for monitor 2010; and, d) map view of temperature for 2010 monitor at the reservoir level.....	47
Figure 3.4:	Different $K_v/K_h$ gives rise to top thick or thin permeability distribution in the reservoir.. ..	50
Figure 3.5:	Temperature profiles and maps for two time stamps (baseline and monitor) for all scenarios labeled as S2 to Sb. We observe how the shape of steam changes for different permeability distributions .....	53
Figure 3.6:	Oil saturation profiles and maps for two time stamps (baseline and monitor) for all scenarios labeled as S2 to Sb. We note how steam replaces oil as time increases.. ..	54
Figure 3.7:	Acoustic impedance profiles and maps for two time stamps (baseline and monitor) for all scenarios labeled as S2 to Sb. As velocity and density changes with steam, the AI is changed .....	55
Figure 3.8:	Figure 3.9: Difference of seismic data (baseline - monitor). The reference data and all scenarios are plotted together; visually, Scenario 4 looks very similar to the reference data.....	56

- Figure 3.9: Difference of seismic data (baseline –monitor) .The reference data and all scenarios are plotted together. Visually Scenario 4 looked very similar to the reference data.....57
- Figure 3.10: Difference of seismic amplitudes obtained from the Reference Model with noise levels corresponding to RRR=0.19 [panels (a) and (b)], RRR=0.56 [panels (c) and (d)] and RRR=1.14 [panels (e) and (f)]. The time vintages are labeled in the panels.....64
- Figure 3.11: RRR attribute maps of TL seismic data obtained from the reference model. Each panel shows the attribute map for two time vintages and different noise levels, characterized by RRR (labeled on each panel).....65
- Figure 3.12: Plot of similarity attribute, for no noise case, as a function of scenarios. The two curves show similarity measure (in volume and map, respectively) of the data from the reference model and the scenarios for time vintage April 2009 through July 2010. The attribute maps and amplitude difference volumes that are used to compute the similarity attribute are shown for each scenario and the reference data.....67
- Figure 3.13: Plot of similarity attribute, for no noise case, as a function of scenarios. The two curves show similarity measure (in volume and map, respectively) of the data from the reference model and the scenarios for

time vintage April 2009 through July 2010, with noise equivalent of  $RRR=0.19$ . The attribute maps and amplitude difference volumes that are used to compute the similarity attribute are shown for each scenario and the reference data.....68

Figure 3.14: Plot of similarity attribute, for no noise case, as a function of scenarios. The two curves show similarity measure (in volume and map, respectively) of the data from the reference model and the scenarios for time vintage April 2009 through July 2010, with noise equivalent of  $RRR=0.56$ . The attribute maps and amplitude difference volumes that are used to compute the similarity attribute are shown for each scenario and the reference data.....69

Figure 3.15: Plot of similarity attribute, for no noise case, as a function of scenarios. The two curves show similarity measure (in volume and map, respectively) of the data from the reference model and the scenarios for time vintage April 2009 through July 2010, with noise equivalent of  $RRR=1.14$ . The attribute maps and amplitude difference volumes that are used to compute the similarity attribute are shown for each scenario and the reference data.....70

Figure 3.16: Difference of RRR attributes for all the scenarios and the reference data with no noise [time vintage April 2009-July 2010]. The numbers reflect the normalized RMS of the difference .....69

Figure 3.17	Difference of RRR attributes for all the scenarios and the reference data with no noise [time vintage April 2009-July 2011]. The numbers reflect the normalized RMS of the difference .....	70
Figure 3.18:	Difference of RRR attributes for all the scenarios and the reference data with no noise [time vintage April 2009-July 2010]. The numbers reflect the normalized RMS of the difference with noise 0.56.....	71
Figure 3.19:	Difference of RRR attributes for all the scenarios and the reference data with no noise [time vintage April 2009-July 2010]. The numbers reflect the normalized RMS of the difference .....	71
Figure 4.1:	Smoothed P-wave velocity profile for WFD model.....	75
Figure 4.2:	Comparison of synthetic and field VSP (left panels). At right, the P-wave velocity profiles are plotted for zero, mid, and far offset shots. Top inset shows the shot location with respect to the active wells.....	76
Figure 4.3:	Frequency spectrum comparison of the field and synthetic VSP.....	77
Figure 4.4:	Source wavelet extracted from surface seismic data shot in 2006.....	78
Figure 4.5:	Velocity models for both baseline and monitor. Zoomed version shows the changed velocity due to steam .....	78
Figure 4.6:	Density models for both baseline and monitor. Zoomed version shows the changed density due to steam .....	79

Figure 4.7:	Schematic diagram showing VSP geometry .....	79
Figure 4.8:	Shot gathers from baseline, monitor and the difference (AGC). The first break is plotted in green for visual purposes .....	80
Figure 4.9:	First, several breaks are picked manually and inverted for velocities; best matched are used in averaging .....	82
Figure 4.10:	Shows velocity inverted from picks. The first three show good correlation, but the last two graphs shows considerable jitter .....	83
Figure 4.11:	Left panel shows model velocities, exactly repeatable on the top and only differing at the reservoir level. Middle panel shows median VSP velocity; the finer details of the velocity change are missing in VSP velocity compared to model velocities. Right panel shows the average velocities; in this case, the correlation coefficient is higher than in median.....	84
Figure 4.12:	Plotting the difference, we note the match is much better than the manual pick. There is no anomaly on the top and the steam feature coincides. The steam front appears at 1048 m, whereas in the model it appears at 1056 m.....	85
Figure 4.13:	Deconvolution spectrum.....	85
Figure 4.14:	Upgoing before and after deconvolution.....	86
Figure 4.15:	The normalized difference in the corridor stack can be generated by dividing the true difference by the RMS of the monitor panel. The true	

	difference is the subtraction of baseline from the time-shifted monitor.....	87
Figure 4.16:	Three panels (zero, near, and far) for wavefield separated. The upgoing will be used as input in the migration.....	89
Figure 4.17:	The right panel is the Kirchhoff migrated section for baseline; middle is for monitor after corrected for time-shifts. The black line shows the area of data fidelity; outside this line, the data is not very dependable. Taking a difference and plotting a 12 dB gained the left panel, showing the steam feature. Going to steam is indicated by decreased impedance (lower density, lower velocity), so it shows up as a trough followed by a peak. There are events below the steam, which are multiples as the input is not deconvolved.....	91
Figure 4.18:	As the shallow receiver has no input in locating the steam, subsets of receivers were used in migration. Here, receivers shallower than 220 m were not used in migration. The images are better for both baseline and monitor; the difference image is also refined, though amplitude diminishes.....	92
Figure 4.19:	Deconvolved upgoing is used here as input in migration and we can see it improves the images. Events are continuous, flat, but as we know deconvolution introduce high frequency noise in the data , there are a lot	

of non-repeatable noise shows up in the difference image along with the  
steam.....92

Figure 4.20: Similar plots with suppress shear. The lateral extent of the baseline and  
monitor is heavily compromised as top 550 m data is not used .....94

Figure 4.21: Input is only the first 150 ms of upgoing data. This is a crude way to  
surgically remove multiples; the image looks narrow in the bottom. In the  
difference map, the number of multiples is lower.....94

Figure 4.22: Difference map shown for comparison. The left smaller window shows the  
input data.....96

Figure 4.23: Panels showing RRR map of the differences for non-deconvolved, sub-set  
non-deconvolved, deconvolved, and shear-suppressed muted sections,  
respectively. The RRR was calculated in a 60 ms window  
length.....97

Figure 4.24: Panels shows RRR map of the differences for nondeconvolved, sub-set  
nondeconvolved and deconvolved section respectively. The RRR is  
calculated in 40 ms window length.....97

Figure 4.25: Panels showing RRR map of the differences for non-deconvolved, sub-set  
non-deconvolved, and deconvolved section, respectively. The RRR was  
calculated in a 20 ms window length .....98

Figure 4.26:	Flow chart summarizing TL VSP processing and amplitude enhancement analysis.....	99
Figure 4.27:	Series of ray tracing for different receiver levels show the zone of illumination. As there is a skew in the reservoir models that reflects in the velocity models too. That non-symmetric feature creates asymmetrical ray density. Due to this reason multiples below steam appears shifted towards right.....	101
Figure 4.28:	Comparison of field VSP (processed commercially) and synthetic VSP. Results are very similar, although the synthetic VSP underwent minimal processing.....	102
Figure 5.1:	Horizontal components from baseline field VSP (April, 2009) shows no upgoing PS reflections.....	105
Figure 5.2:	Schematic diagrams: a) how P- and S-waves travel from source and generate different events as it hits a reflector and get recorded in a 3C down hole geophone.; b) annotated schematic diagram with different seismic events in VSP.....	105
Figure 5.3:	Annotated VSP events for baseline, monitor, and their 4D difference.....	106

Figure 5.4:	Difference of PP amplitude (monitor-baseline) for walkaway synthetic VSP. The amplitude difference between the two datasets is maximum at zero-offset and it decreases at larger offsets.....	106
Figure 5.5:	Theoretical simulation using CREWES Explorer applet showing how PP and PS reflectivity changes with different combinations of changed $\alpha$ , $\beta$ , and $\rho$ .....	110
Figure 5.6:	Two-layer velocity and density models used in WFD. The top layer remained unchanged, while in the bottom layers, velocity and density were modified to simulate different mode monitor situations. ....	112
Figure 5.7:	VSP modeling optimization to generate clear reflections .....	113
Figure 5.8:	Horizontal and vertical components of two-layer baseline VSP.....	114
Figure 5.9:	Horizontal and vertical components of model 8 VSP. ....	114
Figure 5.10:	Horizontal components of baseline and M8 and the difference .....	115
Figure 5.11:	Diagram showing relationship between angles for PS reflection for a fix receiver.....	115
Figure 5.12:	FK plots showing how upgoing events (both PP and PS) are separated from the total wavefield .....	117
Figure 5.13:	Dip median filtering and gating along PS event.. ....	117

Figure 5.14:	Extracted PS unflattened; amplitudes are extracted along the yellow event in the receiver gather panel.....	118
Figure 5.15:	Schematic stepwise illustration of data preparation to extract PS amplitude in a receiver gathers. ....	118
Figure 5.16:	plot of PS amplitudes as a function of offset for 4 models. The PS amplitude behavior is very similar to the theoretical curves shown in Figure 5.5.....	119
Figure 5.17:	Schematic diagram shows variable steam thickness.....	121
Figure 5.18:	X component VSP with various steam thicknesses. In the case of steam of 150 m, the top and base reflections are clearly separated; in the case of 100 m, it is still separated, but for 50 m steam, top and base reflections coincide.....	121
Figure 5.19:	Schematic diagram showing variable steam width.. ....	123
Figure 5.20:	Amplitude for PP and PS for baseline and monitor plotted as a function of shot offset for receiver depth 600 m. Insets show a schematic diagram of the baseline and monitor models and shooting geometry.. ....	124
Figure 5.21:	Amplitude for PP and PS for baseline and monitor plotted as a function of shot offset for receiver depth 700 m. Insets show a schematic diagram of the baseline and monitor models and shooting geometry. .....	125

Figure 5.22: Amplitude for PP and PS for baseline and monitor plotted as a function of shot offset for receiver depth 800 m. Insets show a schematic diagram of the baseline and monitor models and shooting geometry. ....126

Figure 5.23: Amplitude for PP and PS for baseline and monitor plotted as a function of shot offset for receiver depth 900m. Insets show a schematic diagram of the baseline and monitor models and shooting geometry. Here extracted amplitudes are contaminated as the receiver is too close to the reflector.....127

Figure 6.1: Integrated flowchart explaining reservoir model updating for TL.....135

Appendix A: Geometry and symbols used for calculating inline radii for the nonzero-offset Fresnel zone. (Eton et al.,1991).....143

# Chapter One: Introduction

## 1.1 Motivation and objective

With maturing basins and ever deeper and more complex frontiers, the importance of extending the life of and maximizing recovery from producing fields is critical. Lately, 4D seismic, or time-lapse seismic methods, has become a useful technology for monitoring fluid movement. The use of 4D seismic monitoring is becoming more common. Repeatedly acquired seismic is referred to as time-lapse seismic. It is a fairly new technology (Lumley *et al.*, 1997) allowing dynamic characterization of a reservoir in a true volumetric sense. The basic idea is that a production-induced change in the reservoir causes a change in the seismic signal over time. Time-lapse seismic can contribute significantly to improved well placement and production strategies (Koster *et al.*, 2000). Quantitative analysis of time-lapse data can directly lead to a refined reservoir model and act as an active aid to hydrocarbon extraction management.

Although the concept of time-lapse seismic reservoir monitoring is relatively new, a few notable pilot projects have been attempted at enhanced oil recovery (EOR) steam sites. Pullin *et al.* (1987) collected two 3-D seismic surveys before and after a steam pilot at an Athabasca tar sands reservoir site and compared time delay and amplitude

attenuation maps between the two stacked surveys. They were able to qualitatively map the location of heated versus unheated zones. Their observed vertical travel time delays and attenuations through heated sections of the reservoir were similar to predicted rock physics models. Eastwood *et al.* (1994) performed a similar analysis on a 3-D seismic monitor of an Alberta cyclic steam stimulation (CSS) project. They used two 3-D seismic surveys recorded at separate production and injection cycles. The steam flood process is one of the common methods of EOR and discussed in detail in the following section. Steam flow directions, rates, and efficiency can be unpredictable as the reservoir is often more complex and heterogeneous than it seems. This uncertainty can lead to expensive changes in injection well placement, intervals of perforation, surface steam facility planning, loss of expensive steam, and well complications. As a sufficient amount of steam enters the reservoir, it may change the pressure, temperature, and fluid saturation and can cause dramatic changes in rock physics properties. Those changes are reflected in seismic data and can be seen in seismic wave-field attributes. In principle, detecting and measuring changes in the seismic response as a function of time can lead to a better understanding of the steam-flood fluid-flow dynamics, and, in turn, can help optimize the production strategy for an EOR project (Nur *et al.*, 1984).

The oil field for this study is located in southern Oman and has been producing oil since 1984. The decision was taken to further develop it using EOR by means of steam flooding in 2009. The aim was an increase of the overall ultimate recovery factor to over 40 percent (Rocco *et al.*, 2010). The first steam-injection pattern work started in 2009. The challenge was to monitor the rate of growth and shape of the steam chest with limited permeability distribution information. Monitoring the steam growth and sweep efficiency as the steam is injected in the reservoir can be achieved by deploying a wide range of proven geophysical technologies. The objective for this pilot project is to select the most appropriate set of tools for the later full field deployment.

To achieve this objective, it is crucial to understand the reservoir's performance and identify uncertainties and complexities (such as permeability distribution) associated with the reservoir model. In turn, this requires integration of the dynamic reservoir model with the rock and fluid properties. Formulating a workflow to relate the acoustic properties to reservoir properties, thereby closing the loop in a time-lapse sense, is needed. Closing the loop can be defined as completion of one cycle of updating. The oil field in Oman "A" has undergone 15 months of steam injection. There was a set of full wave 3DVSP recorded prior to the steam injection (April 2009); another 3DVSP was shot in July 2010. Southern Oman is known for complex near-surface features, which

cause poor quality surface seismic data. In such areas, VSP imaging in 4D mode is a novel type of activity and often useful (Kiyashchenko & Mamari 2010; Kiyashchenko *et al.*, 2011). An extensive synthetic VSP processing and interpretation process is required for the development of time-lapse processing workflows, including reliable data selection, noise removal, and data matching steps. We understand that time-lapse seismic data clearly delineate steam front distribution (*e.g.*, Eastwood *et al.*, 1994; Issac, 1996; Sun, 1999; Nakayama *et al.*, 2008; Kato 2010). However, using only P-wave field procession gives a partial picture of the image. A challenging task will be to integrate the time-lapse and multicomponent seismic data into a quantitative interpretation.

## **1.2 Vertical Seismic Profile (VSP)**

A VSP is a seismic measurement process in which a signal is generated at the surface of the earth and gets recorded by motion sensors (geophones, hydrophones) secured at various depths in a well (Hardage, 1983, 2001; Toksöz and Stewart, 1984; Stewart, 2001). With the help of this particular recording geometry, the total energy-field (both downgoing and upgoing) can be recorded as a function of time and depth (Figure 1.1). Therefore, the VSP provides a very useful tool for determining some of the fundamental properties of propagating seismic waves. These insights, in turn, can

improve the structural, stratigraphic, and lithological interpretation of surface seismic recordings (Hardage, 1983, 2001; Stewart, 2001). The VSP plays important roles in assessing the rock and fluids close to the borehole (Stewart, 2001) and providing in situ rock properties at depth, particularly seismic velocity (Stewart, 1984), impedance, anisotropy, and attenuation. It assists in understanding seismic wave propagation (*e.g.*, source signatures, multiples, and conversion, along with its own stand-alone seismic reflection image. As a result, the use of VSP is not only common in standard seismic processing and interpretation, but it is also becoming very popular in time-lapse seismic surveys and monitoring (O'Brien *et al.*, 2004).

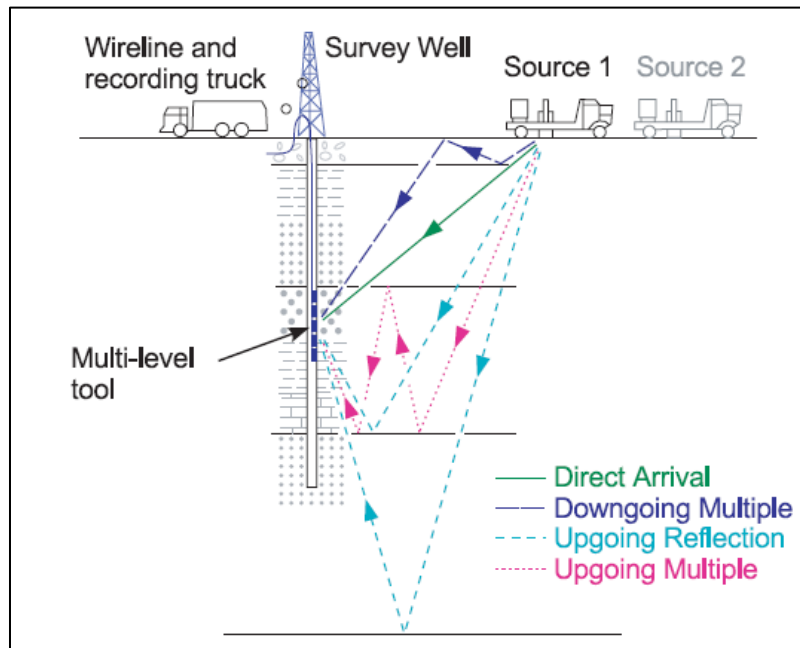


Figure 1.1: Schematic diagram of a VSP survey (DiSiena *et al.*, 1984).

### **1.3 Study area geology and field development**

The “A” field is located in the eastern flank of the South Oman Salt Basin (Figure 1.2) and belongs to the Oman National Oil Company (PDO). This field was discovered in the early seventies and was in production for twenty-six years before it went into cold production (Rocco *et al.*, 2010). PDO and Shell International E&P (SIEP) are working together to identify the most suitable technology to monitor the changes at a reservoir level.

The field comprises a four-way dip closure. The reservoir consists of a 200 m thick sandstone column of heavy oil (17-25 API). It is located on the eastern flank of the South Oman Salt Basin. The Haima Super Group consists of four Formations: Karim, Haradh, Amin, and Mahwis, of which only the first is not oil bearing (Rocco *et al.*, 2010). The Haradh Formation forms the bulk of the reservoir and reserves. Field “A” is penetrated by over a hundred wells; daily production averages 200-350 m<sup>3</sup>/day.

Figure 1.3 shows the main reservoir units. The sandstone reservoirs of the Haima Super Group were deposited under arid continental conditions. The oldest, the Haradh Formation, was deposited in a braided stream environment and contains baffles produced by shale layers and rip-up mudstone conglomerates. It is comprised of well to moderately sorted, fine- to medium-grained sandstone with alternating fining and coarsening-upward cycles. Overall, the Haradh is a coarsening-upward sequence with a thickness varying

from approximately 600 m in the south to approximately 900 m in the north of the field. The best-developed sandstones are medium-grained and are located at the top of the sequence. The Haradh is separated from the overlying Amin Formation by a regional unconformity that produces an irregular surface at the top of the Haradh. The top seal is generally a combination of Al Khlata and the Rahab shale, whereas in the north, the seal is formed by a combination of Al Khlata and the Cretaceous Nahr Umr Shale (Hughes Clarke, 1988).



Figure 1.2: Location map of the the “A” in southern Oman (www.map.com)

<b>Carboniferous to early Permian</b>	<b>Super groups</b>	<b>Formations</b>	
	<b>Gharif</b>	<b>Middle Gharif</b>	<b>Oil bearing</b>
		<b>Lower Gharif</b>	<b>Oil bearing</b>
	<b>Al Khata</b>	<b>Al Khata P1</b>	<b>Not oil bearing</b>
		<b>Al Khata P5</b>	<b>Oil bearing</b>
		<b>Al Khata P9</b>	<b>Present only in the flank- Not oil bearing</b>
	<b>Haima</b>	<b>Mahwis</b>	<b>Oil bearing</b>
		<b>Amin</b>	<b>Oil bearing</b>
		<b>Haradh</b>	<b>Oil bearing</b>

Figure 1.3: Stratigraphic column in field "A".

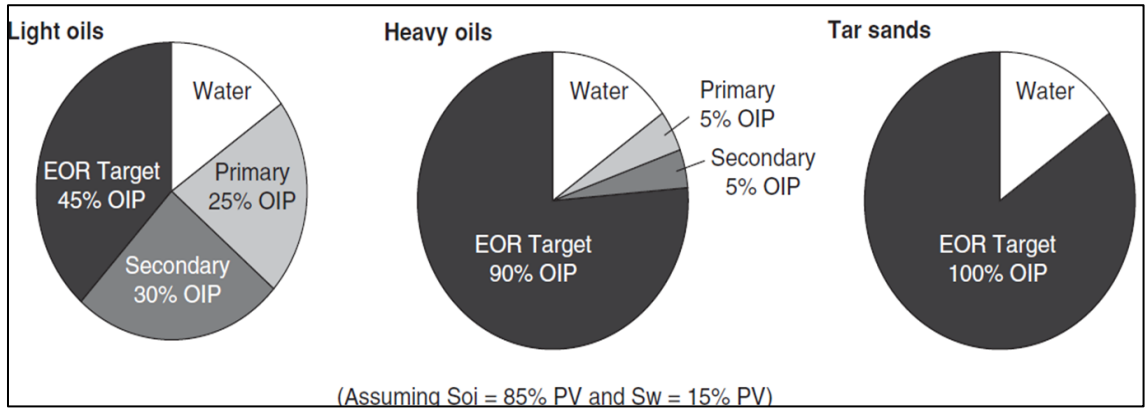


Figure 1.4: EOR target for different hydrocarbons (Thomas, 2008).

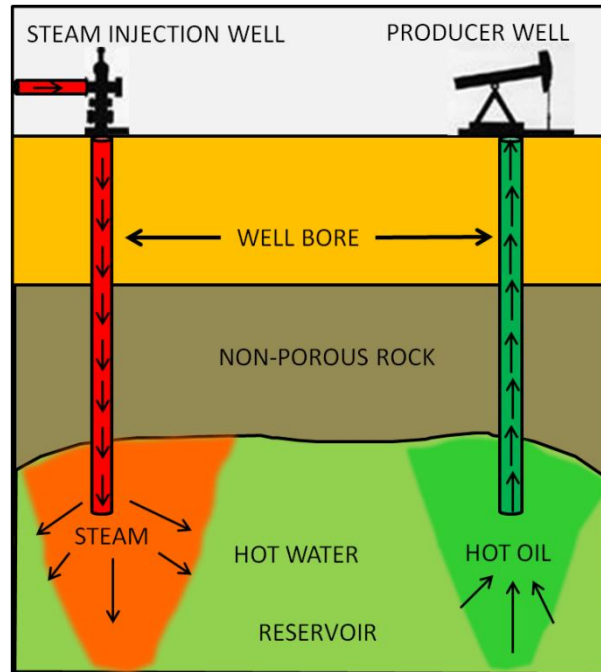


Figure 1.5: Conceptual section of the steam flood process.

To increase productivity, the field went into an EOR phase. EOR is a generic term for techniques used to increase the amount of crude oil extraction from an existing oil field. EOR, also called improved oil recovery or tertiary recovery, has become a popular method to increase crude productivity (Figure 1.4). EOR usually means recovery of oil beyond primary production and secondary water flooding (Thomas and Ali, 1993; Thomas 2008). If, however, the oil is too heavy to produce, EOR is used as a primary method. EOR can be further broadly categorized into thermal and non-thermal (Table 1.1) techniques; the scope of the current dissertation deals with the major thermal EOR process called steam injection (Figure 1.5).

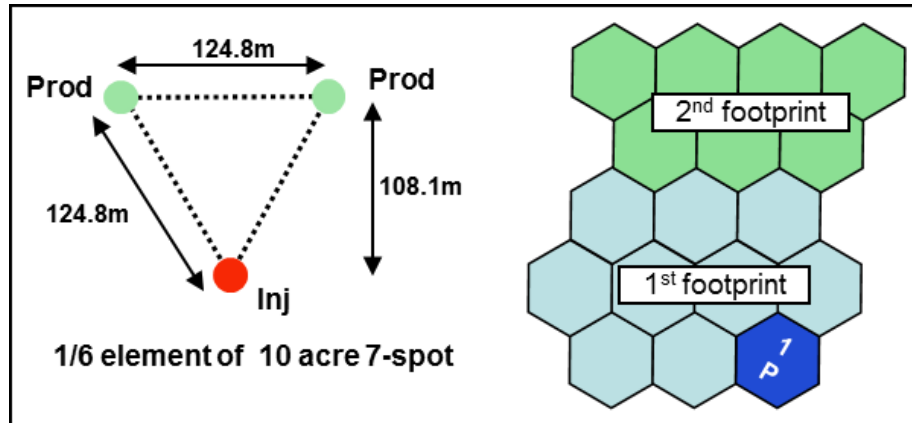
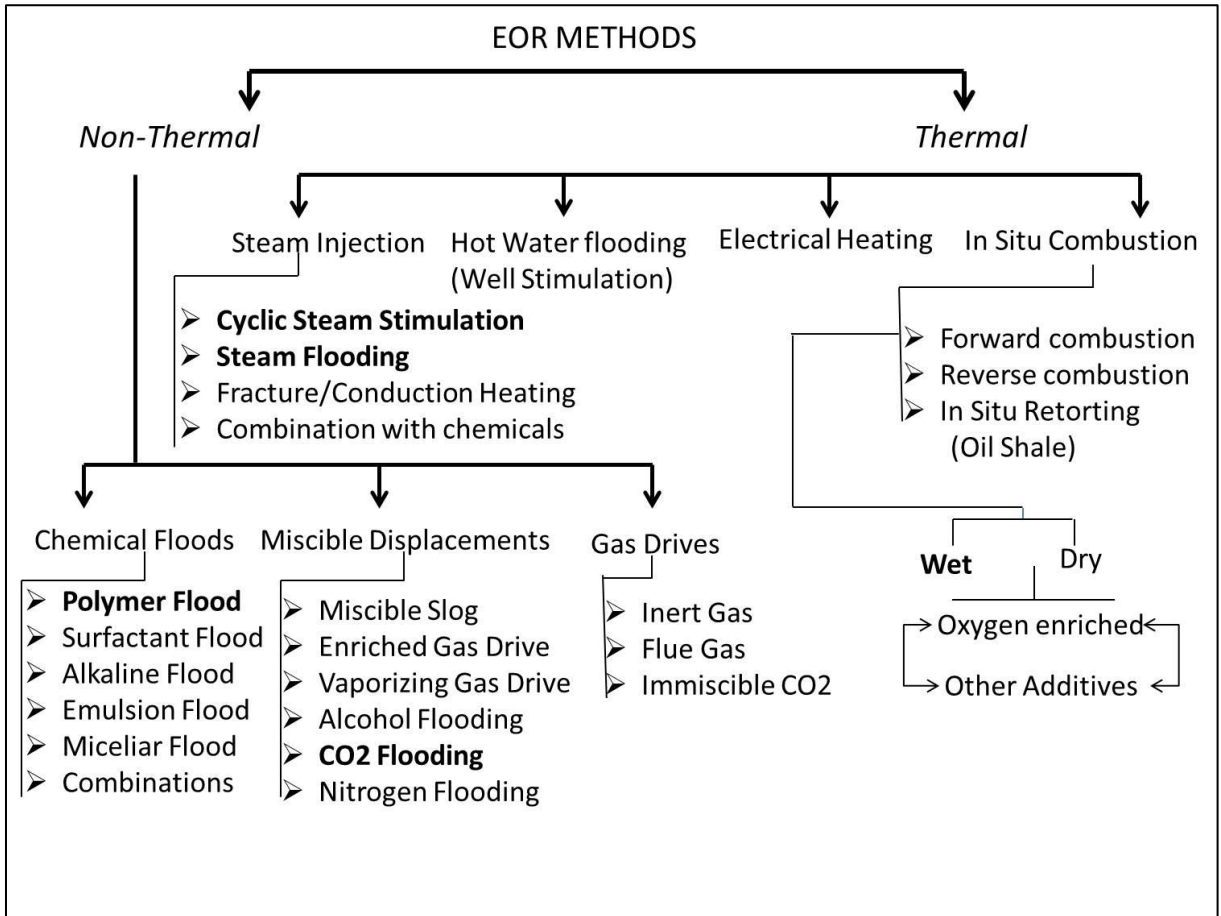


Figure 1.6: Pattern design in field "A". The hexagon at the bottom right represents the first pattern (1P).

At the beginning of 2009, steam injection started in the first pattern (1P) of an onshore thermal EOR. In the following 15 months, a daily average of  $195 \text{ m}^3$  of steam was injected in the central injector well surrounded by six oil producer wells in the shape of a 10-acre hexagonal pattern (Rocco *et al.*, 2010). The thermal development using steam flooding in field "A" makes use of 10 acre 7-spot patterns with one central steam injector well and six surrounding producing wells (Figure 1.6). Figure 1.6 shows the size and location of the first pattern area centered at the injector well. This area has been under steam injection since early 2009. In the following 15 months a daily average of  $195 \text{ m}^3$  of steam was injected in the central injector well surrounded by six oil producer wells in the shape of a 10-acre hexagonal pattern (Rocco, 2010). Two down-hole seismic technologies (Cross-well seismic and 3DVSP) were deployed before (base) and after (monitor) the injection period to record changes caused by the steam as it flowed and heated the reservoir rock.

Table 1.1: Classification of EOR methods. Highlights show commercially successful methods (Thomas and Ali, 1993).



## 1.4 Background study and previous work

### 1.4.1 Steam injection

In 2009 steam injection started in the first pattern (1P). In the following 15 months, a daily average of  $195 \text{ m}^3$  of steam was injected in the central injector well surrounded by six oil producer wells in the shape of a 10-acre hexagonal pattern (Rocco *et al.*, 2010). The attempt was to mobilize the heavy oil (17-25 API, 80 cp – 500 cp) contained in this sandstone reservoir 1,000 m below the surface. Two down-hole seismic technologies (Cross-well seismic and 3DVSP) were deployed before (base) and after (monitor) the injection period to record changes caused by the steam as it flowed and heated the reservoir rock. It is an established fact that in our study area, surface seismic is not very helpful due to complex near-surface effects. As a result, use of the borehole seismic technique was crucial in the present effort. Due to the high-resolution characteristics of the cross-well seismic method, it is quite likely possible to infer new intra-reservoir details that had not previously been observed with standard surface seismic data. Figure 1.7 shows the steam injection profile in which the 4D period has been shaded; the baseline and monitor surveys are marked in blue and red, respectively. Before the main injection started in May 2009,  $9,500 \text{ m}^3$  of steam had been already injected in the pattern. Both base surveys (cross-well seismic and 3DVSP) were acquired after this initially injected volume. Injection was interrupted several times during the fifteen month injection period; net injection time was eleven months. The total injected volume during the time-lapse period was  $90,473 \text{ m}^3$ . The maximum injection rate, when

all steam generators were operational, was over 360 m<sup>3</sup>/day (Rocco *et al.*, 2010). Temperature monitoring within this pattern was carried out with periodic fluid measurements at the wellhead of producer wells; temperature was also logged in three dedicated observation wells inside the pattern. These observations indicated no changes in temperature until March 2010, ten months after the base survey. By the time of the monitor survey in July 2010, only three wells (not including the injector) had detected changes in temperature (Figure 1.8). One of these wells is the observation well T8, located 30 m southeast from the injector. This well registered the highest temperature in the pattern. The steam injection was delivered through two sets of perforations in the upper section of the reservoir. PLT surveys taken in the injector showed highest readings at the top perforation. Well T8 was drilled in December 2008; no temperature response was recorded in this well until March 2010. Well P4, located to the north of the injector, also saw the temperature of the produced fluids and the oil rate increase in March 2009. Maximum recorded temperatures at the time of the monitor survey are shown in Figure 1.8. Data acquisition of base and monitor surveys was carried out while minimizing the sources of noise around the producing pattern. Beam pumps at the producer wells and steam injection were not operational during the campaign. The cross-well seismic survey made use of the producing wells located at the corners of the hexagonal pattern. Due to the presence of H<sub>2</sub>S, operations required specific well control equipment while recording the in-well data. The 3DVSP surveys, acquired immediately after the cross-well seismic, made use of an existing observation well (T5) inside the pattern where the geophones were deployed. Shot point locations were accurately positioned during the monitor survey over an area centered on this well. It was also very important to obtain the highest

repeatability possible in order to increase the chances of measuring a time-lapse signal (Rocco *et al.*, 2010).

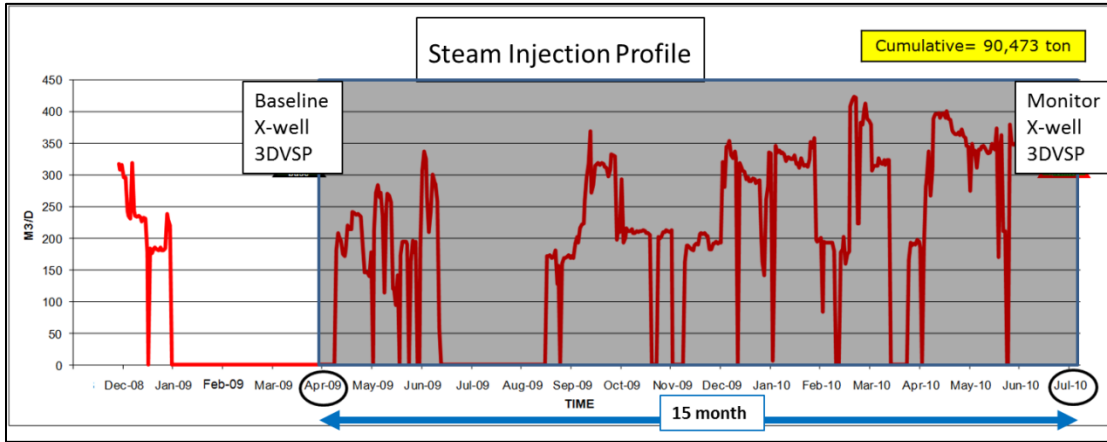


Figure 1.7: Steam injection profile in the first pattern. The fifteen month time-lapse monitoring period is shaded.

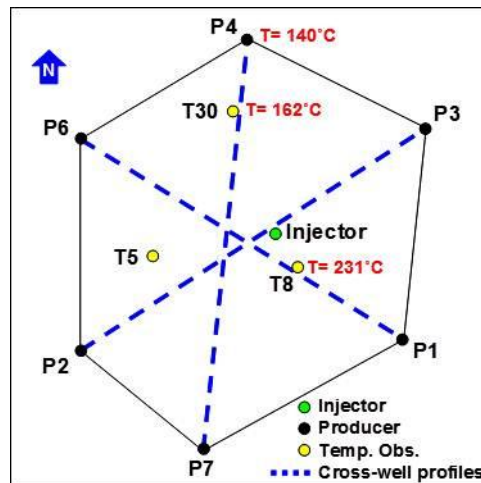


Figure 1.8: Graph showing the first pattern shape and well locations. In red are the maximum temperatures recorded at the time of the monitor survey in July 2010. Dotted blue lines show the location of the cross-well seismic profiles.

The target in this study is a weak reflector and the expected steam-induced velocity and density changes are rather small (less than 200m/s and 0.1g/cm<sup>3</sup>). Under

these conditions, downhole acquisition is more advantageous than surface seismic for two reasons: the Fresnel zone is reduced (worst-case lateral resolution estimate); and, as the receivers are close to target, it increases the signal to noise ratio and increases the detectability (Eaton and Stewart, 1991; Appendix A: Fresnel zone calculation). Cross-well surveys also provide a large gain in vertical resolution in comparison with surface seismic and 3DVSP (Kiyashchenko and Maamari, 2010). The geology of this field is mostly flat, but the overburden generates a lot of multiples. Surface seismic multiples are more problematic since they are generated by both incident and reflected waves. In a VSP, however, there are more ways to handle multiples due to up and down wave separation. Both cross-well and 3DVSP delivered images of the EOR target that were superior to surface seismic. Normally in 3DVSP data, the common way of handling multiples is the spatial-domain deconvolution of up-going waves using filters derived from the down-going waves, which is correct for zero-offset VSP and flat-layered medium. The same approach is also used in other cases where the multiples are assumed to appear within a short enough interval after the first arrival.

#### **1.4.2 Time-lapse 3DVSP**

In Field “A”, the baseline was acquired in 2009 over the first pattern area using 3500 shot locations on a 25 m by 25 m grid, covering a (1.6x1.6) Km<sup>2</sup> area with a long 100-level geophone array in the deviated VSP observation well, located northwest from the injector. The 100 receivers covered depths from 400 m to 1200 m, with the spacing at about 8 m. The vertical component data were initially processed with a standard workflow, including component rotation, anisotropic velocity modeling, up/down

deconvolution, and Kirchhoff migration. The VSP image was better than surface seismic: important horizons were identifiable with limitations; however, the edges of the image had multiple events, which were not expected. Subsequent tests demonstrated that up/down deconvolution boosts the amplitudes of the larger-offset data, while delivering reasonable results for small offsets. Raw data analysis revealed prominent down-going and up-going multiples contaminating the image. Space-time up/down deconvolution is applicable for multiple elimination for zero-offset source and vertical wave propagation. For an offset source, it is problematic if the periods of the same order up-going and down-going multiples are different. For handling the multiples problem, Field “A” “interferometric deconvolution” was developed (Kiyashchenko and Maamari, 2010). Figure 1.9 shows the comparison between normal 3DVSP and interferometric deconvolved 3DVSP.

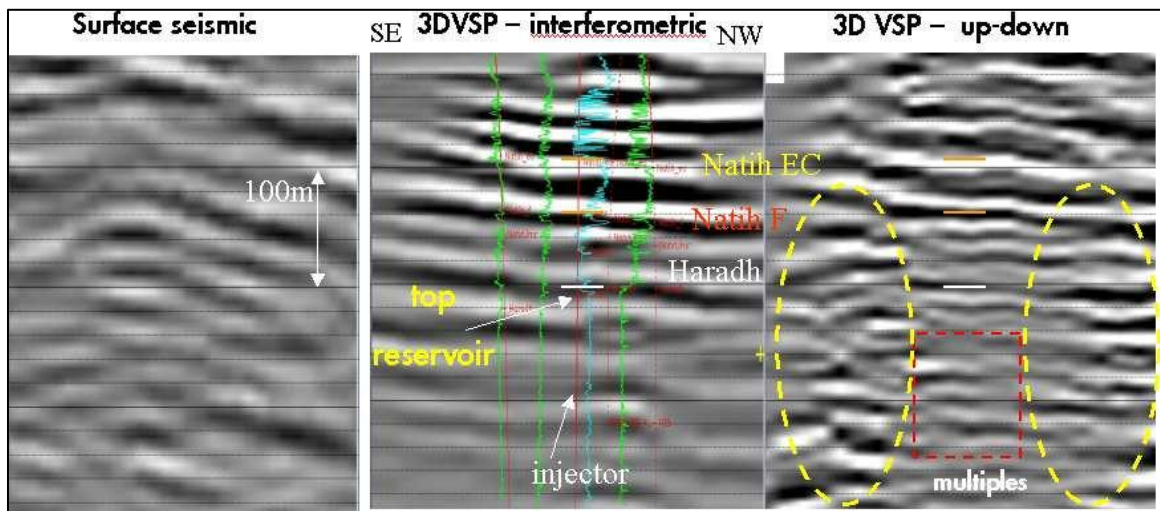


Figure 1.9: The surface seismic image (left), the 3DVSP images obtained after interferometric deconvolution (middle) and space-domain up-down deconvolution (right). All are plotted along southeast-northwest cross-well profile. Green (resp. blue) lines are density (resp. P-wave velocity) logs (Kiyashchenko and Maamari, 2010).

During the 3DVSP acquisition, a downhole repeatability test was done by shooting repeat walkaway VSPs. This test included a baseline and monitor survey when the VSP tool was taken out and redeployed in the borehole. The baseline and monitor surveys were processed in different ways; their similarity was evaluated by computing RMS repeatability ratios (RRR). The more advanced processing with amplitude balancing and advanced deconvolution increases repeatability, allowing a value as small as 0.1 to be achieved with a walkaway VSP. This indicates the possibility of having fairly good repeatability with a monitor survey in 2010. Figure 1.10 shows the results for a cross-section along an east-west traverse going across the 4D anomaly. The time-lapse difference shows the most prominent event at the top Haradh reservoir level, with weaker events at the shallower Natih EC level (noise) and at a deeper level (multiples). As a measure of repeatability, we used the RRR attribute (RMS of the difference normalized by average RMS of the baseline and monitor data, calculated in the running window of 60m; equivalent of NRMS attribute suggested by Kragh and Christie (2002)). The resulting images have very good repeatability within the pattern (Figure 1.11). RRR is about 0.1 at the level of Natih EC – the strongest event in the section where no changes are expected. A polygon outlining the repeatable image area is shown on the map. Repeatability of events that are not subject to change is a good diagnostic to assess different processing workflows and time-lapse response of 3DVSP images.

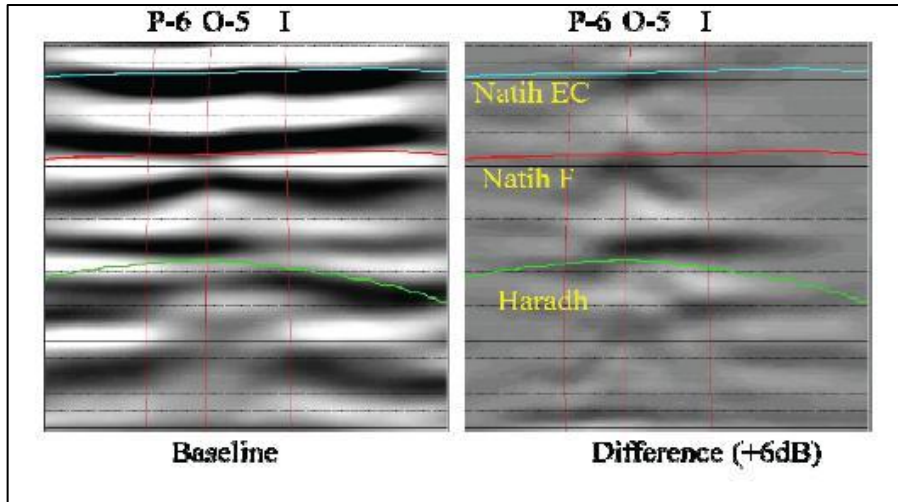


Figure 1.10: 3DVSP baseline (left) and difference (right) images (with well projections) for east-west traverse crossing the pattern.

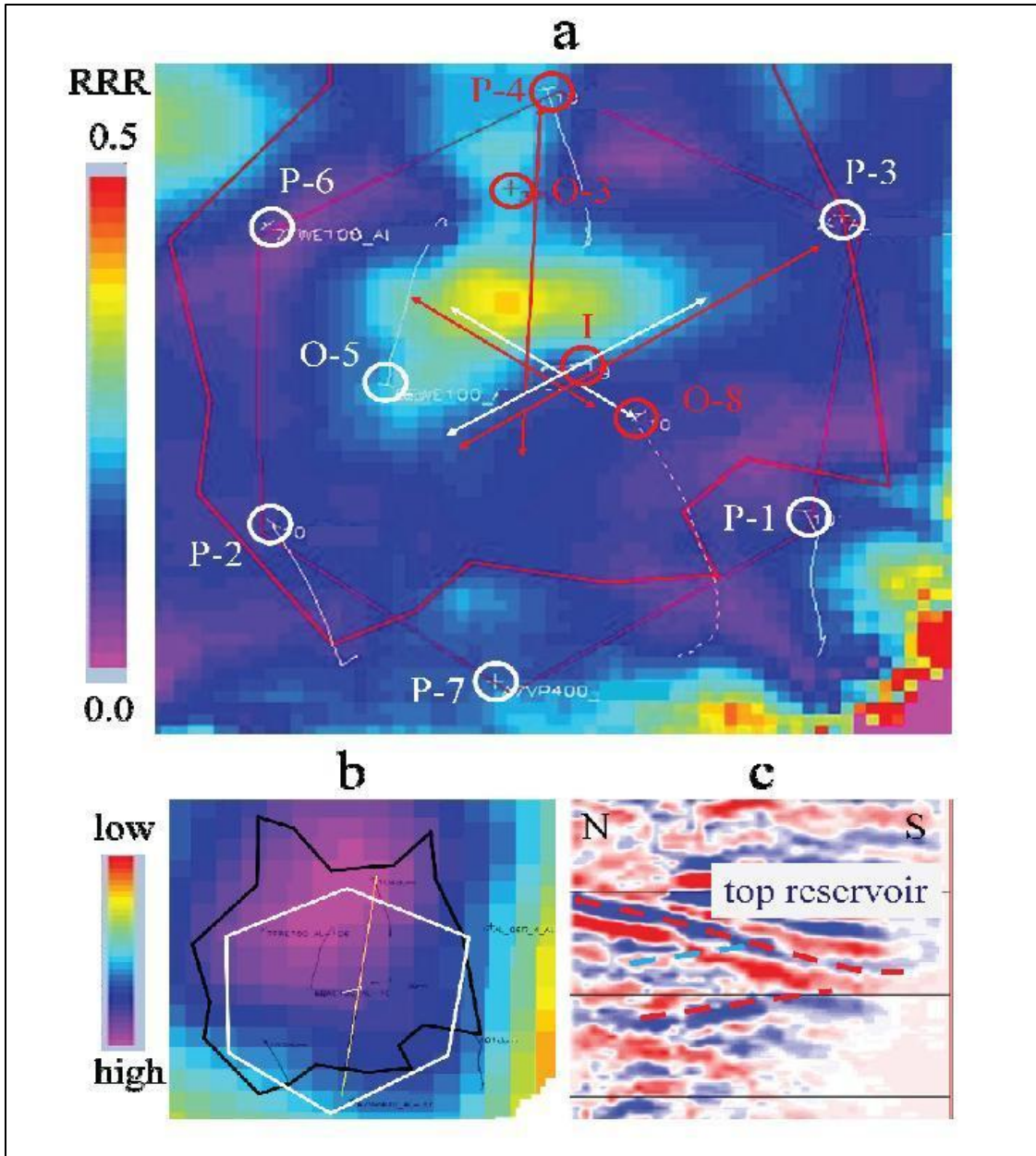


Figure 1.11: a) RRR map at the top Haradh reservoir level. White circles are cold wells and red ones are hot. Red arrows indicate the anomaly extent interpreted from cross-well tomography and white ones from cross-well reflection images; b) the top Haradh relief; and, c) a wedge-type geometry visible with the cross-well seismic image for north-south profile (Kiyashchenko *et al.*, 2011).

## 1.5 Scope of modeling

The uncertainty of monitoring the steam chest with time is high. Oversimplified reservoir models can give an incorrect estimation of steam developments, leading to steam loss, incorrect pressure predictions, and loss of rig times. Seismic time-lapse techniques are well-proven in offshore fields around the world, but remain challenging onshore; areal surveillance examples of thermal developments are very rare in depths greater than 800 m. Southern Oman is well known for poor surface seismic imaging. Moreover, as the field has been producing for more than two decades, the site construction and rig noise are significant issues in repeat surveys and data quality because the data can be highly compromised due to a poor signal-to-noise ratio. In the present field, the time-lapse effect was reported as very weak: the P- wave velocity drop is about 200m/s and the density change is 0.1 gm/cc. Choosing the correct repeat time is very important; it is also crucial to have an estimate about the noise level tolerance in 4D signal processing.

A time-lapse feasibility study should be a complete loop from selection of a correct reservoir model to incorporation of all available petrophysical information and needed customized processing. Prior to acquiring actual field data, it is prudent to execute an extensive reservoir simulation, generate synthetic seismograms, and process them to forecast the dynamic behavior of the steam.

## **1.6 Modeling software**

The reservoir modeling and simulations are performed in Shell's proprietary in-house software (Xstrem), which can integrate reservoir properties, rock and fluid properties, and elastic properties on a single platform. Multicomponent VSPs are generated with full waveform finite difference modeling codes (courtesy of W. Moulder). VSP processing and attribute analysis are also performed using Shell's internal software (SIPMAP, 123DI). Petrophysical analysis is performed using Gassmann substitution and FLAG models (Liu, 2006). Theoretical reflectivity analysis and AVO curves are measured from CREWES explorer software.

## **1.7 Dissertation outline**

The first objective of this dissertation is to execute a detailed workflow to select a reservoir model to understand steam flow behavior and permeability distribution within the steam-flooded zone. To accomplish this, we scale up the geological model and then simulate fluid flow. We also convert outputs from the reservoir simulation, such as spatial variation of porosity, fluid saturation ( $S_g$ ,  $S_w$ , and  $S_o$ ), pressure, and temperature for different time steps, to acoustic properties using validated rock and fluid models. We then convolve the generated acoustic impedance volumes with a wavelet extracted from the surface seismic to generate synthetic seismic (primaries only) with different signal-to-noise (S/N) ratios. There can be many permeability distribution patterns within the reservoir, which can alter the steam flooding rates and shapes. We execute a simulated "Close-the-Loop" workflow based on scenario modeling that relates changes in acoustic

properties (velocity and density) with those in reservoir properties (such as oil saturation, temperature, and permeability), as discussed in Chapter 3.

The second objective of the dissertation is to process, analyze and interpret the synthetic time-lapse P-wave VSP dataset to observe time-lapse AVO response on PP-waves. We generate the synthetic data through a finite difference model simulating a vertical well with a vertical force. Because the modeling was done with no attenuation incorporated, a number of multiples result in the data. In Chapter 4, we discuss various processing steps used to control multiples with minimal harm to the 4D signal. We also present our further attribute analysis and compare modeled results to field data for data validation.

Because the target horizon is a weak reflector and petrophysical changes (velocity and density change) are very low in the study area, an almost zero PS reflection from the top of the steam results. Given this context, the third objective of this dissertation is to determine the minimum change in density and velocity needed to have a seismically-detectable PS response. In Chapter 5, we discuss a detailed modeling study that involves unfolding the PS behavior in the heated reservoir and the steam zone. We observe how PS changes as we approach from a heated zone (temperature effect) to the core of a steam-flooded area (density effect). In Chapter 6, we integrate our results and methods, offer suggestions, and outline the possible scope of future research.

## Chapter Two: Rock physics

### 2.1 Introduction

For quantitative seismic processing and interpretation of a steam-flooded heavy oil zone, we need to have a clear understanding of the petrophysical changes within the reservoir. Seismic values are affected in complex ways by many reservoir properties, such as pressure, temperature, fluid saturation, fluid type, porosity, and pore type (Wang, 2001). When steam is emplaced in a reservoir, it changes the acoustic and elastic properties of the reservoir. The effect of steam is more pronounced on the reservoir fluid than on the rock matrix. Therefore, with increasing temperature and pressure, we need to understand the change in the effective elastic properties of heavy oil, as well as the saturated rock. These elastic factors are often interrelated or coupled with each other. To understand the rock physical effect on time-lapse (TL) seismic interpretation, rock physical modeling is essential.

To perform rock physical modeling for a heavy oil reservoir, it is very important to accurately know the temperature and pressure dependences of elastic properties of heavy oil itself. Han *et al.* (2008) described the temperature dependence of P- and S-wave velocities of heavy oil by using liquid and glass points, which are defined as temperatures at a shear viscosity of 103 cP and 1015 cP (Figure 2.1). According to Han *et al.*, (2008) at temperatures lower than the glass point, heavy oil acts as a solid material due to its extremely high viscosity. At temperatures higher than the liquid point, viscosity is low enough so that its effect on the velocities can be neglected. Figure 2.2 shows the P- and S-wave ultrasonic velocities as a function of temperatures (Kato, 2010). It is also noted

that the measurements were conducted at atmospheric pressure and a frequency of 1.0 MHz.

Ultrasonic velocities are often different from *in situ* reservoir velocities. In the case of a steam injection field, temperature behavior is much more complicated than in laboratory studies. Because laboratory measurements are often undertaken at high frequencies, the elastic-stiffening effect gets exaggerated for both bulk and shear moduli. Lumley (1995) described the P-wave velocity front in an injection well, which is a function of temperature, pressure, and saturant (Figure 2.3). In Figure 2.4, P- and S-wave velocities and  $V_P/V_S$  changes are shown caused by steam injection in a heavy oil reservoir (Kato *et al.*, 2008). In that case, the  $V_S$  was slightly increased with increasing temperature and the  $V_P/V_S$  ratio was significantly reduced as the temperature increased.

We know from the geophysical literature that the  $V_P$  and  $V_S$  both decrease with increasing temperature and increase with increasing pressure (Chopra, 2010). As steam is injected in a reservoir, the density and the bulk modulus of the rock decreases, but the rigidity remains almost unchanged. This causes the P-wave velocity to drop, but the  $V_S$  shows an increase. The immediate density reduction has more effect on the  $V_S$ .

In this present pilot study in Oman, the monitor survey was conducted after one year of steam injection. During this year, the injection was stopped multiple times to accommodate VSP, cross-well seismic surveys, well log measurements, and other rig activities (Figure 1.7). These breaks in steam injection created an adverse effect in the steam chamber build up within the reservoir: steam quality decreases with time once injection stops. There is no first-hand information about the steam quality within the

reservoir. The ratio of steam versus water is defined by the steam quality. Steam quality is the proportion of saturated steam (vapor) in a saturated condensate-steam (vapor-liquid) mixture. A steam quality of 0 indicates 100 percent liquid, while a steam quality of 100 indicates 100 percent vapor.

One goal of this dissertation is to investigate the seismic detectability of the steam. In conventional PP imaging we measure the change in acoustic impedance change due to the injection of steam. The difference in the amplitudes of a monitor and baseline is a combined effect of steam, hot water, and heated oil. The total heated zone produces a different reflection coefficient than the non-heated zone. But when we analyze the PS reflections, they may show the amplitude variation in time, largely due to density changes. The density of the steam chamber is significantly different from the adjacent heated water and oil. Combining PP and PS amplitudes may successfully differentiate the steam-flooded zones from the heated surroundings.

We intend to develop a methodical approach to select and update time-lapse reservoir models and establish “cutoff” parameters, such as minimum velocity and density change, signal-to-noise ratio, steam thickness and width within the reservoir to expect a measurable TL response in PP and PS VSP processing. It is crucial to have an ample understanding of the rock physical changes within the reservoir.

In this chapter, we use the logs from the injector well to describe the rock type (reservoir and seal) and changes in velocities and densities (before and after the steam).

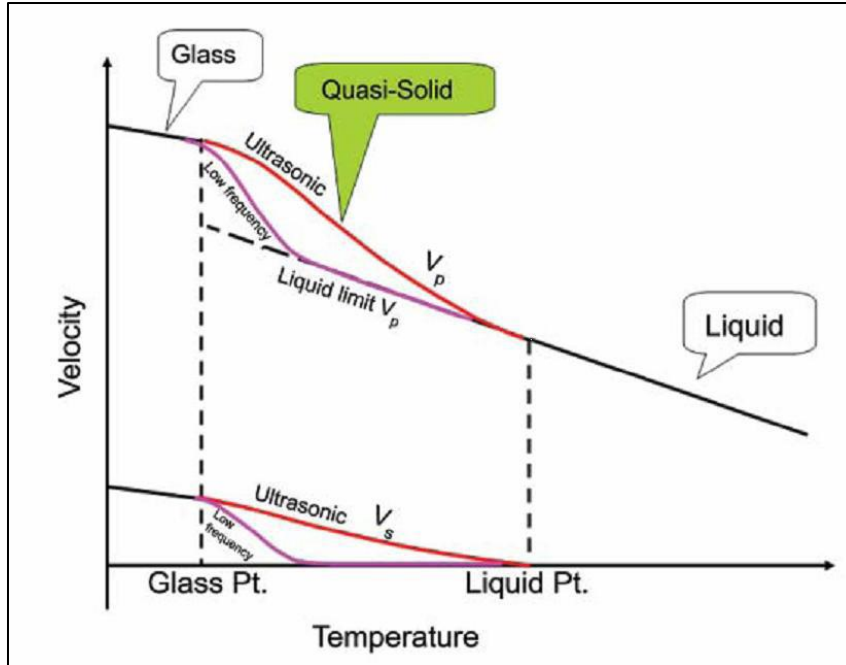


Figure 2.1: Concept of temperature dependence of P- and S-wave velocities of heavy oil at two different frequencies: ultrasonic and low. The temperature dependence can be approximately described by three main stages; liquid, quasi-solid, and solid states (after Han *et al.*, 2008).

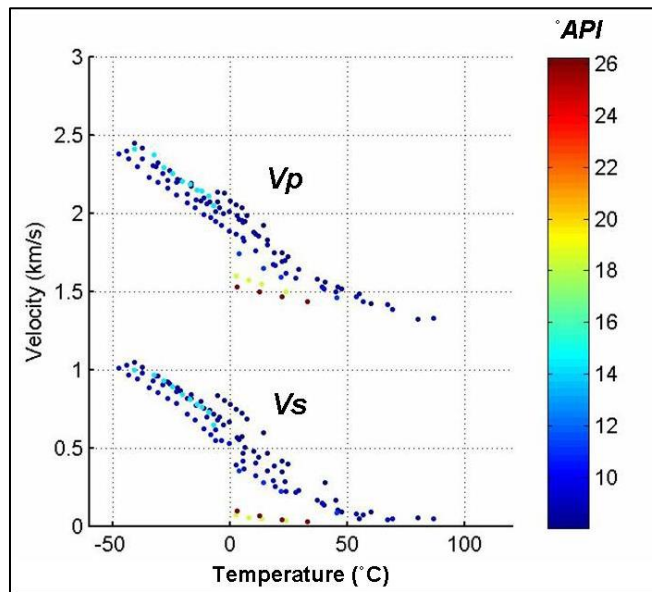


Figure 2.2: Ultrasonic P- and S-wave velocities of the heavy oils as a function of temperature. The color corresponds to the API gravity (after Kato, 2010).

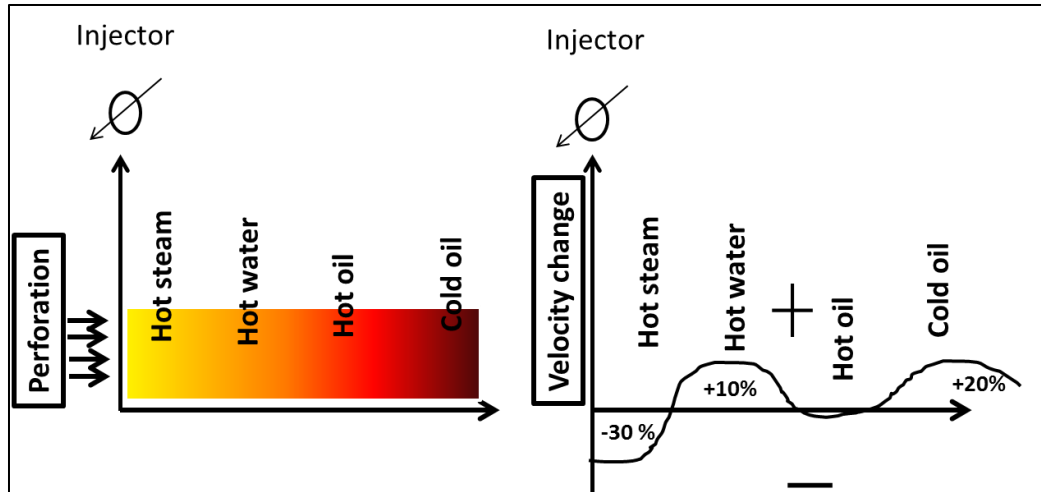


Figure 2.3: An idealized model of steam-flood fluid flow (left). A rapid high-pressure cold front is expected to lead the injector flow, trailed by hot oil, hot water and hot steam zones. The relative dimensions of each zone may not be to scale, and complexities such as mixed phases and gravity overrides are neglected. Right graph showed predicted steam-flood P-wave velocity changes compared to initial reservoir conditions as a function of dimensionless radial distance (after Lumley, 1995).

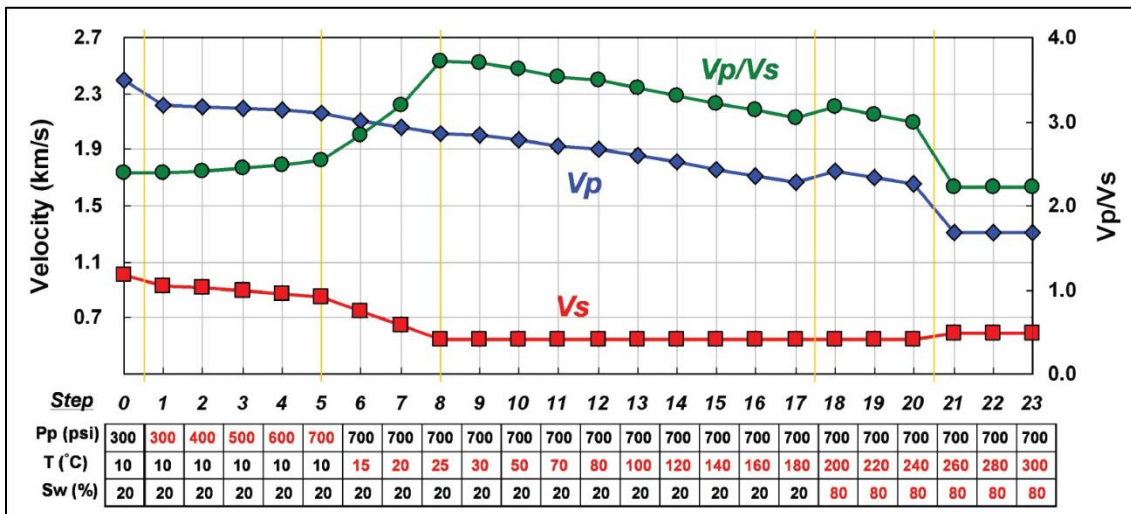


Figure 2.4: P- and S-wave velocities and  $V_p/V_s$  changes caused by the steam injection in heavy oil reservoir (After Kato *et al.*, 2008).

## 2.2 The reservoir

At the Haima level, Field “A” is a classic high relief “turtle-back” fault-bounded, anticline, measuring approximately 4 km by 2 km, oriented north-south (Figure 2.5). The crest of the reservoir is around 1160 m below ground level and the oil column height is close to 200 m. The field consists of four formations: Karim, Haradh, Amin, and Mahwis, the latter three of which are oil bearing. For this study, the properties of the Haradh Formation are most relevant because it is the EOR target.

In this formation, the porosity is around 23 percent, the permeability around 700 mD, and the net-to-gross ratio is around 97 percent. The reservoir seal is provided by a combination of Al Khlata diamictites (nonsorted to poorly sorted, terrigenous sediment) and Nahr Umr shales. The oil in Field “A” is relatively heavy and viscous (19° API). The modeled in-place density of the oil is roughly 950 kg/m<sup>3</sup>. The oil viscosity ranges from 200 to 600 mPa-s or cP. The gas-oil-ratio of the oil is very low, around 1, meaning the oil in the reservoir is assumed to be (nearly) dead oil. In dead oil, no dissolved gas components are released when the oil is brought to surface conditions. The bubble point pressure is also very low (407 kPa). Table 2.1 shows the petrophysical parameters of the reservoir.



### 2.3 Well logs and Temperature logs

Figure 2.6 shows a section of well logs (gamma, density, and velocities) from the injector well before the steam injection. We can see here that the natural gamma log shows the Haradh to be sandstone with occasional gamma peaks (shale streaks). As mentioned in Chapter 1, the producer wells are unevenly heated. Three among six producers are affected (heated) by steam injection whereas the other three are cold. The Shale baffles may have acted as a potential permeability barrier within the reservoir.

A  $V_P$  versus  $V_S$  crossplot is shown in Figure 2.7. The depth intervals are color-coded and the slopes of separation are very distinctly different under different lithology. The Haradh (marked as the red cluster) looked less steep than the top sand interval (900 m). The natural gamma ray log versus  $V_P/V_S$  is also plotted in Figure 2.8. The Haradh interval shows a consolidated cluster along the  $V_P/V_S$  value of 1.7-1.8, while the shale interval (1000-1030 m and 1030-1060 m are plotted in different colors) shows a wide range of  $V_P/V_S$  ratios. The 1000-1030 m zone shows higher  $V_P/V_S$  and the majority of data clusters around 2.3. The 1030-1060 m zone shows lower  $V_P/V_S$  and falls under 1.8-2.0.

Figure 2.9 shows a temperature log recorded over time for three observation wells. Wells 1 and 2 show an increase in temperature with steam injection, whereas well 3 is cold. Among the producers, only P6 (Figure 2.9 inset) produced hot fluid after steam injection; the rest of the producers were unaffected. This uneven heating of observation wells suggests that there is a high permeability connection towards the north of the hexagon, while the rest of the wells suffer from a permeability barrier.

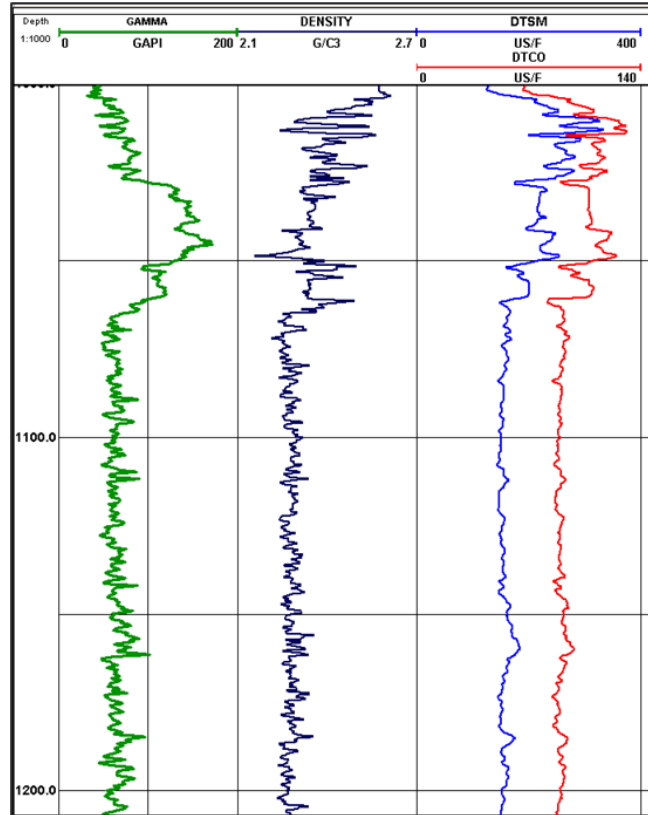


Figure 2.6: Well log from injector showing gamma, density and velocity (compressional and shear) velocities.

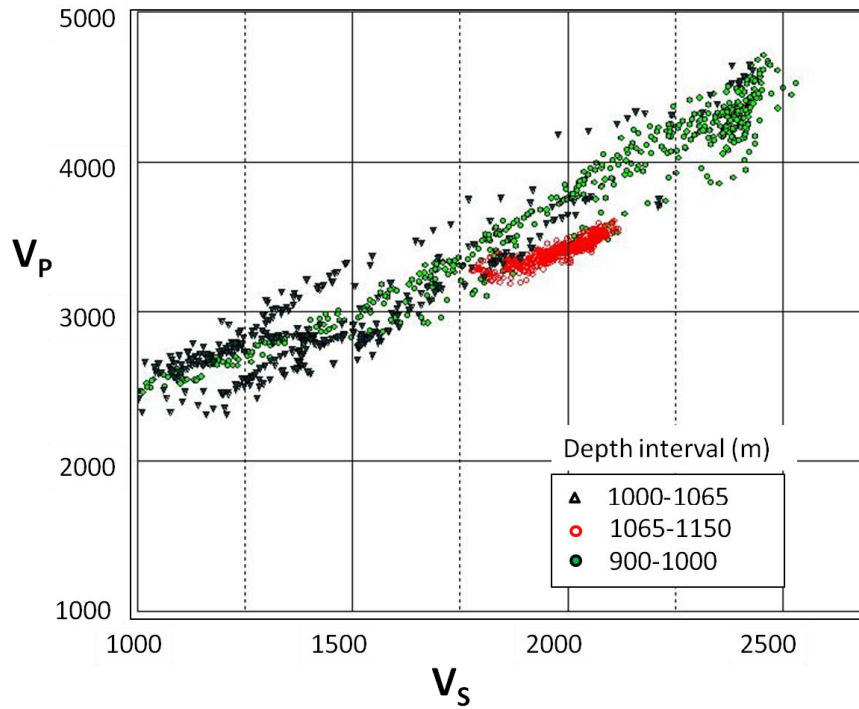


Figure 2.7:  $V_p$  versus  $V_s$  crossplot. Red cluster is the EOR target.

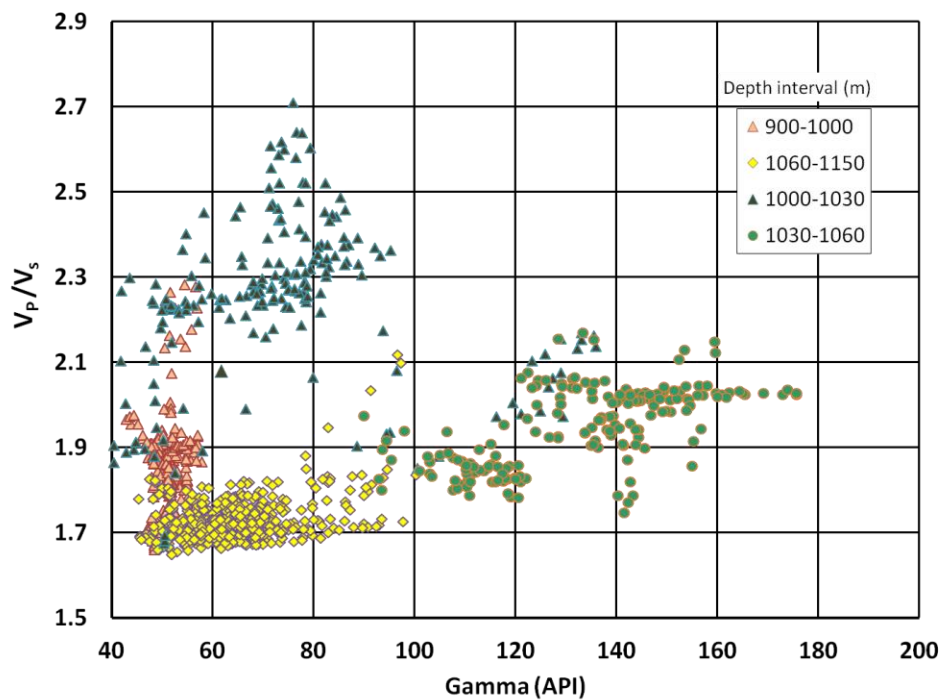


Figure 2.8:  $V_p/V_s$  versus Gamma crossplot. The yellow cluster is the EOR target. The shale intervals (1000-1030 m and 1030-1060 m) show a wide range of scatter.

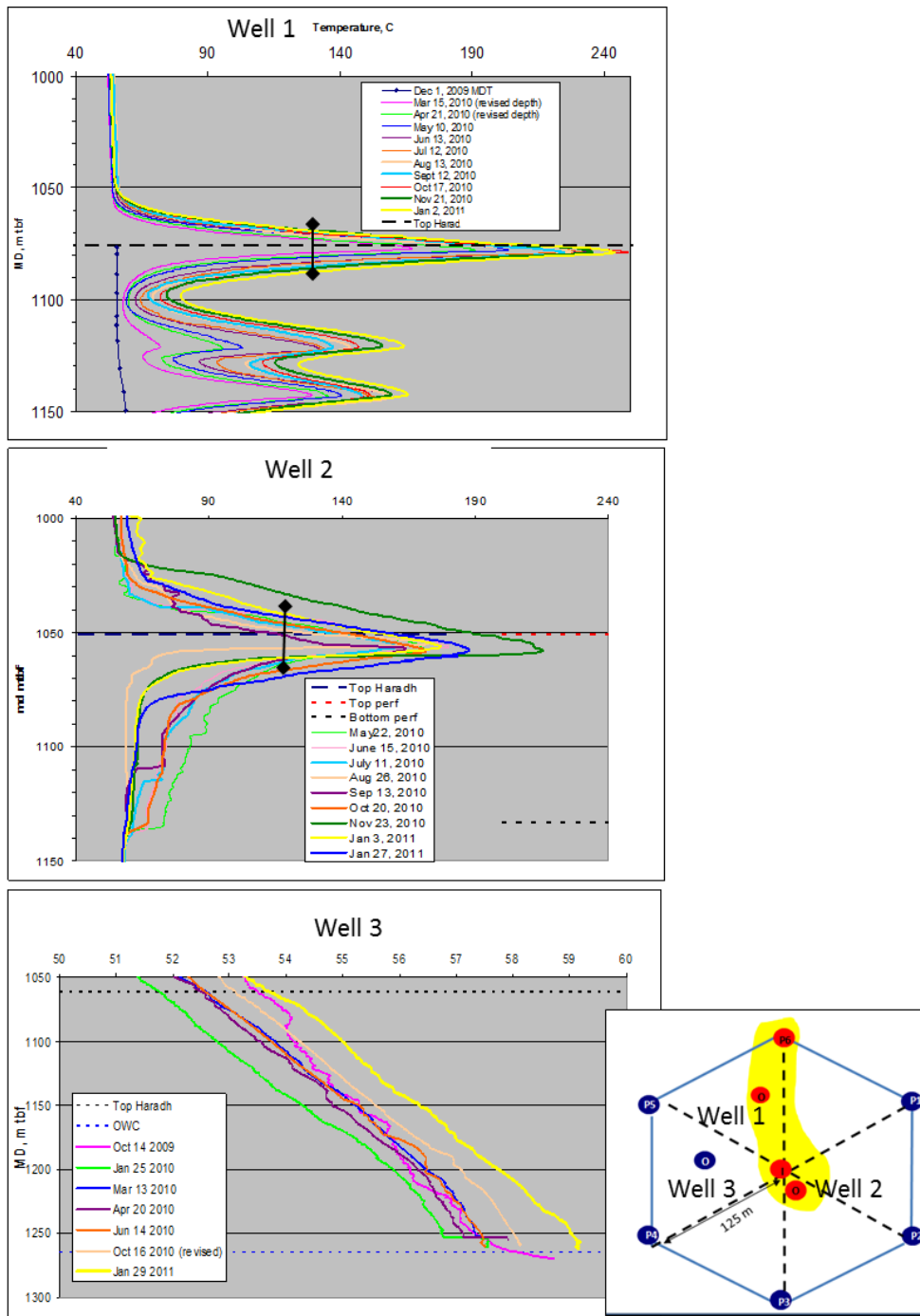


Figure 2.9: Temperature profiles from the observation wells showing differential temperatures over the months. The first two wells showed temperature rise within the reservoir, whereas another well (situated south of the injector) remained cold.

## 2.4 Velocity and density change after steam injection

As steam was injected in the reservoir, not only did it displace oil, it changed the physical properties of the *in situ* fluid. Ideally, at the injector well, the steam will form a chamber near the perforation, increasing the oil temperature and decreasing the viscosity and displacing oil (Chopra, 2010). During this heat transfer, a part of the steam loses its latent heat and is changed into hot water. In the early stages of steam injection, it is quite likely to have more hot water in the injector than steam, a condition known as poor steam saturation.

There was no dipole sonic measurement after the injection (Pers comm. Kiyashchenko, 2013). The model velocities were calculated using Gassman substitution and FLAG modeling. Figure 2.10 is a plot of the available compressional and shear velocity log from dipole sonic tool from injector and the modeled (computed) changed velocities after the injection of steam. We observe a reduction in  $V_P$  and increase in  $V_S$  after steam injection (marked as  $V_{P\_monitor}$  and  $V_{S\_monitor}$  in the plot). The operator reported a density drop of 0.1 gm/cc and  $V_P$  drop of 200 m/s that was used for in-house analyses (Kiyashchenko and Maamari, 2010). Figure 2.11 shows a plot of  $V_P/V_S$  before and after the steam injection; there is a significant drop in the ratio as steam gets into the reservoir.

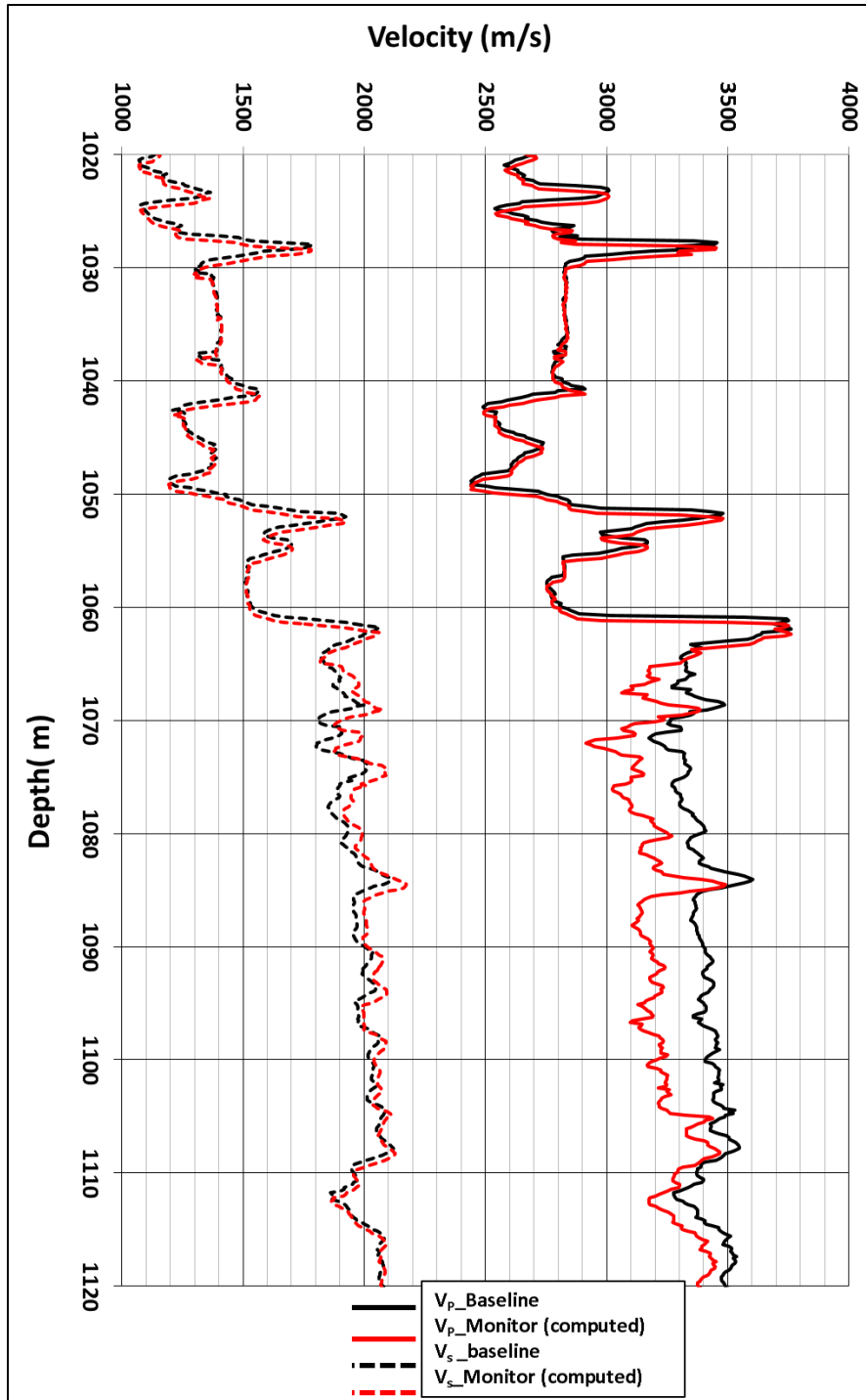


Figure 2.10: Compressional and shear velocity log before (marked as baseline) and computed velocities after (marked as monitor) steam injection.

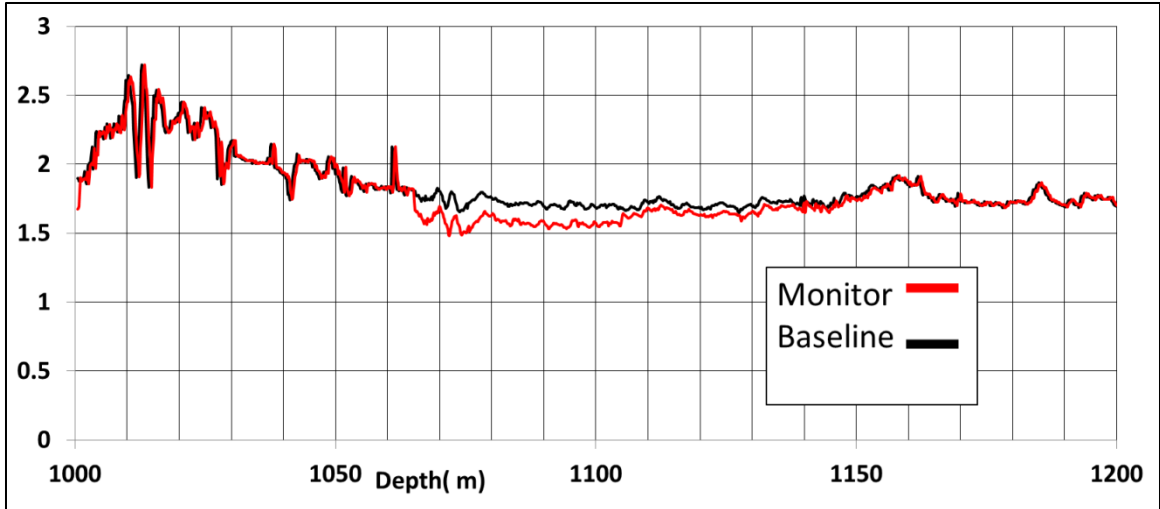


Figure 2.11: Change in  $V_p / V_s$  due to steam injection. Monitor velocities are computed from the baseline velocities, which are measured at the injector before steam injection.

## 2.5 Lambda-Mu-Rho plot (LMR)

The expression of  $\lambda \cdot \rho$  and  $\mu \cdot \rho$  (LMR) parameters has been used as key lithology and fluid indicators in quantitative AVO interpretation (Goodway *et al.*, 1997, Goodway, 2001). LMR analysis can be used to discriminate between lithologies and assist in understanding fluid effects, due to the separation in responses of both the  $\lambda\rho$  and  $\mu\rho$  sections to gas sands versus shales. In some reservoirs, it is possible to separate lithologies at an even finer scale to identify wet sands from shales and carbonates. This could become particularly important in steam-flood and injector planning to identify the optimum zones to inject fluids (Anderson and Grey, 2001).

We created a *lambda* ( $\lambda$ ) – *rho* ( $\rho$ ) and *mu* ( $\mu$ ) - *rho* ( $\rho$ ) crossplot, where  $\lambda$  is Incompressibility and  $\mu$  is Rigidity (Lame-Parameter). The expression of LMR is obtained by P and S impedance ( $I_p$  and  $I_s$ ) combinations as follows:

$$\lambda\rho = I_p^2 - 2 * I_s^2 \text{ and } \mu\rho = I_s^2 ,$$

where

$$V_s = \sqrt{\frac{\mu}{\rho}} \quad \text{and} \quad V_p = \sqrt{\frac{(\lambda+2\mu)}{\rho}} \quad (2.1),$$

where  $V_s$  is shear velocity and  $V_p$  is compressional velocity.

We used the density and velocity logs prior to the steam injection and calculated  $\lambda$ ,  $\mu$  and  $\rho$ . In Figure 2.12, we plotted LMR at depth intervals of 900 m to 1100 m and computed and plotted the LR and MR for the Haradh interval only after the steam injection (dark yellow). We note that the LMR ratio decreased as steam was injected to the reservoir.

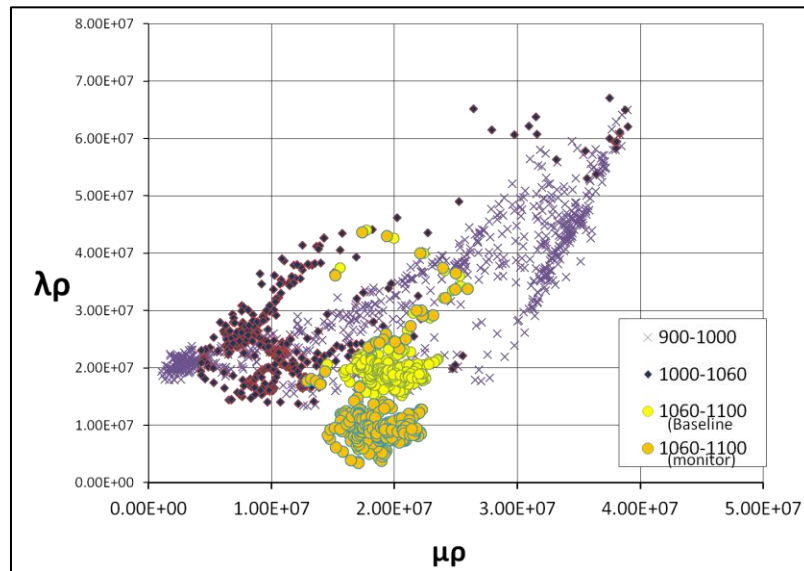


Figure 2.12: LMR plots for the injector well. Target zone is plotted again after recalculating with changed parameters due to steam.

## 2.6 Rock and fluid model

In the TL study we mainly measure the changes within a reservoir. To capture changes in TL reservoir modeling, we require an understanding of the fluid properties as a function of temperature and pressure on the dry rock and density–velocity trends for the target reservoir. These parameters are derived and described below.

## 2.7 Fluid properties

The velocity of a porous rock is a function of the properties of the rock matrix, as well as the fluid in the pore spaces and changes in the fluid properties. The relevant properties are density, acoustic velocity, and bulk modulus (Mavko, *et al.*, 2003). Before the steam injection, the reservoir fluids are heavy oil (19 API) and formation water. The steam injection resulted in a strong heating of the formation fluids as they interacted with the injected steam. The reservoir in this case did not produce any secondary gaseous hydrocarbons because the bubble point pressure for the oil is very low (500 kPa). We used the FLAG software (FLAG 11). The most reliable *in situ* fluid density information comes from wire line tools, but in the present case the values are compromised because the field is in production. The salinity is about 5000 ppm NaCl equivalent. For such a low salinity, the fluid properties are not sensitive to the precise fluid composition and the salinity. The steam that was injected was accompanied by a fraction of hot water in the liquid phase containing some salt. In the course of the steam injection project, the average salinity of the water in the reservoir, therefore, gradually declined. But because of the low salinity, the effect on the water density and velocity was small enough to ignore.

Properties of the oil present in the reservoir are taken from the Shell internal report, which covered several wells in the field area (SIEP EP2009-3190). The oil properties, at standard conditions of 15 °C and 101 kPa, are found in Table 2.2.

Table 2.2: Oil properties of Field “A”, Oman.

<b>Oil density 935.6 kg/m<sup>3</sup></b>
<b>Gas Oil Ratio (GOR) 1 m<sup>3</sup>/m<sup>3</sup></b>
<b>Gas gravity relative to air 1.357</b>

Because the GOR is small, the acoustic fluid properties will be rather insensitive to the gas gravity. Using these input values, we modeled the oil and water properties with the FLAG software. The results are displayed in Figures 2.13.a-c.

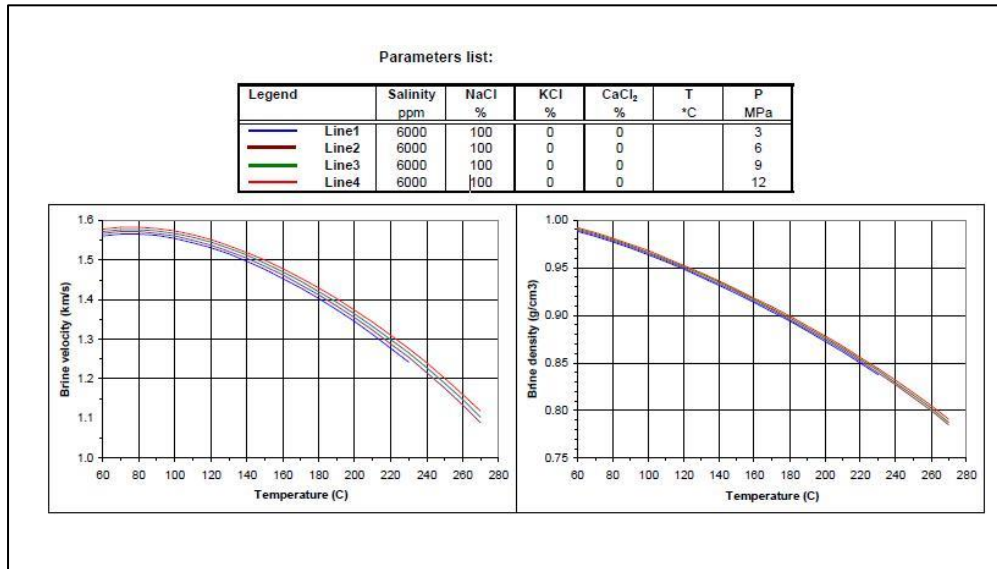


Figure 2.13.a: Brine properties as a function of temperature and pressure.

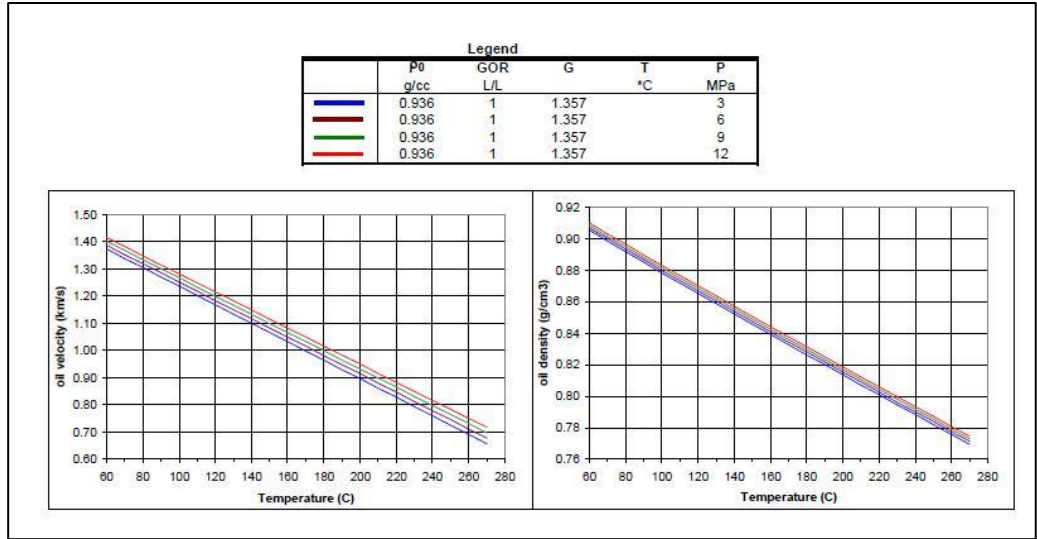


Figure 2.13.b: Oil properties as a function of temperature and pressure.

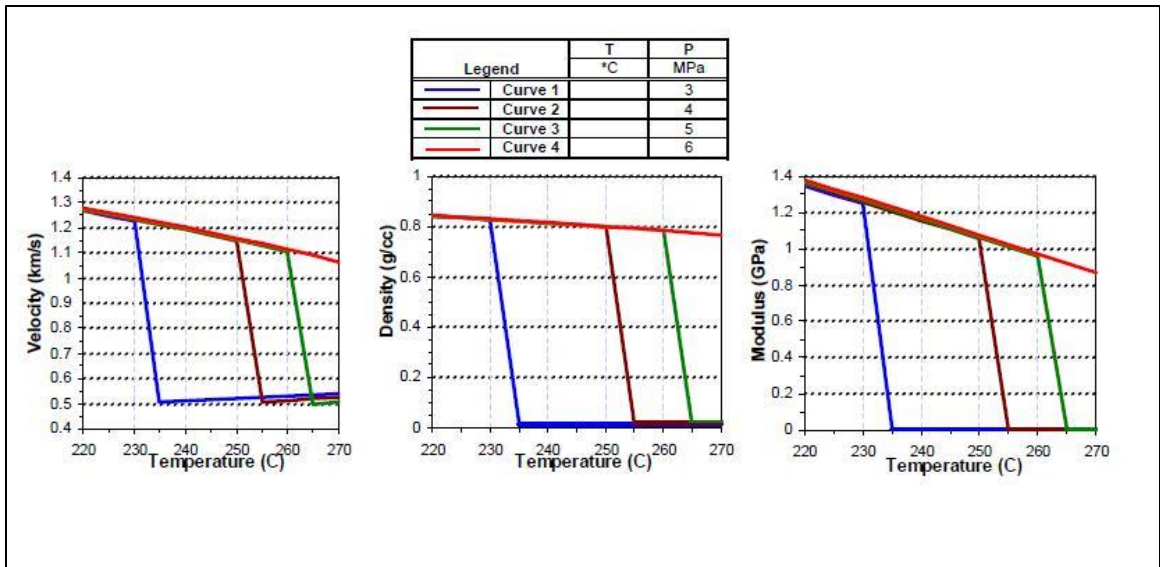


Figure 2.13.c: Properties of fresh water and steam as a function of temperature and pressure.

## 2.7 Rock velocities as function of density

We used the compressional and shear data for the well crossplot (Figure 2.10). Crossplots of velocity versus density for the oil-bearing zone and water-bearing zones are presented separately in Figure 2.14 and they are cloudier in nature than being a trend. The regression fit is calculated and separate equations are calculated for oil- and water-bearing zones. The equations are:

$$V_P = 5496.9 * \text{Density} - 9126.5 \quad (1); \text{ and,}$$

$$V_S = + 0.73565 V_P - 537.8 \quad (2),$$

where  $V_P$  is the P-wave velocity in m/s and (bulk) density is in g/cm<sup>3</sup> and  $V_S$  is the S-wave velocity.

The equation is quite similar to the mud-rock line (Castagna, 1985), which states that  $V_P = 1.16 V_S + 1360$  for water-saturated clastic rocks. The constant changes empirically for different basins, however (Castagna and Backus, 1993).

These expressions are similar to those mentioned in Shell's internal report and are further used during reservoir model scenario generation in Chapter 3. The internal report also mentioned the ultrasonic velocities of the core plugs at *in situ* stress amounted to  $V_P \approx 3720$  m/s and  $V_S \approx 2120$  m/s. For the sample porosity of 26 percent, these velocities are about 20 percent higher than the trend derived from the log data (SIEP EP2009-3190).

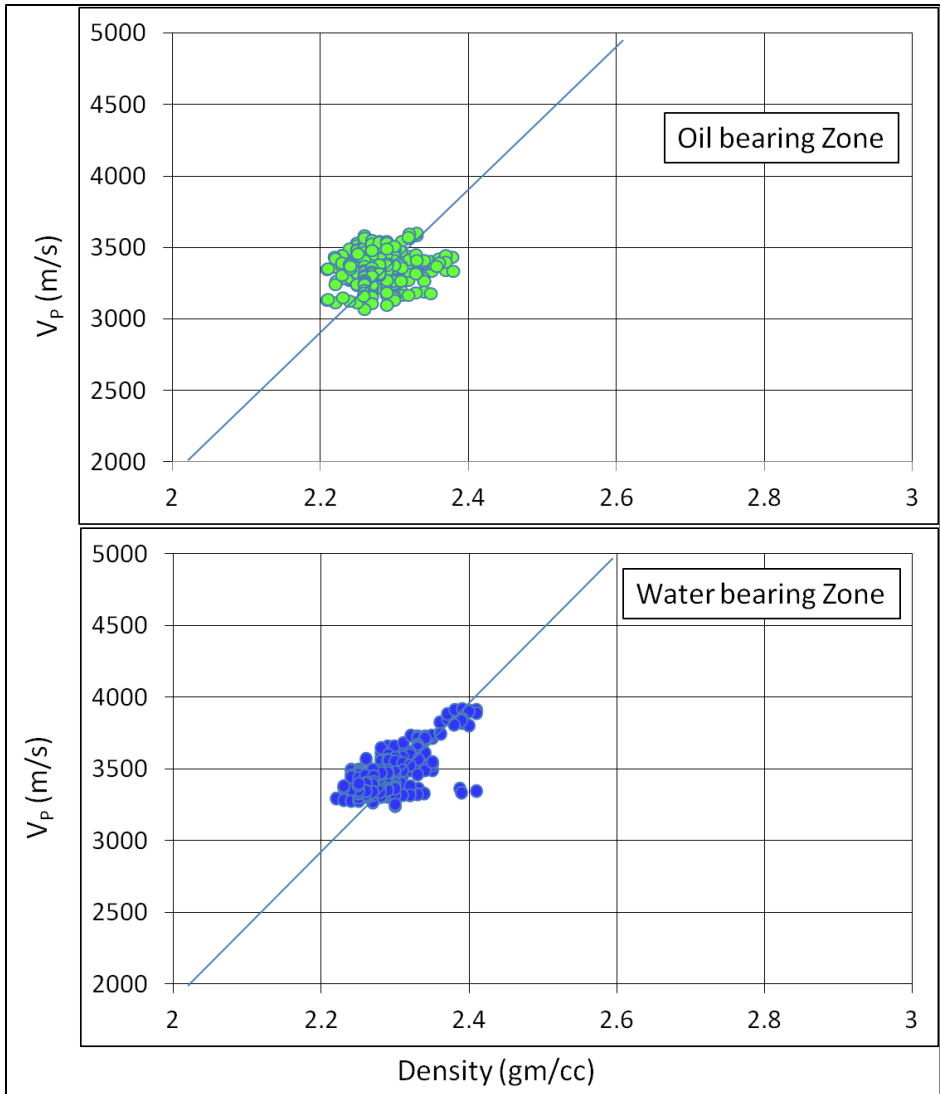


Figure 2.14: Crossplot of velocity versus density for the oil bearing zone (upper panel) and water bearing zone (lower panel). Equations used are  $V_p = +5477.116 \cdot \text{density} - 9074.37$  and  $V_p = 5477.116 \cdot \text{density} - 9074.34$ .

## Chapter Three: “Closing the loop” on the reservoir model update

### 3.1 Introduction

As steam is injected into a reservoir, it alters the petrophysical properties, including velocity and density, of the reservoir over time. The general practice is to observe the temperature response and draw conclusions about the permeability distribution within the reservoir. Different permeability distributions, however, can give rise to similar temperature profiles. A range of dynamic reservoir models need to be considered to decrease this uncertainty. For a specific EOR area, several dynamic reservoir models that are capable of giving similar temperature responses should be considered to identify the scenario that best matches the TL seismic response. We have developed an iterative approach to “closing the loop” based on scenario modeling (Mukherjee *et al.*, 2012).

Figure 3.1 describes the methodology with the help of a flow chart. TL synthetic seismic data generated from a “Reference” reservoir model was considered as simulated “data.” The synthetic seismic data could have been generated in various ways, including zero-offset convolution with reflectivity and full wave-field propagation. As described in the right portion of the workflow in Figure 3.1, we generated zero-offset convolutional synthetics. We also generated several scenarios as variances of the same “Reference” reservoir model, in terms of permeability distribution. Similar to the “Reference” reservoir model, for each scenario, acoustic properties were computed from the reservoir properties along with rock and fluid models (Rocco *et al.*, 2010). These acoustic



As an outcome of this comparison, we were able to select the scenario whose synthetic time-lapse seismic response best fits the data, and either use that as the new “Reference” reservoir model, or modify the existing “Reference” reservoir model to match the selected scenario. This step concluded one iteration of the loop; the loop may need to go several times for complete model modification.

We executed this loop using simulated data for the purpose of this study, but the workflow can and should be exercised on field data, especially after each monitor seismic survey, to refine the reservoir model and make it most representative of the subsurface. We used this close the loop (CtL) methodology in an EOR field in southern Oman, where production is being enhanced by steam injection. As part of the in-well surveillance program, temperature data are collected at regular time intervals. These data are used as a constraint in generating the scenarios of the “Reference” reservoir model. As we already mentioned in Chapters 1 and 2, temperature readings in a few producing wells suggested that the steam propagates preferentially to the north, indicating the possibility of a highly permeable connection between the injector well and well P4 (Figure 3. 2).

We took a “Reference” reservoir model created by the reservoir engineers of the operating company. They created this model based on the geological information and petrophysical input from the well control points. Figure 3.3 shows a map and profile view of the temperature front in the “Reference” reservoir model for baseline and monitor vintages. Comparison of the temperature measurements at wells with that modeled in the reservoir model indicates that they do not match. Such discrepancies inspired us to think about a few scenarios (variances of the “Reference” model) that would honor the existing

temperature data and identify the scenario whose permeability distribution matches that of the “Reference” model in the zone of interest; hence, CtL.

We set forth the process of model building, synthetic generation, and methods of comparison in following sections.

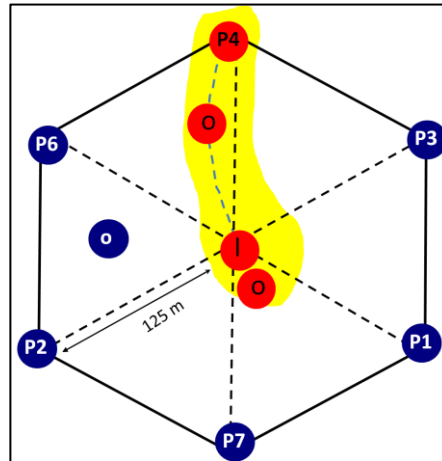


Figure 3.2: The steam injection pattern outline: ‘P’ is producer wells; ‘O’ is observation wells; and ‘I’ is injector well. Red indicates hot wells at the time of monitor surveys.

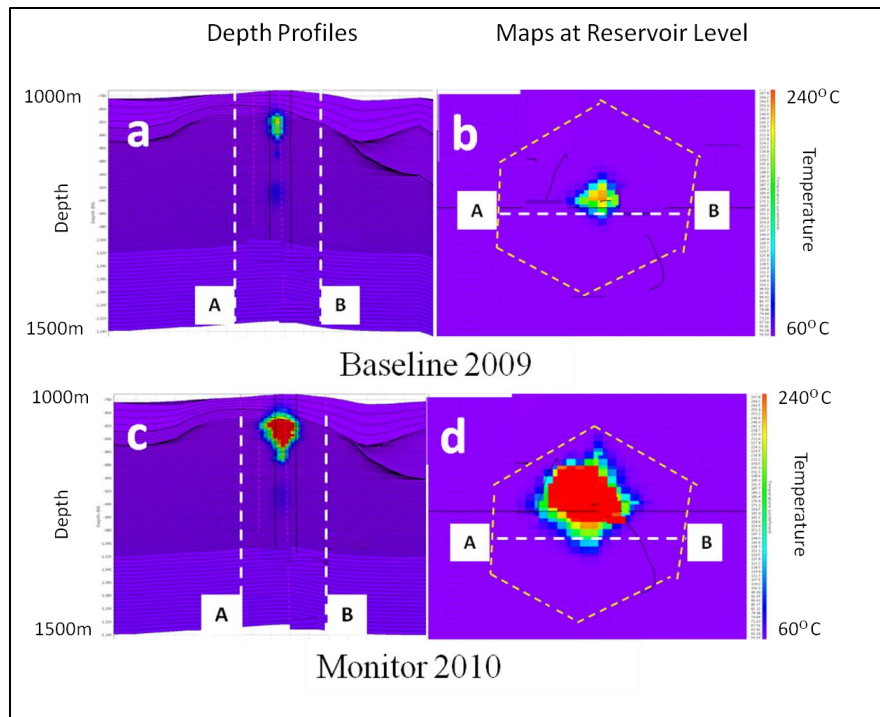


Figure 3.3: Temperature profiles and maps of Reference Model for two time vintages: a) temperature profile for baseline 2009; b) map view of temperature for baseline 2009 at the reservoir level; c) temperature profile for monitor 2010; and, d) map view of temperature for 2010 monitor at the reservoir level.

## 3.2 Methodology

In the following sections, we describe the process of making synthetic seismic data from reservoir models.

### 3.2.1 Import Model

The first step of the workflow was to import the dynamic reservoir model. This dynamic reservoir model is the output of reservoir modeling and includes 3D volumes of temperature, pressure, porosity, steam saturation, brine saturation, and oil saturation for different time vintages. The reservoir engineers, using the production data, determined

these time-stamps. Figure 3.3 shows the temperature profiles over years; we note that the steam fronts got bigger from baseline to monitor. The growing steam front is indicated by temperature increase around the injection well. The temperature scale for all the sub-figures goes from 60°C to 240°C. As the steam injection progresses, the steam saturation inside the steam zone increases and the oil saturation decreases.

### **3.2.2 Import Horizons, Wells, and Real Surface Seismic Data**

After importing the dynamic reservoir model, real well logs, seismic data, and some of the known horizons are imported into the model. The well logs are digitized around known horizons in order to generate realistic over- and under-burden acoustic properties ( $V_p$ ,  $V_s$ , and density).

### **3.2.3 Add Realistic Overburden/Underburden**

We next discretized the imported well logs in order to add realistic over-burden and under-burden to the reservoir model (generating similar cap rock and reservoir below the target zone). Blocked  $V_p$  and density logs from the well were used for generating the realistic overburden.

### **3.2.4 Insert Fluid and Rock Properties**

The fluid properties imported in the dynamic reservoir model included fluid saturations. There is an increase in the temperature and the fluid modulus, while density decreases with increases in temperature. Hence, we expected the fluid density and modulus to reduce in the steam injection zone. We used the Hertz-Mindlin model to relate the dry rock moduli to the pressure effects. For this part of the study, we selected a

Hertz-Mindlin exponent of 1/3. The fluid modulus and dry rock modulus were combined to give the bulk modulus.

Because the P-wave velocity is directly proportional to the square root of the bulk modulus ( $K$ ), we used the following expression to estimate the P-wave velocity ( $V_P$ ):  $V_P = \sqrt{(K + 4/3\mu)/\rho}$ . Using this P-wave velocity and the bulk density, we calculated the acoustic impedance (AI). The presence of steam caused the AI to decrease; therefore, the steam injection zone is characterized by low AI.

Further, while discussing the scenarios, we demonstrate the effect of two different  $K_v/K_h$  (vertical and horizontal permeability) values showing the effect of varying  $K_v/K_h$  on temperature, oil saturation, and AI.

In the modeling, we used the following grain and properties: temperature is 250°C; oil density is 783 kg/m<sup>3</sup>; oil velocity is 750 m/s; steam density is 26 kg/m<sup>3</sup>; steam velocity is 498 m/s;  $V_{P \text{ grain}}$  is 5443 m/s;  $V_{S \text{ grain}}$  is 3464 m/s;  $\rho_{\text{grain}}$  is 2656 kg/m<sup>3</sup>; and, overburden is 22618000 P.

### **3.2.5 Resample, Depth-to-Time conversion, and synthetic seismic data generation**

After the rock and fluid models were calculated, we converted the existing P-wave velocity profiles from depth to time. Using these time profiles of P-wave velocities and densities, we computed reflectivity and generated zero-offset synthetic seismic data. The wavelet was extracted from the surface seismic acquired in 2006; the synthetics generated here are surface seismic data, not VSP.

### 3.3 Description and Analysis of Scenarios

The six scenarios used here differ from each other and from the “Reference” reservoir model in terms of their permeability distribution, or presence or absence of shale layers acting as baffles within the reservoir. Each scenario is made of layers characterized by different grid sizes. Once the structure is defined, we assign petrophysical values to each grid point. The terms “top thick” and “top thin” are used to describe permeability distribution in the models. In a “top thick” model, the grid size is bigger in the top layers and decreases with depth, allowing steam to propagate more to the top and less to the bottom layers. Conversely, in a “top thin” model, the grid size is smaller at the top and increase with depth, making steam propagate more to the deeper layers. Figure 3.4 shows the top thick and thin models.

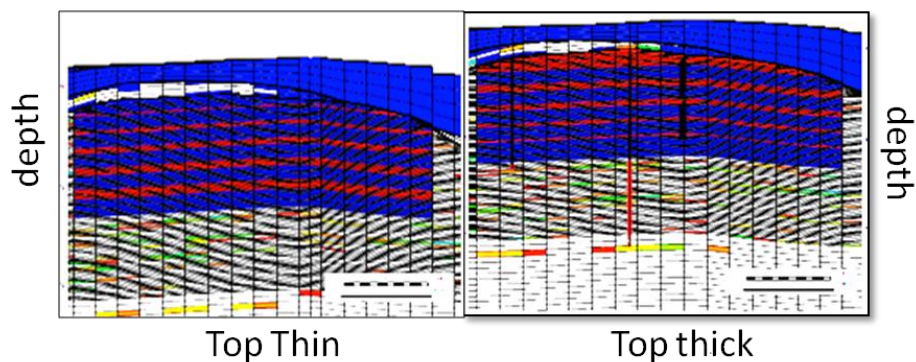


Figure 3.4: Different  $K_v/K_h$  gives rise to top thick or thin permeability distribution in the reservoir.

In total, we generated six different scenarios; details for each scenario are listed below.

1. Scenario S2: Horizontal permeability for the top few layers within the reservoir are overwritten to 10 D. Such a highly permeable model helps to visualize high steam within the reservoir, but is not realistic.
2. Scenario S3: Horizontal permeability gets modified to generate a temperature profile according to the temperature log data. Scenario S3 has a top thick permeability distribution, which means the permeability in shallow layers is higher than in deep layers.
3. Scenario S4: Horizontal permeability is modified to generate a temperature profile according to the temperature log data, but bottom horizontal permeability is higher to give it a top thin look.
4. Scenario S5: Scaled version of S3 (top thin), where the absolute permeability of the imposed layering are reduced by a factor of 10.
5. Scenario S6: Scaled version of S4 (top thin), where the absolute permeability of the imposed layering are reduced by a factor of 10.
6. Scenario Sb: There are many 0.5 m thick baffles introduced, honoring the regional geology at the reservoir level.

In Figures 3.5 to 3.7, the panels show the temperature, oil saturation, AI map, and seismic data for both baseline and monitor for all the scenarios. The panels in Figure 3.8 show the synthetic seismic data generated using the convolutional model. The right panels of Figure 3.8 show the seismic data plotted on top of the temperature profiles. TL acoustic properties for each of the scenarios and the “Reference” reservoir model were computed separately. After computing acoustic properties, we calculated their

reflectivity, which we then convolved with a source wavelet (extracted from existing surface seismic data) to generate zero-offset TL synthetic seismic data. We next compared the seismic data generated from the scenarios to the “data” (synthetic seismic data from the “Reference” model). Figure 3.9 shows the difference between baseline and monitor seismic data for our data and each of the scenarios.

We observe that scenarios S3 and S4 look more like our “data,” while S6 and Sb have the least similarity.

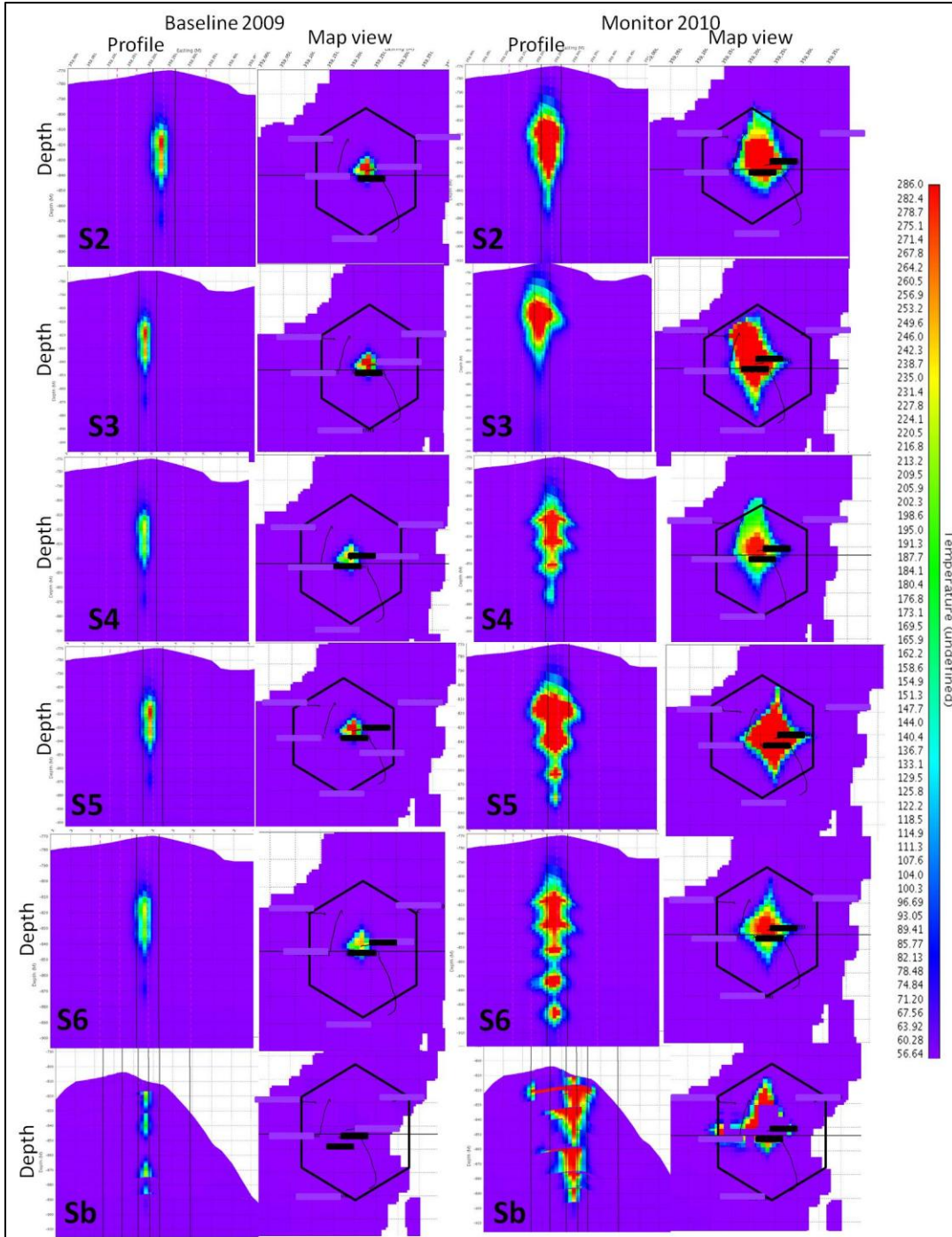


Figure 3.5: Temperature profiles and maps for two time stamps (baseline and monitor) for all scenarios labeled as S2 to Sb. We observe how the shape of steam changes for different permeability distributions.

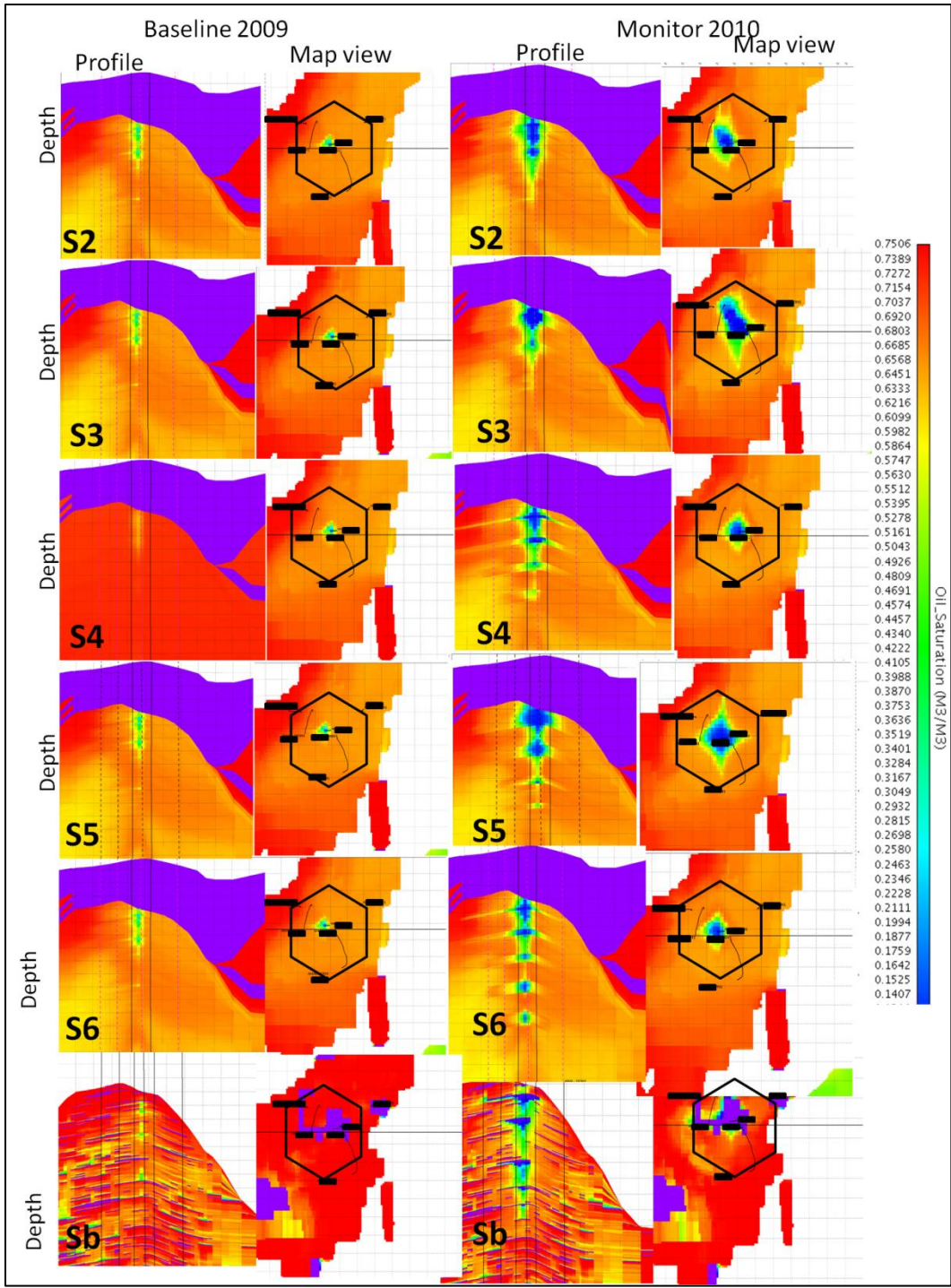


Figure 3.6: Oil saturation profiles and maps for two time stamps (baseline and monitor) for all scenarios labeled as S2 to Sb. We note how steam replaces oil as time increases.

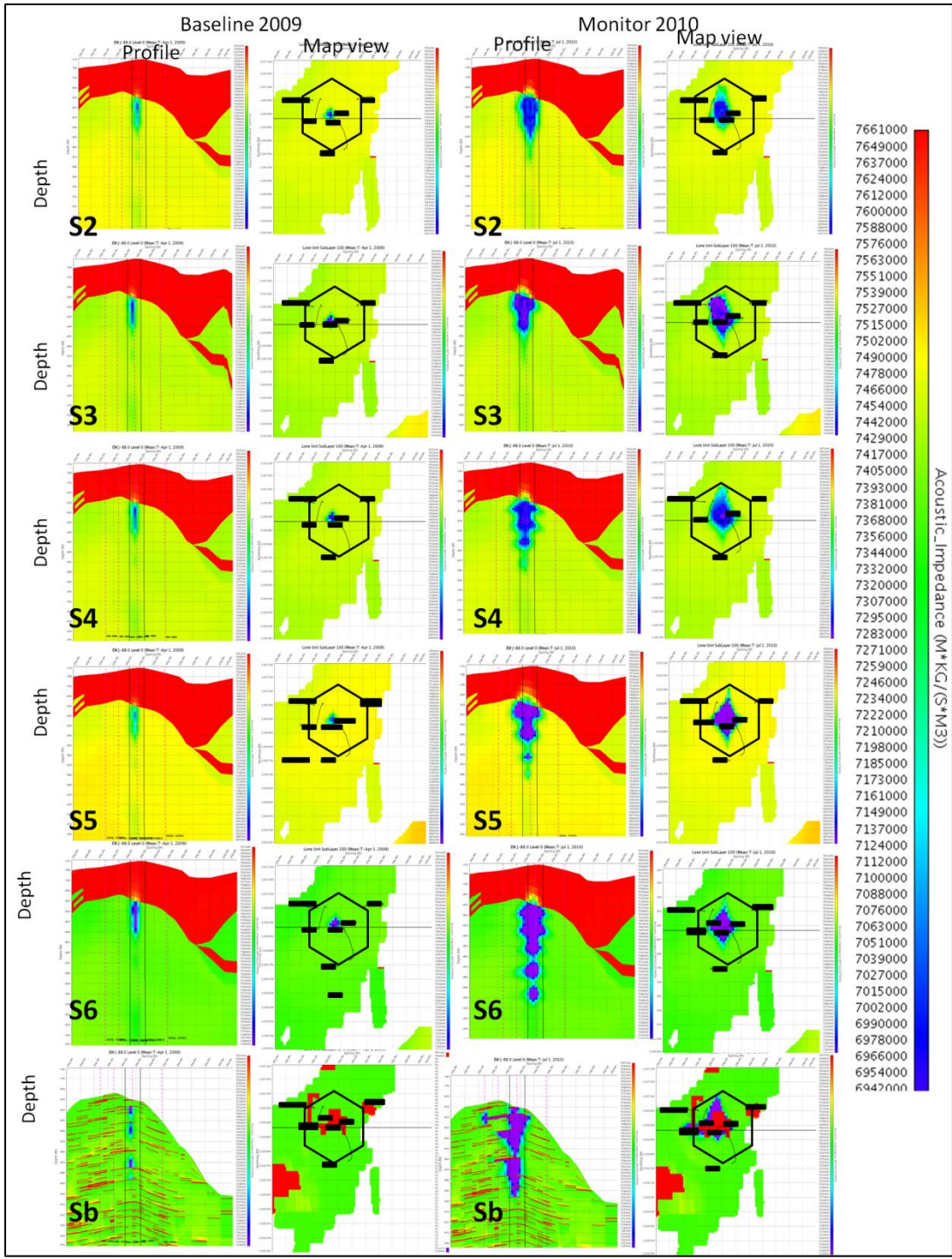


Figure 3.7: Acoustic impedance profiles and maps for two time stamps (baseline and monitor) for all scenarios labeled as S2 to Sb. As velocity and density changes with steam, the AI is changed.

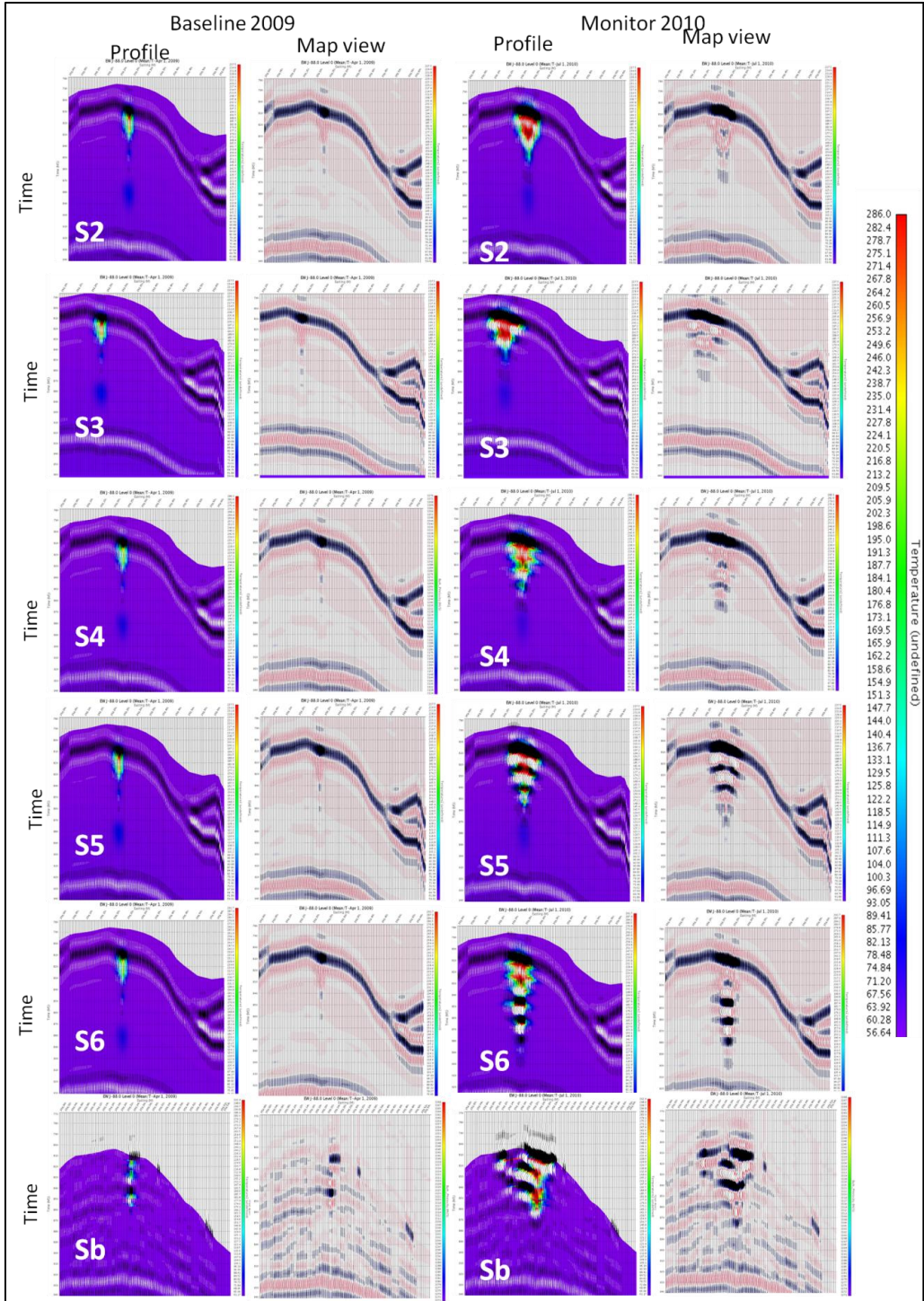


Figure 3.8: Synthetic seismic data generated for the scenarios. The right panel shows the seismic data overlaid on the temperature map.

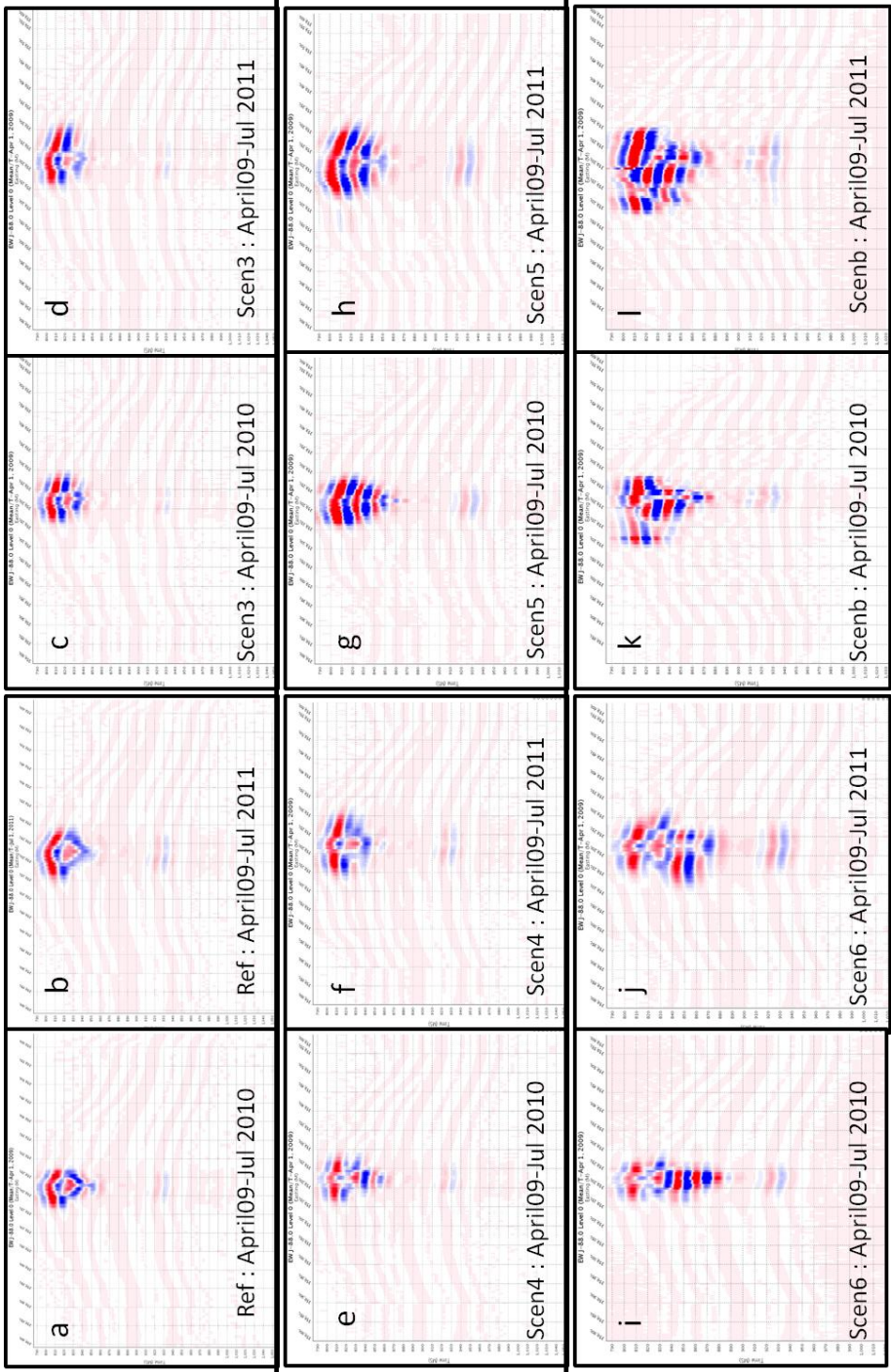


Figure 3.9: Difference of seismic data (baseline - monitor). The reference data and all scenarios are plotted together; visually, Scenario 4 looks very similar to the reference data.

### 3.4 Time-lapse attributes and analysis

Seismic data attributes have been used in the industry since the 1970s and have evolved from simple instantaneous attributes performed on a sample-by-sample basis (Taner *et al.*, 1979) to more sophisticated multidimensional attributes, such as coherency and waveform classification (Marfurt *et al.*, 1998). Seismic attributes are often used in reservoir characterization studies and prove to be important qualitative and quantitative predictors of reservoir properties and geometries when correctly used (Chambers *et al.*, 2002). Comparing the calculated seismic attributes on consistent TL measurements can reveal dynamic changes in fluid distribution. In this chapter, we study a suit of 4D attributes designed by Paul Hatchel (of SIEP) on the synthetic dataset with the goal of quantifying 4D anomalies in the presence and absence of noise.

After creating the baseline and monitor synthetic seismic volumes for the “Reference” model and each of the scenarios, we calculated the TL responses in the form of 4D attributes. In order to visualize the TL effects at the reservoir level, we calculated the following seven TL attributes:

- 1) *Normalized RMS* of amplitude difference, also known as unsigned RRR (RMS Repeatability Ratio);
- 2) *Normalized difference of RMS* amplitude, also known as signed RRR (RMS Repeatability Ratio);
- 3) *The Difference of sum of negative amplitudes*;
- 4) *The Difference of sum of positive amplitudes*;

- 5) *Difference of RMS amplitudes;*
- 6) *RMS of amplitude differences;* and,
- 7) *Difference of peak amplitudes.*

Few abbreviations are used here; attributes are standard in seismic exploration and are described in the following section.

The root mean square (RMS) operator, also known as the quadratic mean, is a statistical measure of the magnitude of a varying quantity. It is especially useful when varies are positive and negative, *e.g.*, sinusoids, as is the case of seismic traces. It can either be calculated for a series of discrete values, or for a continuously varying function  $X_i = X(t_i)$ , in a given time window (t1-tN):

$$X_{\text{RMS}} = \text{RMS}(X) = \sqrt{\frac{1}{N} \sum_{i=1}^n X_i^2} \quad (3.1).$$

The corresponding formula for a function (or waveform)  $S(t)$  defined over the interval  $T < t < T'$  is given by:

$$S_{\text{RMS}} = \sqrt{\frac{1}{T'-T} \int_T^{T'} S^2(t) dt} \quad (3.2).$$

The normalized RMS difference (NRMSD) of two traces within a given time window is expressed as follows (NRMS is usually expressed as a percentage):

$$\text{NRMSD} = 200 * \text{RMS}(T1-T2) / \text{RMS}(T1) + \text{RMS}(T2) \quad (3.3),$$

where T1 and T2 are the two traces that we want to compare in a given time window (t1-tN) and N is the number of samples in the interval (t1-tN). The maximum value possible for NRMSD is 200 percent.

The values of NRMSD are not intuitive and are not limited to the range 1 to 100 percent. For a time shifted sine wave:

$$\sin T = A \sin (2\pi ft) \text{ and } T_2 = A \sin 2\pi f(t+dt) \quad (3.4).$$

For a small scaling difference:

$$T_1 = F(t) \text{ and } T_2 = (1+a) F(t) \text{ we obtain } NRMSD = a .$$

In the particular case of TL seismic, the NRMSD operator has become a type of standard measure of repeatability used to quantify the similarity of two traces. It is often referred to in this context as RRR. The residual differences in the repeated TL data that are independent of changes in the subsurface geology impact the effectiveness of the TL method. These differences depend on many factors, such as source, streamer positioning, and recording fidelity. Such factors may be regarded as contributing to the TL noise. If the difference between the traces T<sub>1</sub> and T<sub>2</sub> is due to noise, we can write:

$$T_1 = S+N_1 \text{ and}$$

$$T_2 = S+N_2,$$

where, S represents the signal and N the noise. Since the RMS of the noise parts is the same, we can write:

$$N(1)RMS = N_2 RMS = NRMS, \text{ or}$$

$$RRR = \sqrt{2} \frac{100*NRMS}{\sqrt{S^2RMS - N^2RMS}} \quad (3.5).$$

In 4D, the sum of negative or sum of positive amplitudes (SNA or SPA) on given attribute time window, which usually extends from just above the top to just below the bottom of the reservoir, is a very common 4D attribute. Consequently, the DSPA and

DSNA attributes used in 4D seismic are defined as the difference of the SPA or SNA attributes between the baseline and monitor surveys:

$$DSPA = SPA (\text{Baseline}) - SPA (\text{Monitor}) \text{ and,}$$

$$DSNA = SNA (\text{Baseline}) - SNA (\text{Monitor}).$$

Of the seven attributes listed above, the first two, unsigned and signed RRR, are the most commonly referenced TL attributes. The purpose of looking at other attributes here is to illustrate that even though they may show similar shapes as the TL response, certain attributes are more appropriate for obtaining details about the TL response in some regions of interest.

Given that we worked with simple TL synthetic data, we examined the unsigned RRR for further qualitative study. For unsigned RRR, the values of this attribute ranged from 0 (no change) to 2 (maximum change). We suggest that for more complicated field datasets, all of the attributes listed above be analyzed for a comprehensive TL analysis.

We incorporated random white noise in the reference data to make it more comparable to field seismics. As the random noise level in the data was increased, it became progressively more difficult to follow the steam front. This is shown in the remaining panels of Figure 3.10 and 3.11, representing the TL response for three different noise levels, corresponding to RRR values of 0.19, 0.56, and 1.4. These RRR values are representations of the signal-to-noise ratio (S/N). As an example, at the incorporated noise equivalent to RRR of 1.4, it becomes difficult to identify the boundary of the steam. The amount of noise is defined using RMS RRR; the corresponding expression for S/N is given by:

$$S/N=20 \log \{1/(0.707*RRR)\} \quad (3.6).$$

### 3.5 Comparison Between Scenarios

Once the TL attribute maps were generated for the “data” and all the scenarios, we attempted to qualitatively compare them by looking at their shape, size, and amplitude distribution. For qualitative comparison, we selected a TL attribute (unsigned RRR) and visually compared the map for each scenario with that for our data.

Visual comparison in both map and profile view suggested that scenario S4 is the most similar to our data. Apart from visual comparison, three methods of quantification are used:

- 1) Similarity attribute;
- 2) Subtraction of maps; and,
- 3) Difference of energy.

The similarity attribute approach was discussed by Fomel and Jin (2009). This method provides a value of similarity between two data volumes or maps by computing the normalized zero-lag cross-correlation between them. The mathematical expression for this correlation is given by:

$$C = \frac{\sum_t a \cdot b}{\sqrt{\sum a^2 \sum b^2}} \quad (3.6),$$

where “a” and “b” are the two input datasets and “t” represents the number of samples. The value of “C” ranges between -1 (perfectly co-relatable but opposite polarity data) to 1 (perfectly similar). Figure 3.12 plots similarity attributes for each scenario, as compared

to the simulated data for time vintage July 2010. There are two similarity curves, one for the comparison of attribute maps and the other for comparison of seismic volume difference. For example, the similarity attribute for maps of scenario S2 with our data is about 0.83. Similar values for each scenario, both for map and volume comparison, are computed and plotted. Such analysis suggests that scenario S6 is most correlated to the simulated data, although only slightly better than scenario S5. Volume comparison, however, suggests that scenarios S4 and S2 are most similar to the simulated data. Given that our interest is generally in the region of injection (around the top reservoir level) and not in the entire reservoir column, we gave more weight to the results from the map views: here, S6 is the best fit, counter-intuitive to the initial observation. As the random noise level is increased to RRR=0.19, 0.56 and 1.4, the selection of the best-matching scenario using similarity value remains the same, although selection becomes increasing difficult (Figures 3.13 to 3.15).

Another approach to comparing synthetic seismic data from scenarios with the simulated data is to differentiate one TL attribute map from the other and compute the residual energy. When the two maps in comparison are more like each other, the residual energy is less. The six panels in Figure 3.16 show the differences of the RRR attribute maps of the simulated data from the RRR maps for each of the six scenarios (for time vintage April 2009 - July 2010). The panels in Figure 3.17 to 3.19 show similar plots with noise levels of RRR 0.56 to 1.14.

$$X = \sqrt{\frac{\sum_t (a-b)^2}{N}} \quad (3.7).$$

Out of the six scenarios, the residual energy for S6 is the least, both visually, and in terms of its RMS value.

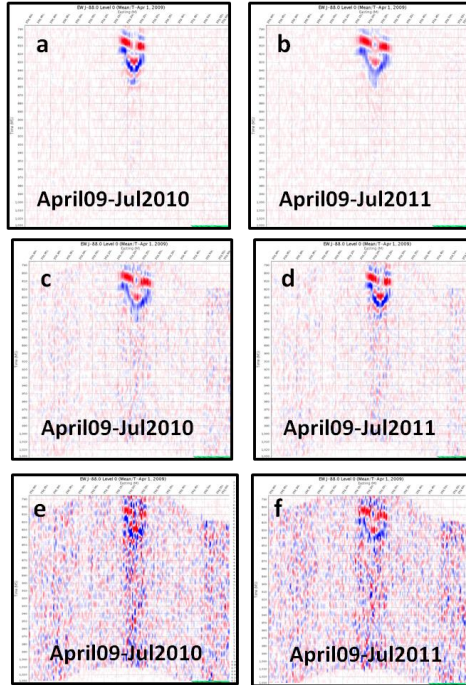


Figure 3.10: Difference of seismic amplitudes obtained from the Reference Model with noise levels corresponding to RRR=0.19 [panels (a) and (b)], RRR=0.56 [panels (c) and (d)] and RRR=1.14 [panels (e) and (f)]. The time vintages are labeled in the panels.

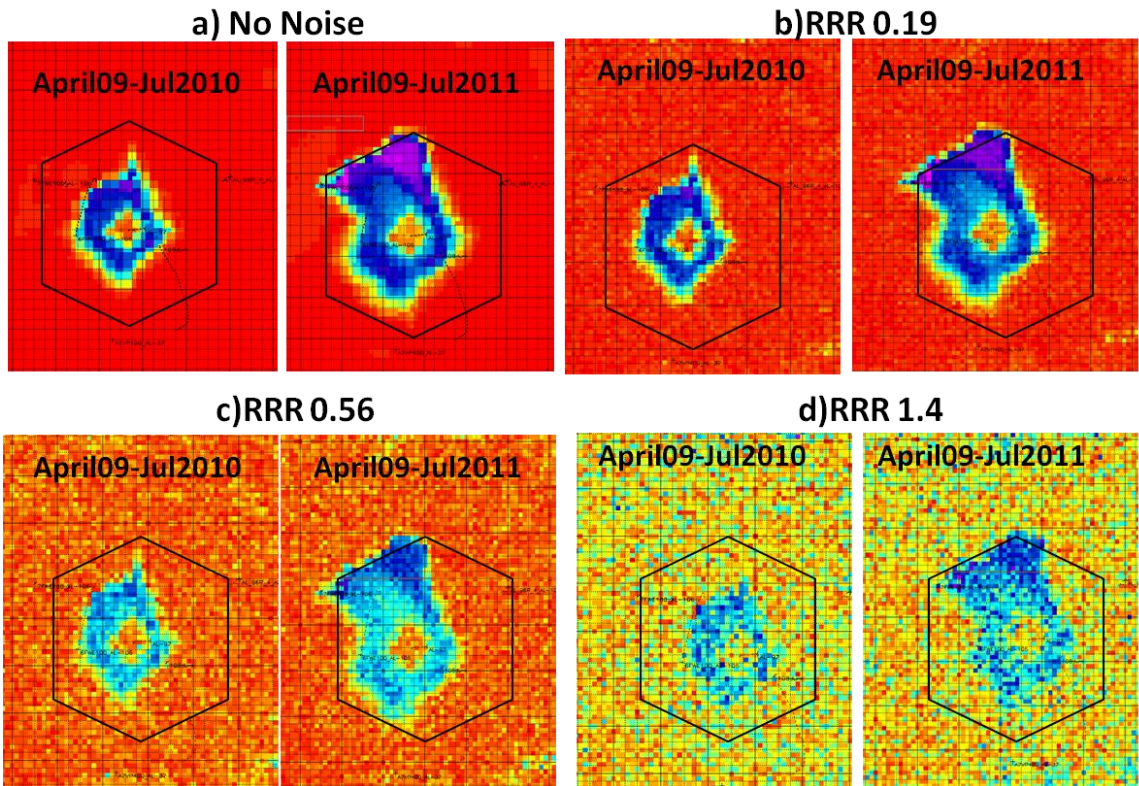


Figure 3.11: RRR attribute maps of TL seismic data obtained from the reference model. Each panel shows the attribute map for two time vintages and different noise levels, characterized by RRR (labeled on each panel).

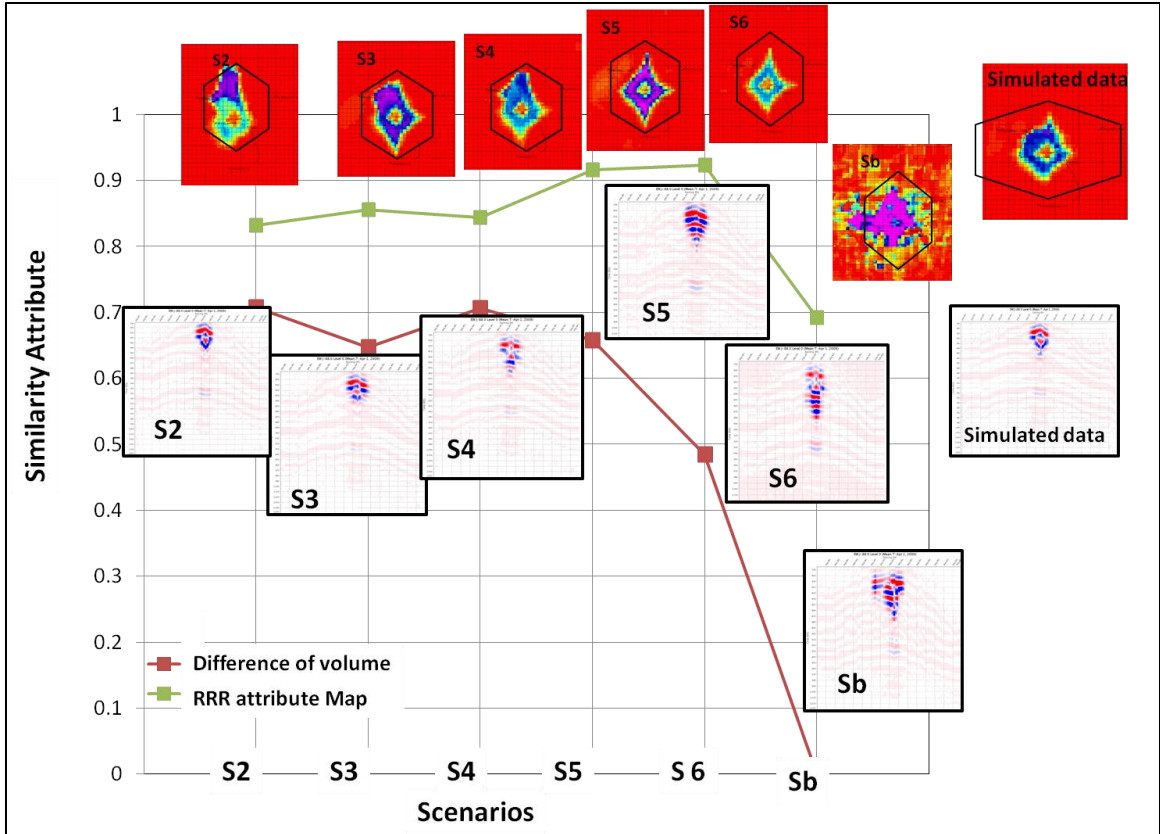


Figure 3.12: Plot of similarity attribute, for no noise case, as a function of scenarios. The two curves show similarity measure (in volume and map, respectively) of the data from the reference model and the scenarios for time vintage April 2009 through July 2010. The attribute maps and amplitude difference volumes that are used to compute the similarity attribute are shown for each scenario and the reference data.

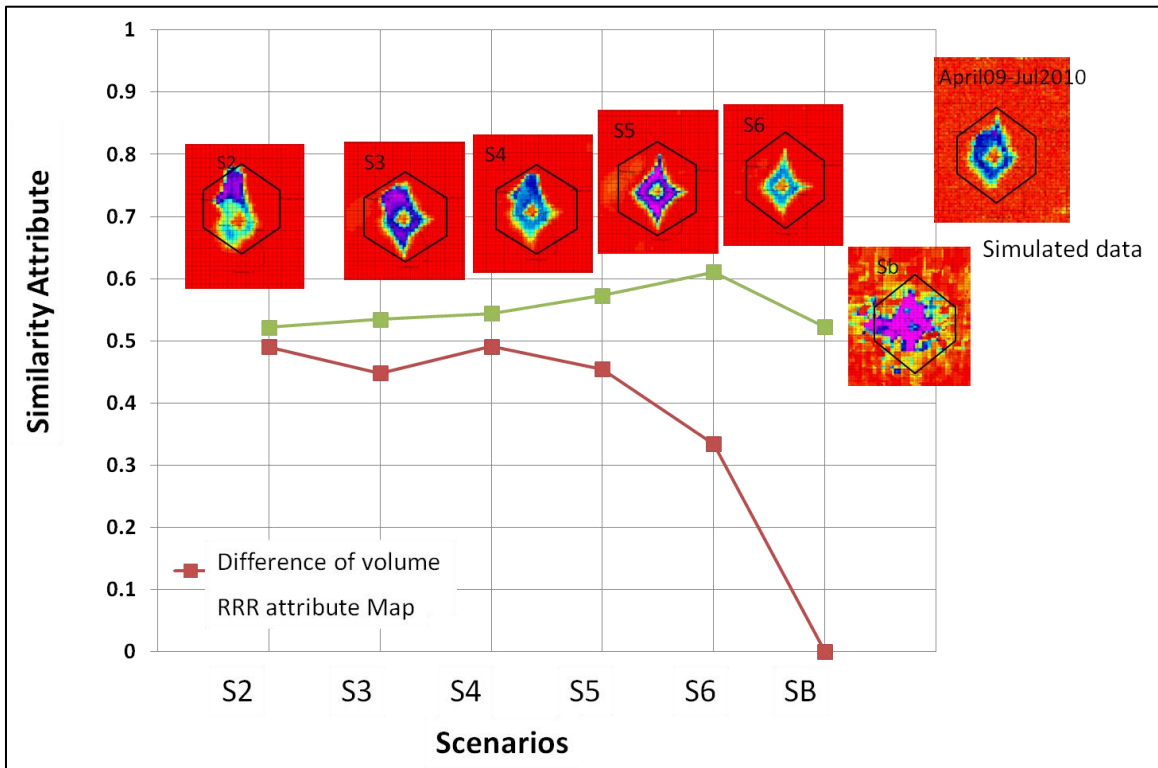


Figure 3.13: Plot of similarity attribute, for no noise case, as a function of scenarios. The two curves show similarity measure (in volume and map, respectively) of the data from the reference model and the scenarios for time vintage April 2009 through July 2010, with noise equivalent of  $RRR=0.19$ . The attribute maps and amplitude difference volumes that are used to compute the similarity attribute are shown for each scenario and the reference data.

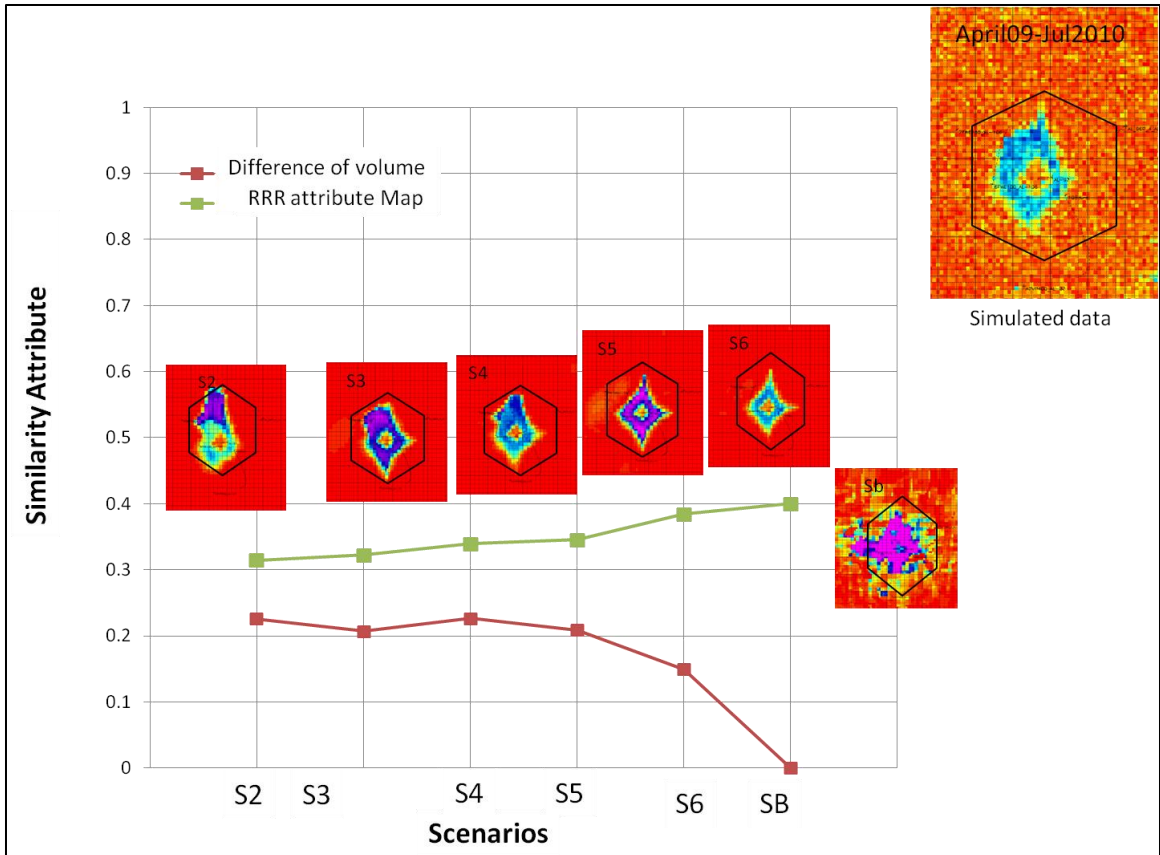


Figure 3.14: Plot of similarity attribute, for no noise case, as a function of scenarios. The two curves show similarity measure (in volume and map, respectively) of the data from the reference model and the scenarios for time vintage April 2009 through July 2010, with noise equivalent of  $RRR=0.56$ . The attribute maps and amplitude difference volumes that are used to compute the similarity attribute are shown for each scenario and the reference data.

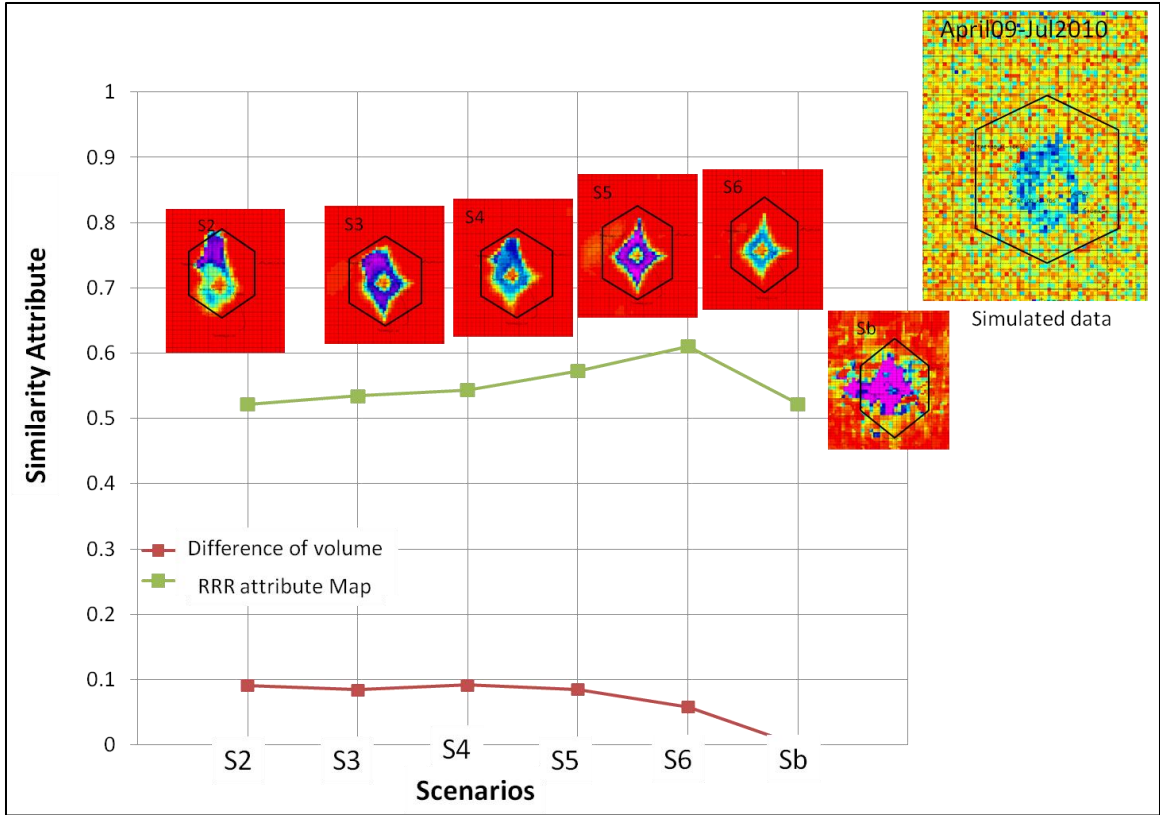


Figure 3.15: Plot of similarity attribute, for no noise case, as a function of scenarios. The two curves show similarity measure (in volume and map, respectively) of the data from the reference model and the scenarios for time vintage April 2009 through July 2010, with noise equivalent of  $RRR=1.14$ . The attribute maps and amplitude difference volumes that are used to compute the similarity attribute are shown for each scenario and the reference data.

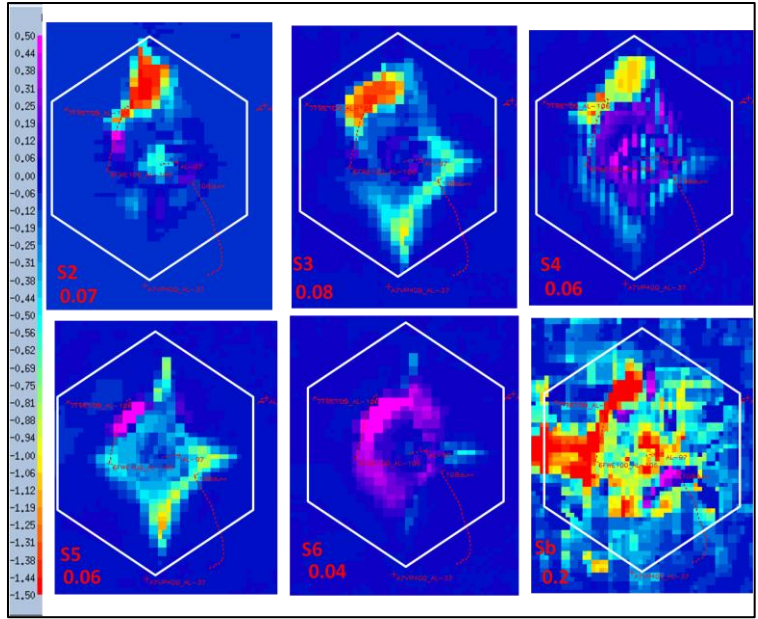


Figure 3.16: Difference of RRR attributes for all the scenarios and the reference data with no noise [time vintage April 2009-July 2010]. The numbers reflect the normalized RMS of the difference.

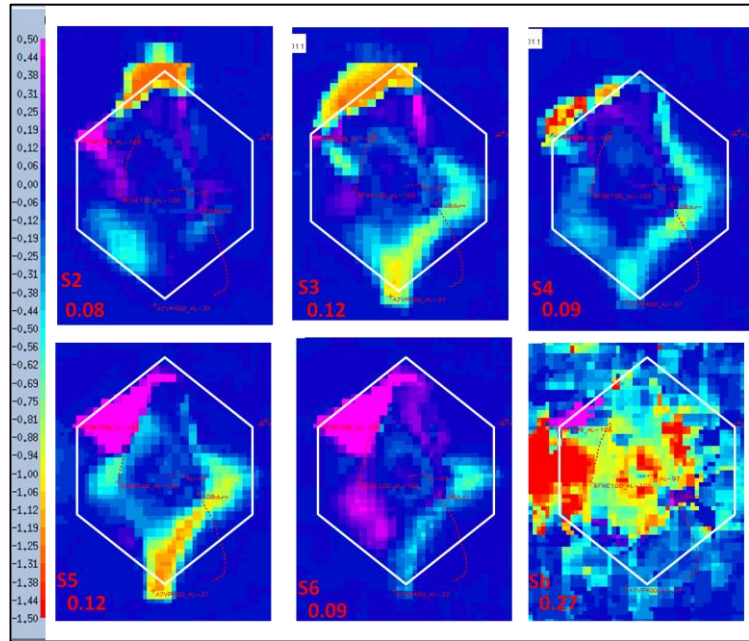


Figure 3.17: Difference of RRR attributes for all the scenarios and the reference data with no noise [time vintage April 2009-July 2011]. The numbers reflect the normalized RMS of the difference.

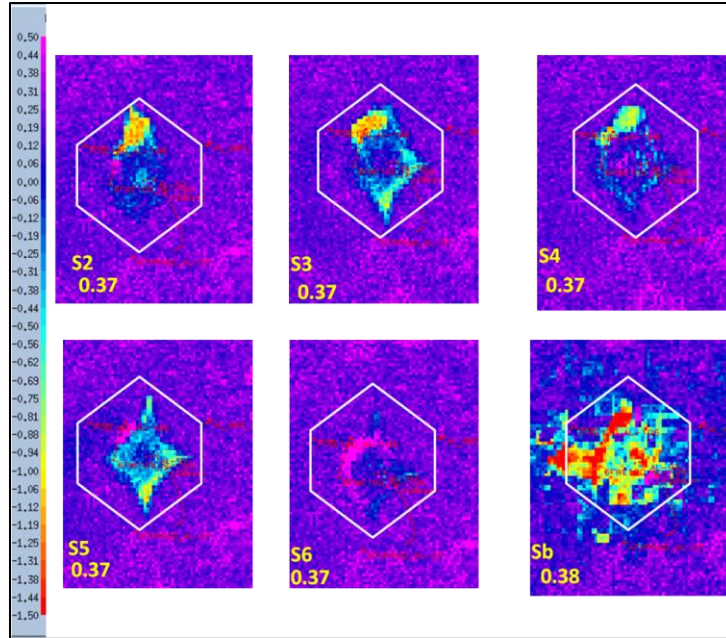


Figure 3.18: Difference of RRR attributes for all the scenarios and the reference data with no noise [time vintage April 2009-July 2010]. The numbers reflect the normalized RMS of the difference with noise 0.56.

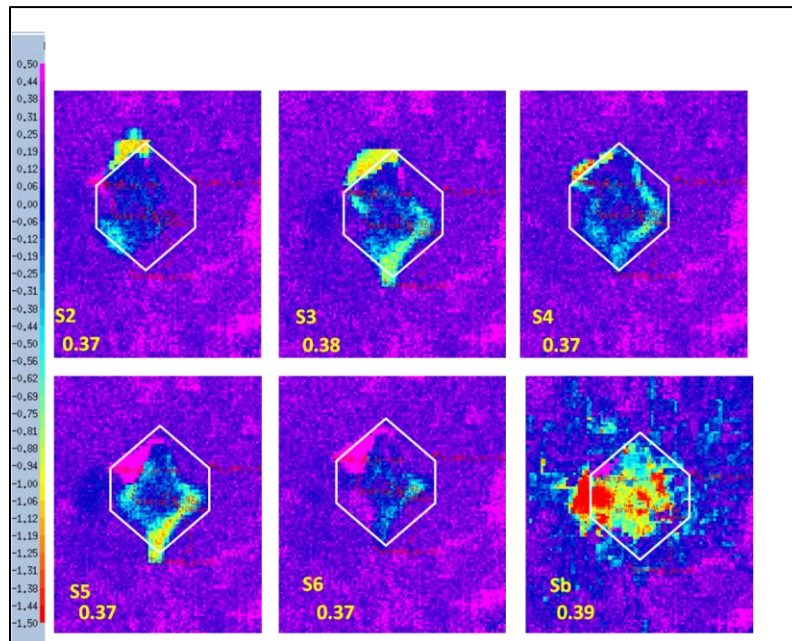


Figure 3.19: Difference of RRR attributes for all the scenarios and the reference data with no noise [time vintage April 2009-July 2010]. The numbers reflect the normalized RMS of the difference.

### 3.6 Results and summary

We executed a detailed workflow to CtL using synthetic data for a steam injection oil field in southern Oman. As a result, we are able to select a scenario S6 as the closest to our data. This selection is possible after careful quantitative comparison; it is counter-intuitive to initial observations. We note the following:

- 1) It is very important to consider a range of realistic scenarios that can give a similar temperature effect; and,
- 2) Scenario-based CtL, when carried out properly, helps identify the scenario that best honors the data, which may be counter-intuitive to initial observations.

We successfully established a quantitative CtL workflow that helps to select the most suitable reservoir model. Two quantitative approaches for attribute comparison concluded that both the similarity attribute and difference of RRR energy plot work consistently with each other to identify the scenario that honors the data and, hence, provides the most accurate representation of the subsurface. In the next chapter, we discuss processing synthetic VSP for PP and methodically working out processing ways to increase the S/N for TL cases with very low contrast (velocity change of 5 percent and density drop of 2 percent).

## **Chapter Four:** **Processing and interpretation of PP walkaway VSP model data**

### **4.1 Introduction**

We created a set of walkaway VSP data for baseline (April 2009) and monitor (July 2010) surveys using Wave Equation Modeling through a finite differences method. We used upscaled logs from the wells to generate this acoustic VSP. In this chapter, we discuss the required processing modifications and caution needed to perform better velocity estimations and obtain a clarified time-lapse signal. We later compare our results with commercially processed results.

### **4.2 WFD models for walkaway VSP**

WFD is Wave Equation Modeling code finite differences. The operator uses a prototype version of a finite difference code for modeling wave propagation program written by J.N. Buur and W.A. Mulder (1993-1994) in-house at Shell. This modeling can create surface or VSP seismic acoustically or elastically. It takes gridded velocities ( $V_P$  and  $V_S$ ) and density models as inputs, using Gardner's (1974) equations when there are no density models available. The shooting and recording geometry needs to be specified along with the grid size of the model. The source signature also needs to be specified. A boundary reflection, which is a common problem of modeling, can be regulated by adding extra points along model boundaries or making the model large with recording time.

The model generation time is proportional to the size of the input data, recording time, and number of extra points added in the model. Lastly, but most importantly, computation speed of the platform plays a major role in the model generation time. The flowchart in Table 4.1 explains the generic modeling flow for WFD.

Table 4.1: WFD modeling flow to generate seismic data

Step 1	Create the input data (velocity grid)
Step 2.	Setting up WFD parameter file <ul style="list-style-type: none"> <li>• Type of Equation (wave, acoustic, or elastic; size of the input model)</li> <li>• grids, add Vs and rho (for elastic models)</li> <li>• Boundary conditions: used to make absorbing boundaries</li> <li>• Free Surface</li> <li>• Extra points for absorbing boundaries</li> <li>• Sources and wavelets</li> <li>• Shot grid</li> <li>• Receiver grid</li> <li>• recording time interval</li> </ul>
Step 3	Run WFD ( in single machine or cluster)
Step 4.	Converting the trace files and view

### 4.3 Model generation

For this pilot project, the  $V_p$  from the well was scaled and laterally extrapolated to velocity models ( $V_p$ ) for both baseline and monitor. WFD modeling was done for a few selected shots from the WAW VSP line (K. Mehta, 2011). Acoustic WFD modeling results agree reasonably well with the active WAW VSP data in terms of direct arrival timing and moveout; corresponding P-wave reflections present in both modeled and field

data and can be identified in the smoothed logs. The field data are noisy for shallower receivers. There is a timing discrepancy between WFD modeled and field data for the far offset shots. This could be attributed to the inaccurate (layered) velocity model used to generate the modeled data. Otherwise, the synthetic results are very similar to the real dataset. Figure 4.1 shows the smoothed velocity profile used; panels in Figure 4.2 show the comparison of the WFD and field VSP for various shot points. Figure 4.3 shows the frequency spectrum of the modeled and field VSP for baseline and repeat.

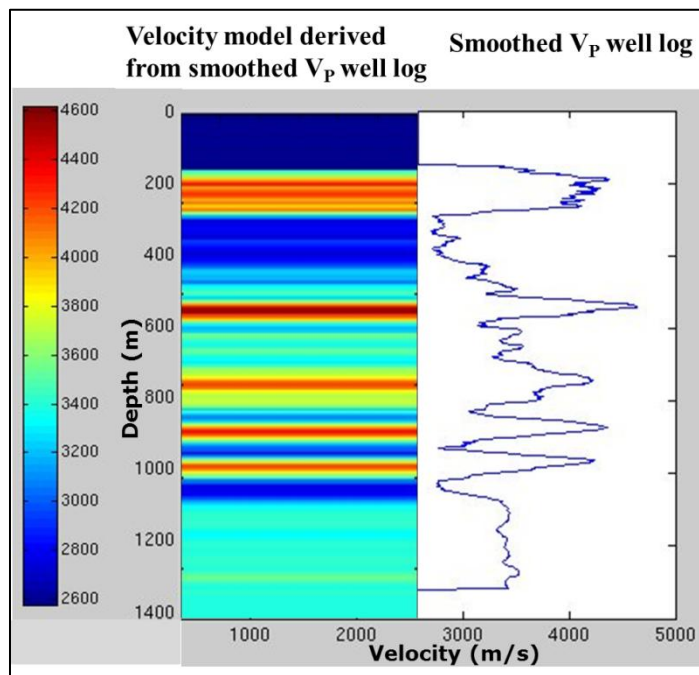


Figure 4.1: Smoothed P-wave and laterally extrapolated velocity profile for WFD model.

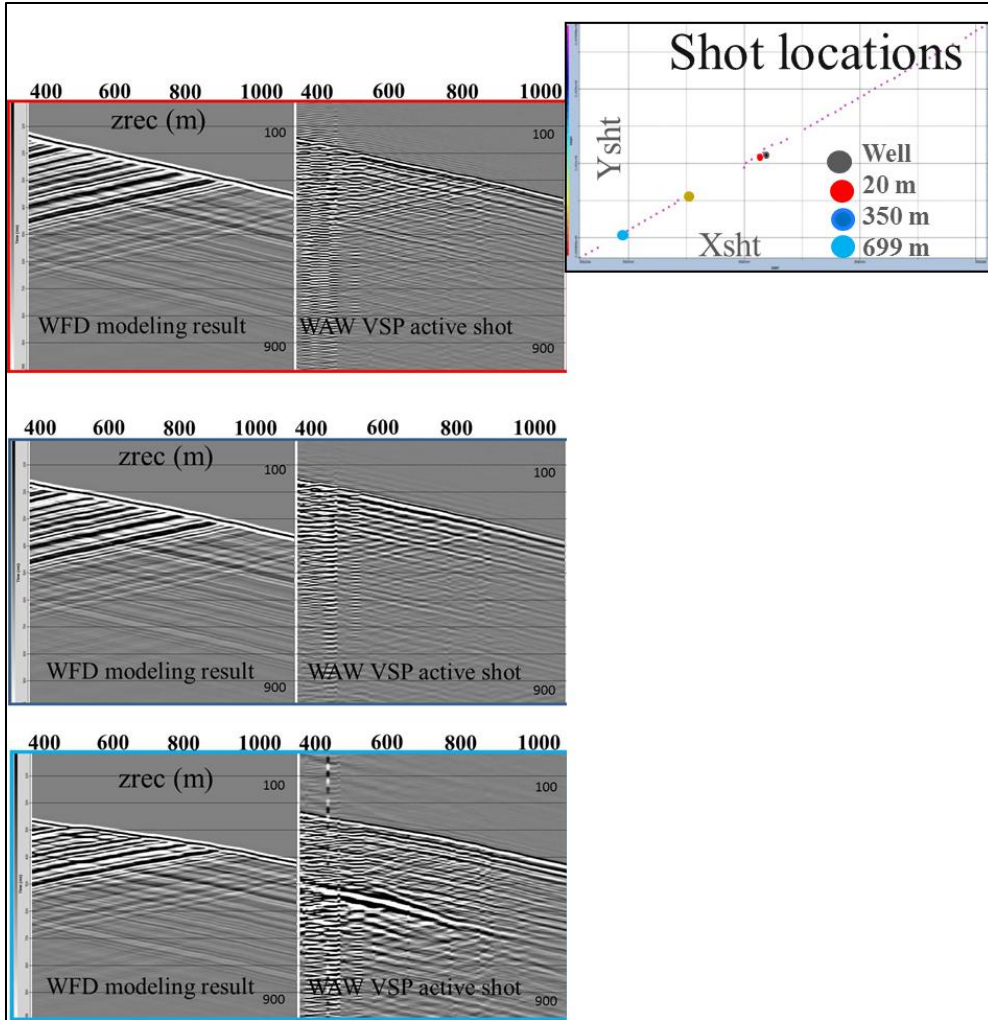


Figure 4.2: Comparison of synthetic and field VSP (left panels). At right, the P-wave velocity profiles are plotted for zero, mid, and far offset shots. Top inset shows the shot location with respect to the active wells.

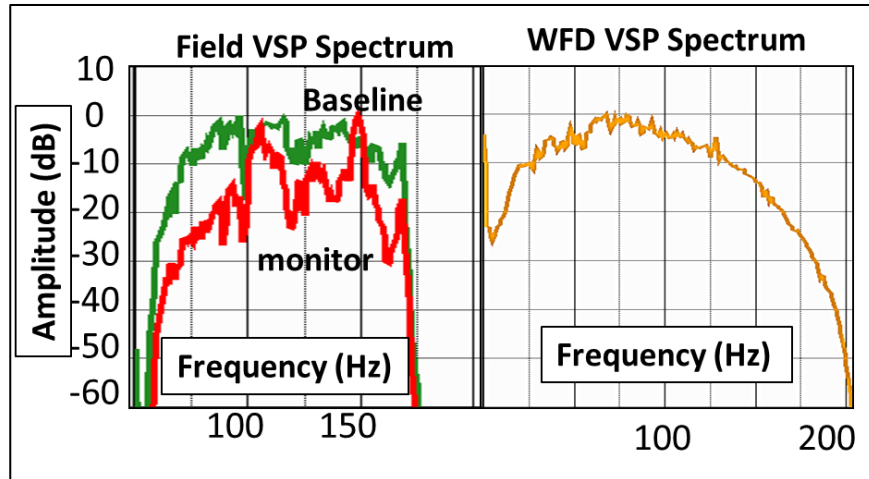


Figure 4.3: Frequency spectrum comparison of the field and synthetic VSP.

#### 4.4 VSP acquisition geometry

Table 4.2 describes the acquisition geometry of the walkway VSP.

Table 4.2: Acquisition geometry of VSP

Wellbore	Vertical well
Source Type	Vertical force
Receiver interval	7.5 m
Number of receiver	160
Total shot	149 (74 shots in each side and one on the top of the well)
Source interval	12.5m

There is no attenuation incorporated in the model, which causes a lot of multiples of the steam. The source wavelet was extracted from the field data and shown in Figure 4.4. Figures 4.5 and 4.6 show the velocity and density models for both baseline and monitor. Figure 4.7 depicts the schematic representation of the VSP geometry.

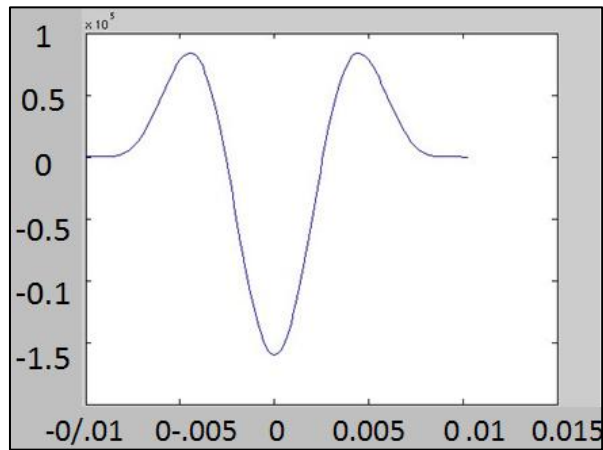


Figure 4.4: Source wavelet extracted from surface seismic data shot in 2006.

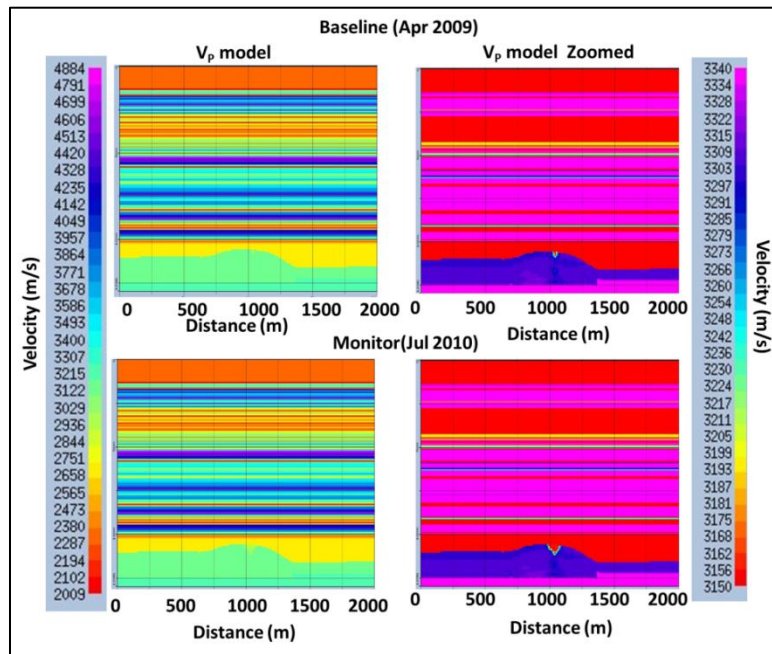


Figure 4.5: Velocity models for both baseline and monitor. Zoomed version shows the changed velocity due to steam.

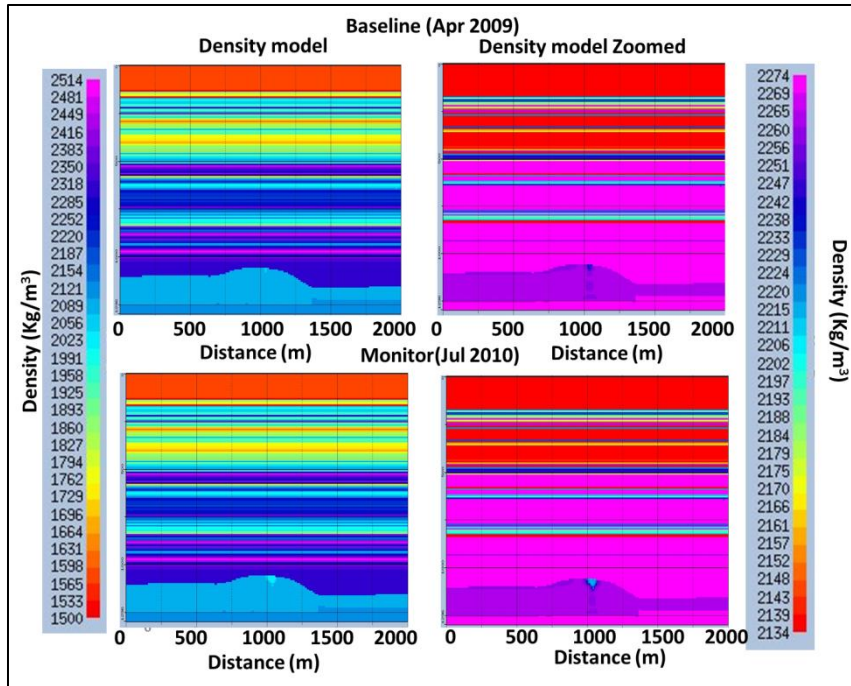


Figure 4.6: Density models for both baseline and monitor. Zoomed version shows the changed density due to steam.

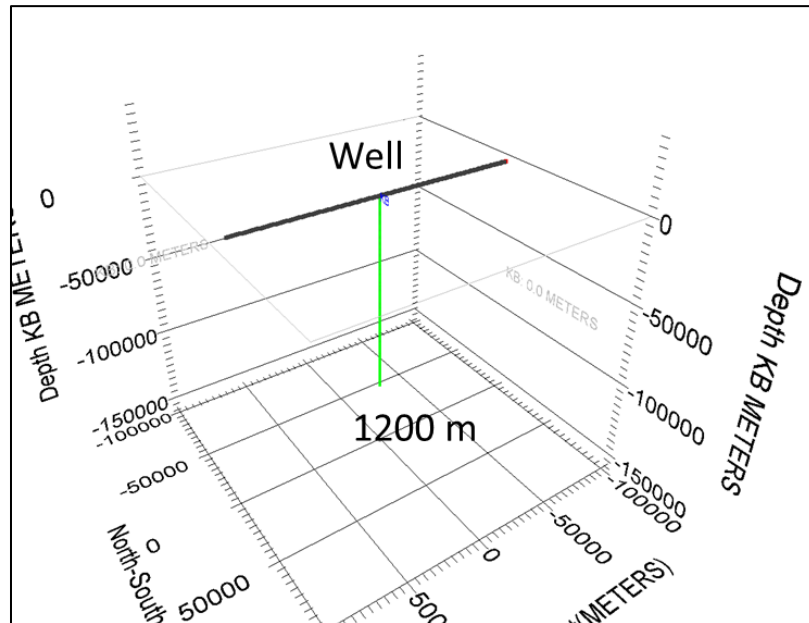


Figure 4.7: Schematic diagram showing VSP geometry.

## 4.5 Zero-offset VSP processing

Once the model was made, we took the zero-offset of Z component VSP shot gathers from both baseline (April 2009) and monitor (July 2010) in order to check the detectability of the anomalies in VSP. The model has -2% density changes and -5%  $V_p$  changes, with 0%  $V_s$  change. Additionally, we cross-checked the velocity inversions to develop an easy and robust technique to maximize the TL effect.

Figure 4.8 shows the zero-offset VSP data for both baseline and monitor, and a subtraction of those (monitor-baseline). The shot gather from baseline and monitor look very similar, almost identical. The frequency content is also the same with a dominant frequency (Figure 4.3) about 100 Hz. Once the baseline is subtracted from the monitor, the reflection from the top of the steam become visible. The last panel of Figure 4.8 shows the differences; we used AGC for better view purpose. Along with the reflection from the top of the steam, strong multiples of the reflections are also visible. Other than the section below receiver number 140 (1050 m), data are practically the same.

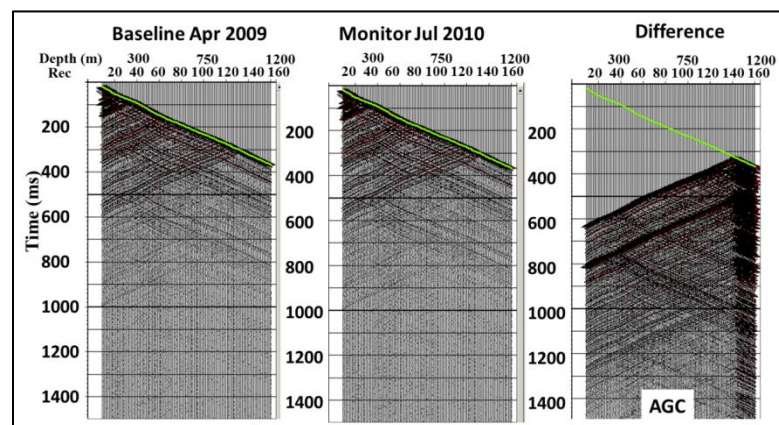


Figure 4.8: Shot gathers from baseline, monitor and the difference (AGC). The first break is plotted in green for visual purposes.

We then followed a methodology called interpretive processing (Hinds and Kuzmiski, 1996, 2001). In interpretive processing, the interpreters examine each step of the processing flow. More importantly, this approach allows the interpreter to fully examine the VSP data in the same manner as a quality control (QC) procedure for surface seismic data processing.

In this section, we discuss how the results affect the signal to noise ratio and change the results. The VSP flow for making a corridor stack is given in Table 4.3.

Table 4.3: Standard VSP processing flow for corridor stack

Load geometry
Horizontal rotation ( may be needed for horizontal components)
Pick fist arrivals (first break )
Align data on first arrival pick
Wavefield separation (separate upgoing and downgoing)
Deconvolution design
Deconvolve upgoing
Align upgoing
Build corridor
Stack

Once the VSP was loaded, we picked the first arrivals. To minimize error in picking, we picked five events near first breaks and inverted them for velocity. Those five events are :

- 1) First energy;
- 2) Peak;
- 3) Zero crossing;
- 4) Trough; and,
- 5) End of the wavelet.

For individual picking, shown in Figure 4.9). We assigned a small gate (20ms) around the event and used autopicking .

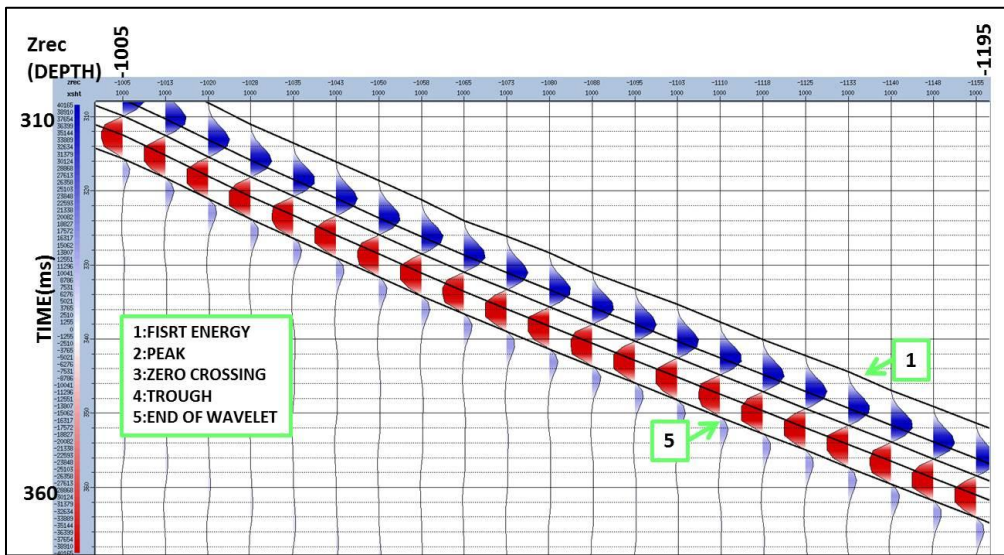


Figure 4.9: First, several breaks are picked manually and inverted for velocities; best matched are used in averaging.

Once autopicked, they are manually checked before inverting for velocities. In Figure 4.10, we have plotted all five inverted velocities over the model velocity for a comparison. We observe the matching is good for peak, trough, and zero-crossing inverted velocities where first energy and end of wavelet gave a lot of jitters. Once the first breaks were picked for baseline, we imported the picks at monitor and adjusted the

picks where necessary. Because there is no change in the velocities until the reservoir level, picks are practically the same. Picks only change at the reservoir level due to steam. Importing picks from baseline is a very common practice in TL processing because it minimizes processing time and background noise due to the overburden. Once velocities were calculated, we calculated the mean and median of the best three velocities. Averaging gives a better correlation than taking the median of the three velocities. Figure 4.11 shows a comparison plot of the model velocity and VSP velocities.

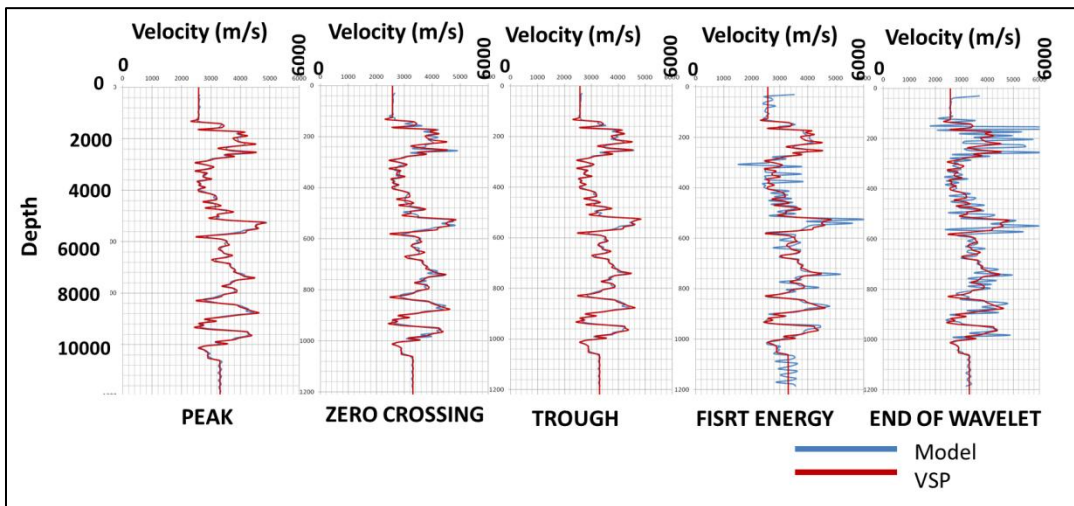


Figure 4.10: Shows velocity inverted from picks. The first three show good correlation, but the last two graphs shows considerable jitter.

We noticed that the VSP velocities are about 20 to 30 % lower than the actual model velocity. In Figure 4.11, we have plotted the difference of velocities (baseline-monitor) for model-derived (Blue) and VSP (Red). The actual drop in velocity is about 150 m/s, where in VSP it is about 110-120 m/s. The steam front appears shallower (1042 m) in VSP velocity, whereas it is originally at 1056 m in the model. This is due to the resolution discrepancy between modeling and VSP. In VSP, the receiver interval is at

every 7.5 m, whereas in the model we used log velocity, which has much more vertical resolution (Figure 4.12).

Once the velocity was calculated, we moved to the next step, which is wave-field separation. The data are flattened at the first break. We used a 13-point median filter to separate downgoing waves; upgoing waves were extracted by subtracting downgoing from the total wavefield. Once the wavefields were separated, we calculated a deconvolution operator using the downgoing wave. Figure 4.13 shows the deconvolution spectrum. After deconvolution, we improved the resolution correspondingly; Figure 4.14 shows a comparison between the upgoing wavefield before and after.

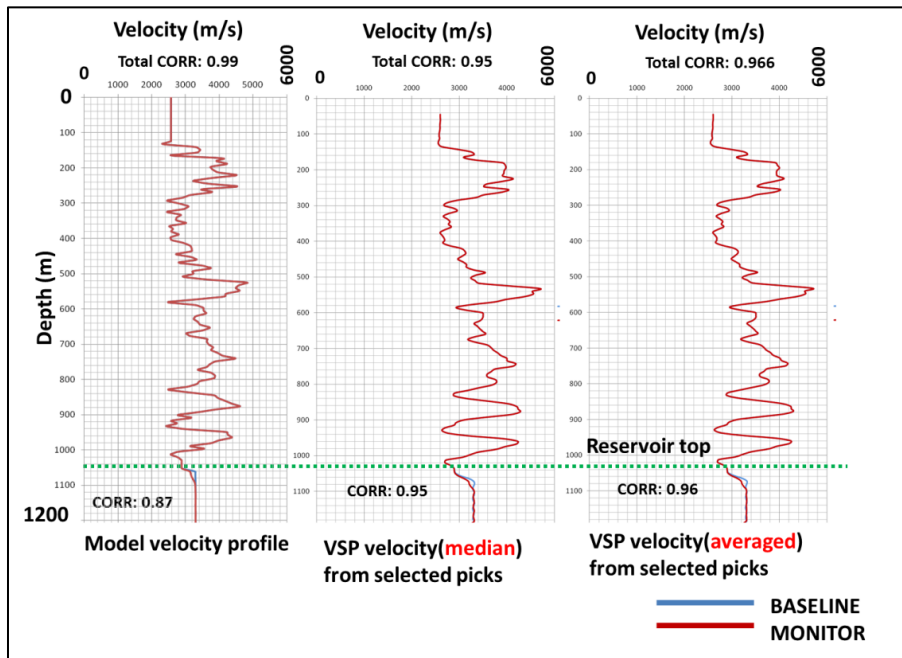


Figure 4.11: Left panel shows model velocities, exactly repeatable on the top and only differing at the reservoir level. Middle panel shows median VSP velocity; the finer details of the velocity change are missing in VSP velocity compared to model velocities. Right panel shows the average velocities; in this case, the correlation coefficient is higher than in median.

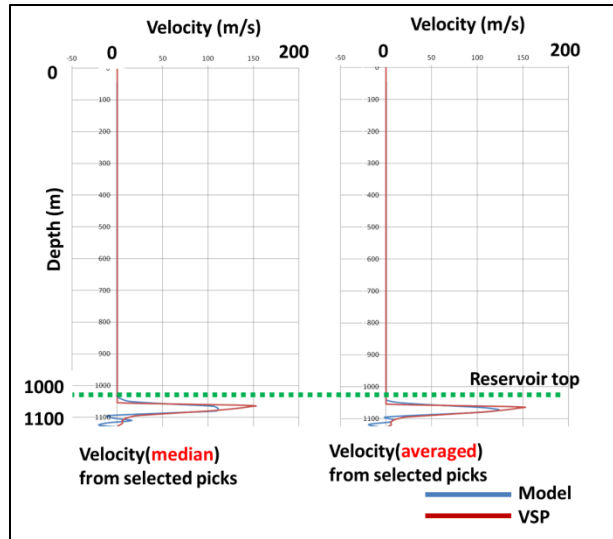


Figure 4.12: Plotting the difference, we note the match is much better than the manual pick. There is no anomaly on the top and the steam feature coincides. The steam front appears at 1048 m, whereas in the model it appears at 1056 m.

We then shifted the data to two-way travelt ime by applying first-arrival time-statics (Hardage, 1983). Considering the time lag of multiples, the upgoing wavefield recorded close to reflectors is assumed to be largely noise free. A 50 ms corridor mute was applied to the data to remove multiples and other noise. Once the corridor stack was made, the trace was repeated ten times for better viewing.

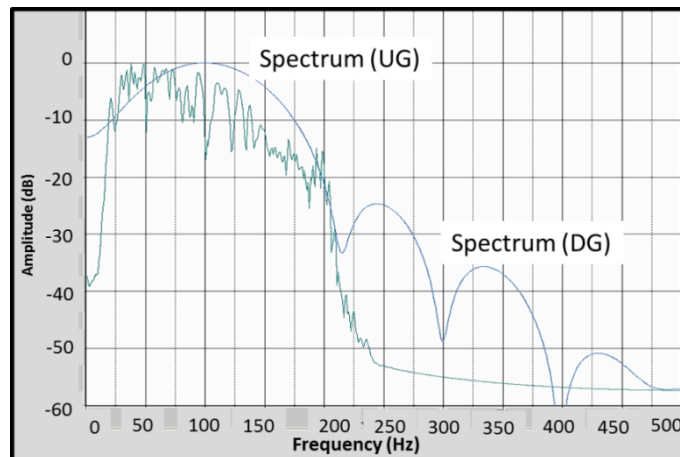


Figure 4.13: Deconvolution spectrum.

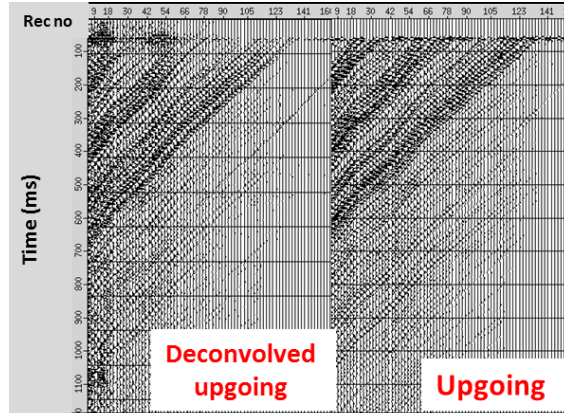


Figure 4.14: Upgoing before and after deconvolution.

We followed a similar processing flow to process the monitor (July 2010) data. Once the monitor corridor stack was made, time shifts were calculated, as discussed in the following section. We applied the time-shifts in the monitor corridor. Figure 4.15 shows the subtraction from monitor to baseline and normalized differences. We observe that TL response is nicely visible in the corridor stack; it also corresponds with the depth.

## 4.6 Time-shifts

The time-shifts between baseline and monitor surveys is a robust indicator of changes in the presence of wavelet differences and static shifts. Time-shifts are usually measured using a cross-correlation window. Here, we calculated the time-shifts through cross-correlation of baseline and monitor traces in a time window  $\Delta N$  samples above and below our analysis point at time “t”; “N” is known as the gate (Hatchel, 2010, internal report). The monitor trace by an amount  $(L+B)$ , where “L” is lag and “B” is lag bias; the cross-correlation coefficient is defined as:

$$\Phi_{ab}(t,N,L,B) = \int_{a(t+i*\Delta t)}^{b(t+(i+L+B)*\Delta t)} w(i)$$

where  $w(i)$  is a triangular filter, which is 0 for  $i=\pm N$  and 1 for  $i=0$ .

### 4.7 TL analysis

Once the time-shifts are calculated and applied to the monitor data, we performed TL analysis. A subtraction from the baseline to time-shifted monitor is the TL effect one expects to see. In Figure 4.15, we plot the subtraction. Here, the first time-lapse response comes from the reservoir level. We also observe changes below the reservoir because changed velocity affected the wavelet. A normalized TL (difference) corridor stack is also plotted to minimize reflection from the base of the model.

A RRR attribute was not calculated for the TL corridor stack window. For corridor stacks, it is not crucial to calculate 4D attributes, but, in the case of VSP images and maps, it carries significant interpretative value that will be discussed below.



Figure 4.15: The normalized difference in the corridor stack can be generated by dividing the true difference by the RMS of the monitor panel. The true difference is the subtraction of baseline from the time-shifted monitor.

## **4.8 VSP imaging for baseline and monitor**

After successfully generating corridor stacks, we processed the Z offset VSP to make images for baseline and monitor. Standard VSP flow was taken until the separation of the upgoing and downgoing for all offsets. After flattening the data at the first break, we performed median filtering to separate the data. Figure 4.16 shows panels of data separated for different offsets. The upgoing data volume will further used as an input in processing flows to generate images. It is very important to have the cleanest upgoing possible. We tried both FK filtering and median filtering to separate wavefields. We note that for near offset, both processes generate almost equal results; however, for mid and far offset, the median filter works better than FK. There is slight shear contamination in the upgoing, which is suppressed in further processing and discussed later in this section.

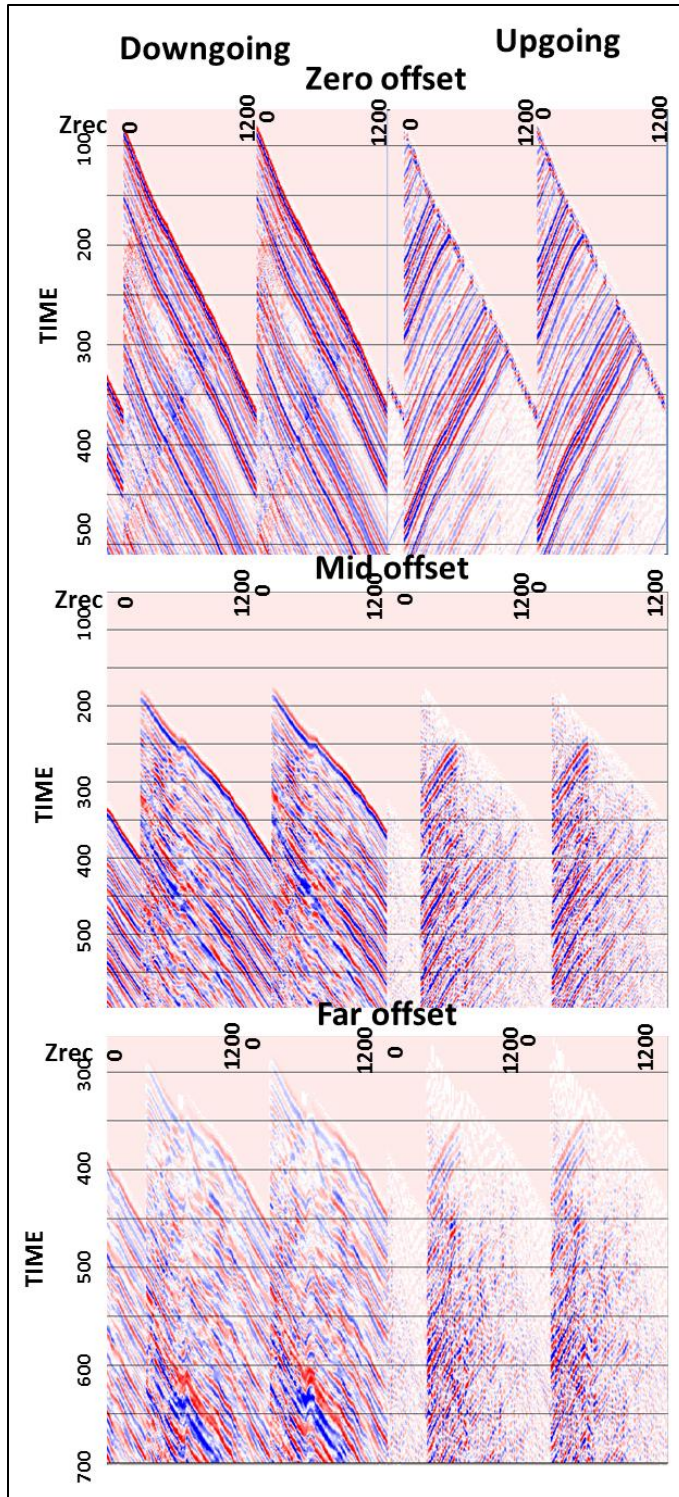


Figure 4.16: Three panels (zero, near, and far) for wavefield separated. The upgoing will be used as input in the migration.

The basic goal of TL processing is to enhance the time-lapse response as much as possible. In the early stage of steam-induced EOR, essentially the pore fluid changes with time, while the basic geological structure remains the same. In a mature EOR field, or in a zone of massive stress-related change (such as chalk reservoirs), we can see structural changes over time.

As the petrophysical changes in the model are too small, we tried multiple ways to generate migrated images to improve the time-lapse response by enhancing the TL signal in comparison to the background amplitudes. Figure 4.17 shows the baseline and monitor time-shifted and difference PP images for the walkaway VSP migrated. The upgoing wavefield was migrated with the Kirchhoff migration method (Yilmaz, 2001) without any deconvolution. We make the following observations in both the baseline and monitor images:

- 1) The overall structure and amplitudes content are similar in both dataset;
- 2) The amplitude decays symmetrically away from the well (center) due to the decrement of folding away from the well;
- 3) There are strong multiples visible around 1200 m because the data are migrated without deconvolution, but, as we are looking at the subtraction of the data, those multiples get canceled;
- 4) The TL response appears as negative amplitude over positive at 1050 m;
- 5) The signal to background ratio is about 13.1;
- 6) The multiples look a little off-center towards right from the anomaly, as discussed in Section 4.11.

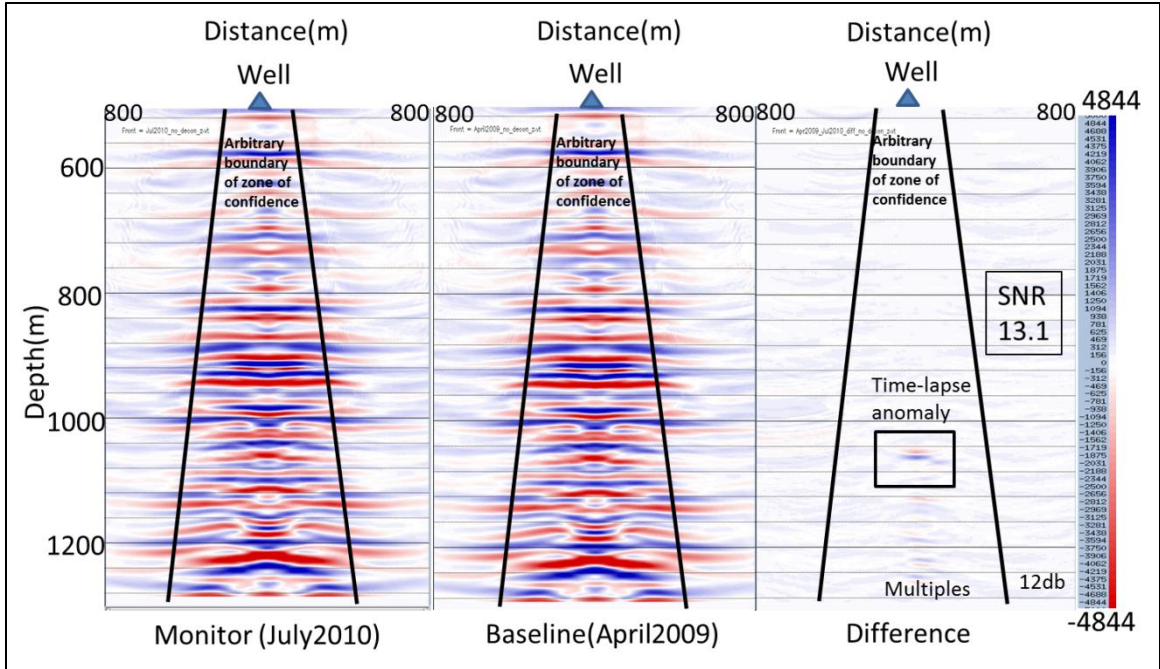


Figure 4.17: The right panel is the Kirchhoff migrated section for baseline; middle is for monitor after corrected for time-shifts. The black line shows the area of data fidelity; outside this line, the data is not very dependable. Taking a difference and plotting a 12 dB gained the left panel, showing the steam feature. Going to steam is indicated by decreased impedance (lower density, lower velocity), so it shows up as a trough followed by a peak. There are events below the steam, which are multiples as the input is not deconvolved.

We processed the upgoing by limiting the receivers, as shown in Figure 4.18. Receivers from top 220 m are not included in migration to avoid complex overburden. The result looks much cleaner and has less background noise, but, at the same time, the amplitude of the time-lapse anomalies gets dimmer. The signal to background ratio is about 11.1.

We then deconvolved the upgoing and migrated the dataset without the shallow receivers (Figure 4.19); we used both spiking deconvolution and interferometric deconvolution (Kiyashchenko and Mamari, 2010).

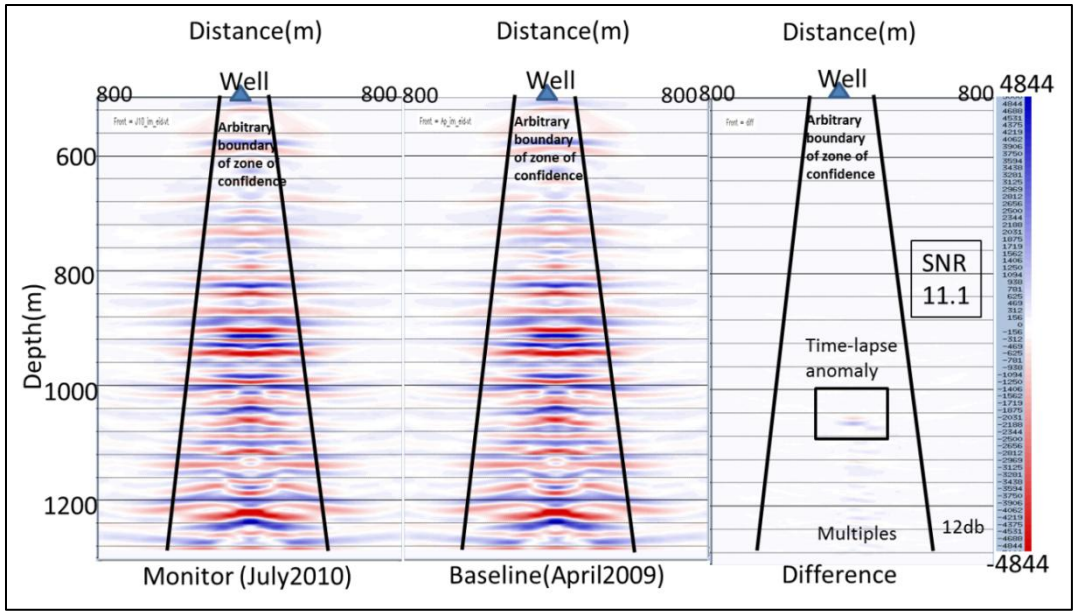


Figure 4.18: As the shallow receiver has no input in locating the steam, a subset of receivers were used in migration. Here, receivers shallower than 220 m were not used in migration. The images are better for both baseline and monitor; the difference image is also refined, though amplitude diminishes.

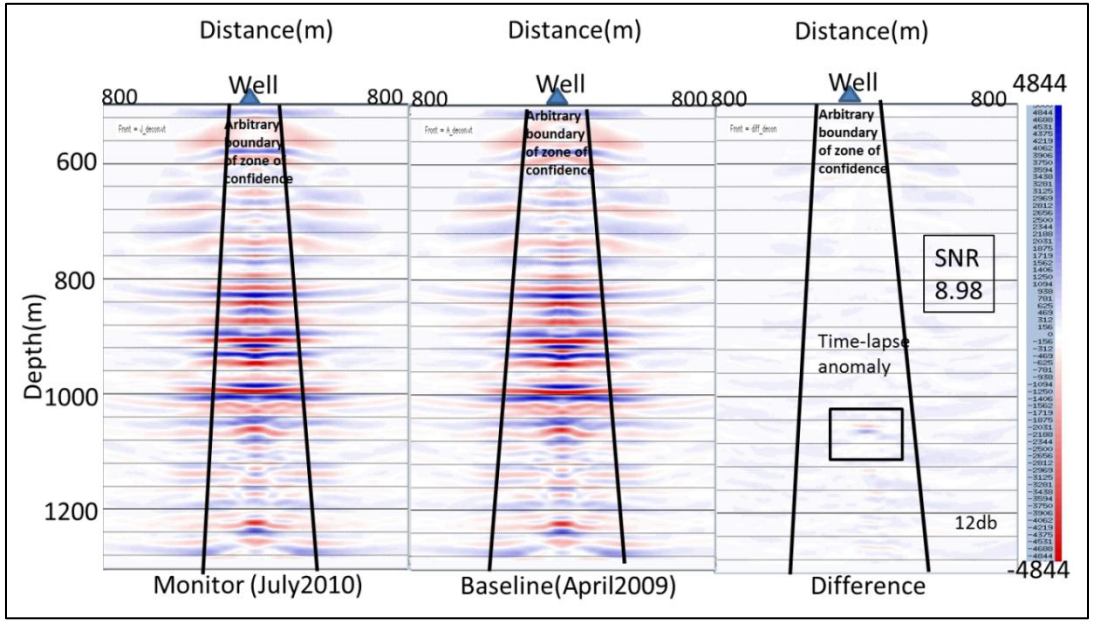


Figure 4.19: Deconvolved upgoing is used here as input in migration and we can see it improves the images. Events are continuous, flat, but as we know deconvolution introduce high frequency noise in the data , there are a lot of non-repeatable noise shows up in the difference image along with the steam.

We applied deterministic deconvolution to the upgoing wavefield using the deconvolution operator designed on the downgoing. Interferometric deconvolution was described by Kiyashchenko and Mamari; they adopted the OBC demultiple technique outlined in Traub *et al.* (2009). The idea is to deconvolve the data with downgoing multiples in the wave number domain. The expression may be written as:

$$U_{DEC}(k_x, \omega) = \frac{U_{UP}(k_x, \omega)}{U_{DN}(k_x, \omega)} U_{FB}(k_x, \omega)$$

where  $U_{up}(x_s, x_r, \omega)$ ,  $U_{dn}(x_s, x_r, \omega)$ , and  $U_0(x_s, x_r, \omega)$  are the space-frequency downgoing, upgoing, and gated first arrival wavefields generated by the source with lateral coordinate vector  $x_s$  and measured by the receiver  $x_r$ .

Figure 4.19 shows images of interferometric deconvolved baseline and time-shifted monitor and their differences. The multiples are suppressed in the baseline and monitor images; the structural continuity is better than in non-deconvolved images. The background noise, however, is much higher; the signal to background ratio is 8.98.

We then migrated the non-deconvolved data with lesser receivers (660 m -1200m) and used extra FK filtering to suppress shear; Figure 4.20 shows the data. We observe that as the background noise decreases, the overall amplitude diminishes and the lateral extent of the anomaly is also compromised.

Lastly, we attempted to gate the upgoing near first breaks to surgically mute the arrival of multiples, using the gated and shear suppressed upgoing for migration. The result is cleaner and free of multiples, but the 4D signal and lateral aperture are highly compromised (Figure 4.21).

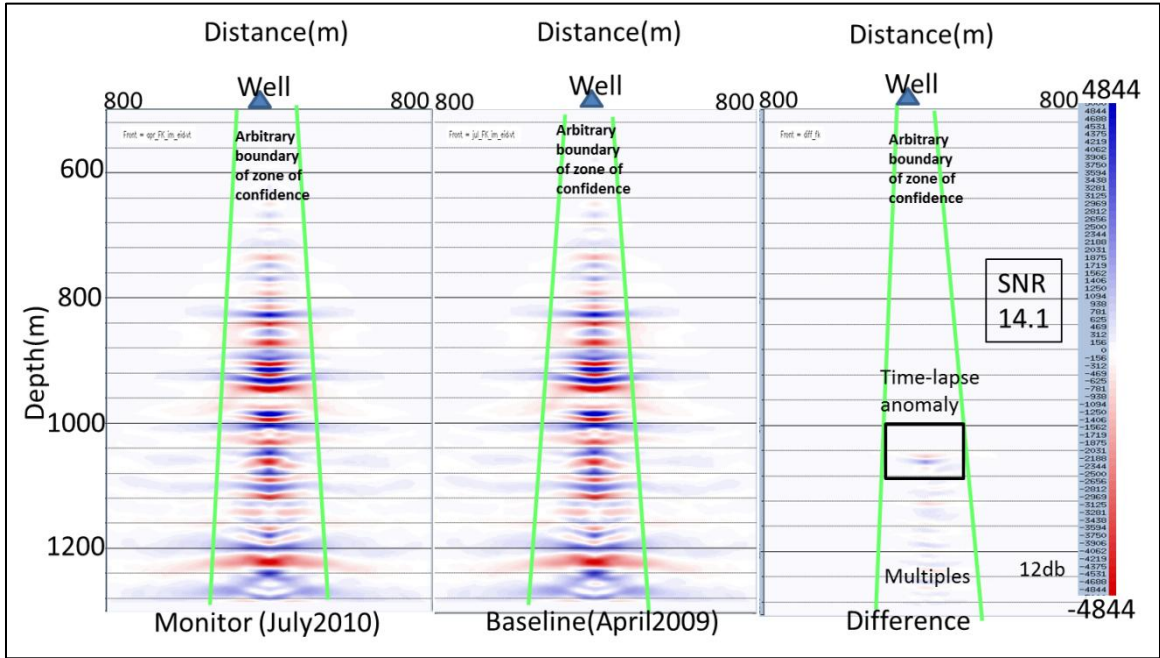


Figure 4.20: Similar plots with suppress shear. The lateral extent of the baseline and monitor is heavily compromised as top 550 m data is not used.

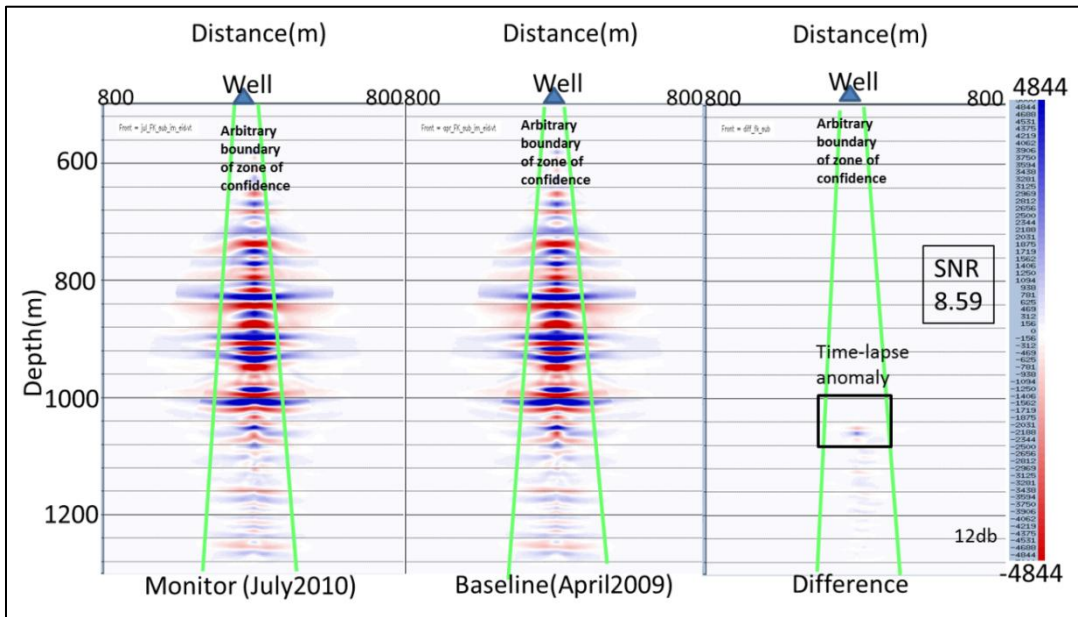


Figure 4.21: Input is only the first 150 ms of upgoing data. This is a crude way to surgically remove multiples; the image looks narrow in the bottom. In the difference map, the number of multiples is lower.

For visual comparison, we plotted all the difference maps together (Figure 4.22). Here we can clearly observe the following:

- 1) The less processing is done (such as deconvolution or shear suppressing) the better. Processing noises may increase background noise and diminish true anomalies;
- 2) Deconvolution worked better to image the wellbore surrounding, but as it incorporates higher frequency, it potentially increases background noise;
- 3) Experimenting with a subset of receivers should be used to have a vital impact on S/N, as well as the aperture of the anomalies;
- 4) Surgical muting heavily affects the S/N, so the aperture must be used with caution.

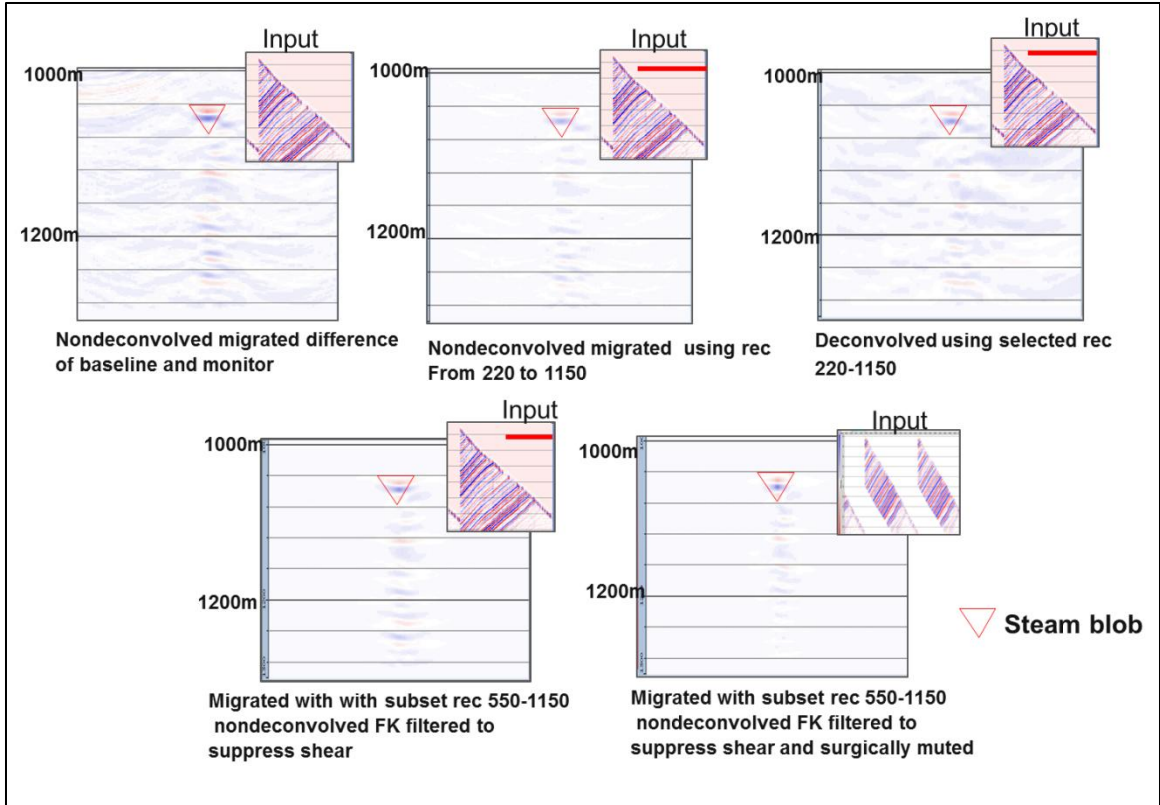


Figure 4.22: Difference map shown for comparison. The left smaller window shows the input data.

#### 4.9 TL attributes

Once difference maps were generated, as a measure of repeatability of the resulting images we calculated the RRR attribute (RMS of the difference normalized by average RMS of the baseline and monitor data). This attribute is equivalent to the NRMS attribute suggested by Kragh and Christie (2002) and discussed in Chapter 3. The attribute was calculated in three different running windows (60, 40 and 20 ms). Figures 4.23 to 4.25 show the RRR section for the difference walkaway VSP image. With a larger window (60 ms) length, the anomaly is easily identifiable in comparison to the

background, but as we decrease the window length, the shape of the anomaly gets much sharper.

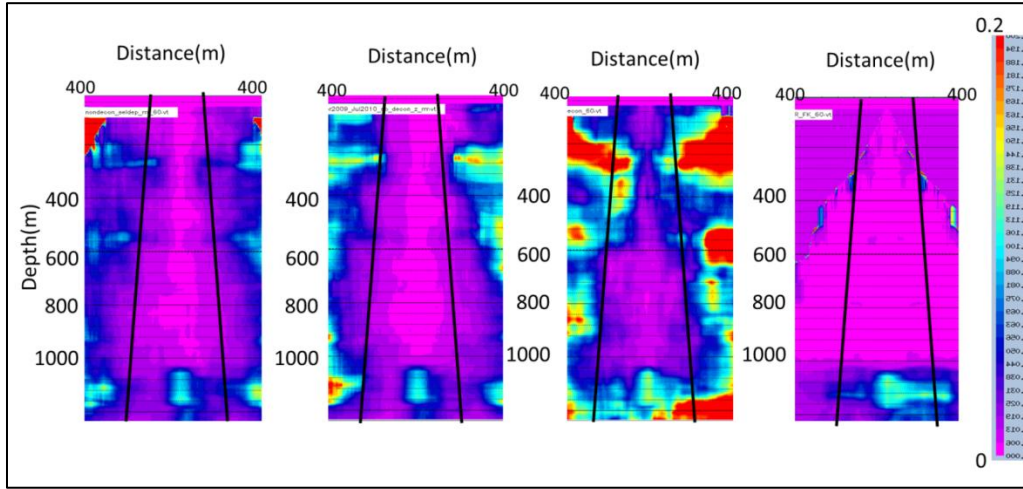


Figure 4.23: Panels showing RRR map of the differences for non-deconvolved, sub-set non-deconvolved, deconvolved, and shear-suppressed muted sections, respectively. The RRR was calculated in a 60 ms window length.

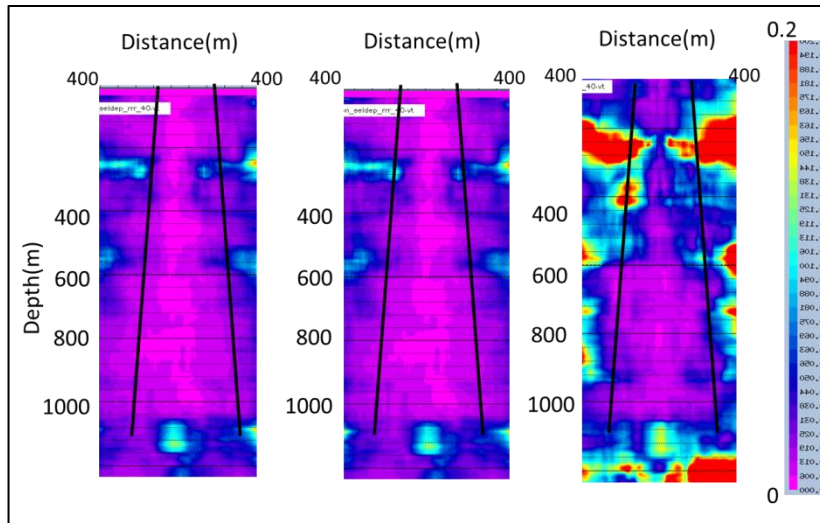


Figure 4.24: Panels showing RRR map of the differences for non-deconvolved, sub-set non-deconvolved, and deconvolved section, respectively. The RRR was calculated in a 40 ms window length.

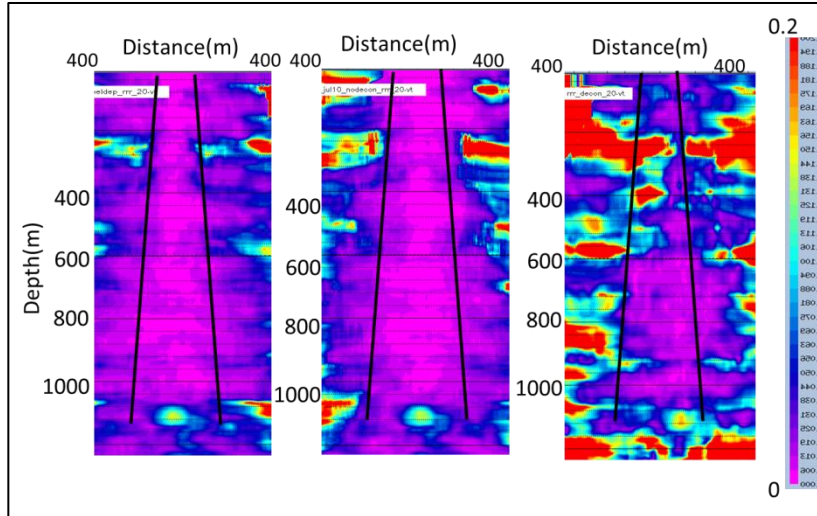


Figure 4.25: Panels showing RRR map of the differences for non-deconvolved, sub-set nondeconvolved, and deconvolved section, respectively. The RRR was calculated in a 20 ms window length.

#### 4.10 Modified VSP flow for TL processing

We processed the Z component to generate PP images for baseline and monitor and created a difference map to observe the TL anomaly. We modified the standard VSP processing flow because the main requirement in this context is to enhance the 4D signal. Figure 4.26 shows the processing flow for time lapse VSP processing; each color arrow shows one loop of image generation. Further difference maps are color-coded accordingly for result comparisons.

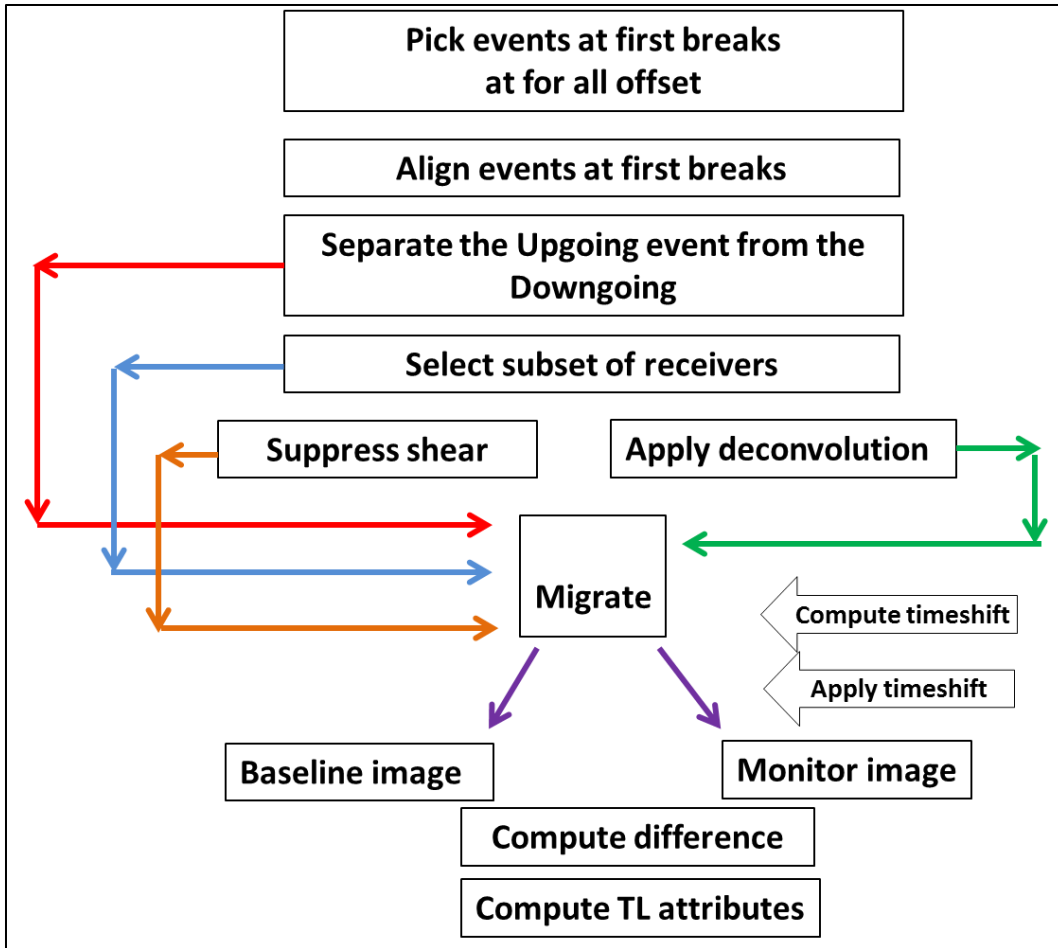


Figure 4.26: Flow chart summarizing TL VSP processing and amplitude enhancement analysis.

## 4.11 Ray tracing

In the difference images, we observe that the multiples and other events below the anomaly show a slight rightward shift from the wellbore. To further investigate this phenomenon, we performed ray tracing for various receiver locations (Figure 4.27). Close observation reveals that the steam feature in the velocity model is not symmetric: it is slightly shifted towards the right. The blue line below every ray trace map shows that

most of the illuminated area covers the right side of the steam blob. This explains why the events below the steam show a rightward shift from the center.

## **4.12 Results and interpretation**

We successfully imaged the TL anomalies owing to drops in velocity in the model. The RRR map shows the TL effect much more prominently, irrespective of the processing done; however, the shape and contamination with the zone of confidence differs with the amount of processing: for the VSP, it shows a cone around the wellbore. The RRR VSP profile (non-deconvolved) of the walkway line is compared with the RRR map at the reservoir level created internally by the operator (Kiyashchenko and Maamari, 2011), as shown in Figure 4.28. The location and character of the anomaly due to steam is very comparable between the two. The plotted north-south RRR profile map in the insets show very similar results to the synthetic VSP.

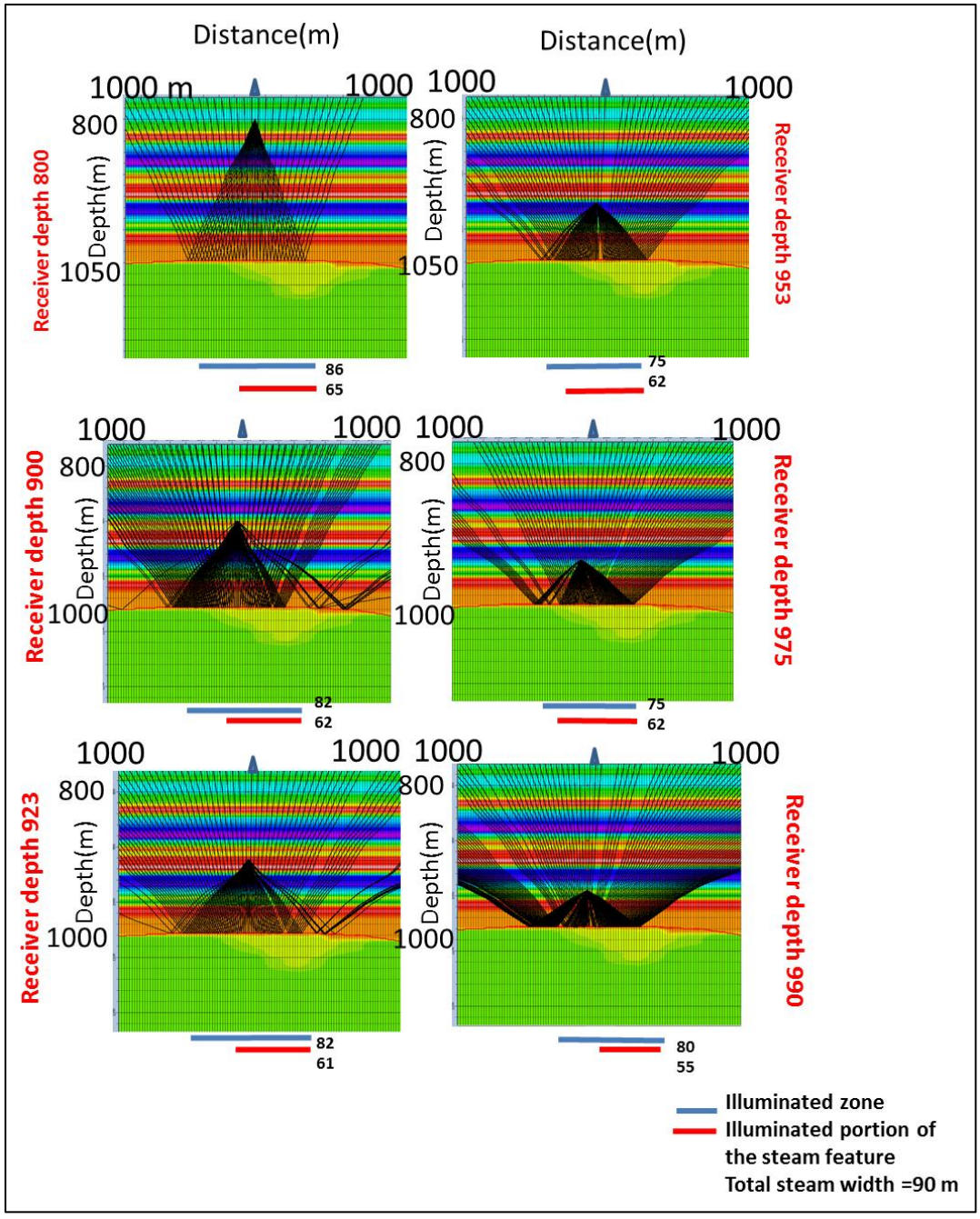


Figure 4.27: Series of ray tracing for different receiver levels show the zone of illumination. As there is a skew in the reservoir models that reflects in the velocity models too. That non-symmetric feature creates asymmetrical ray density. Due to this reason multiples below steam appears shifted towards right.

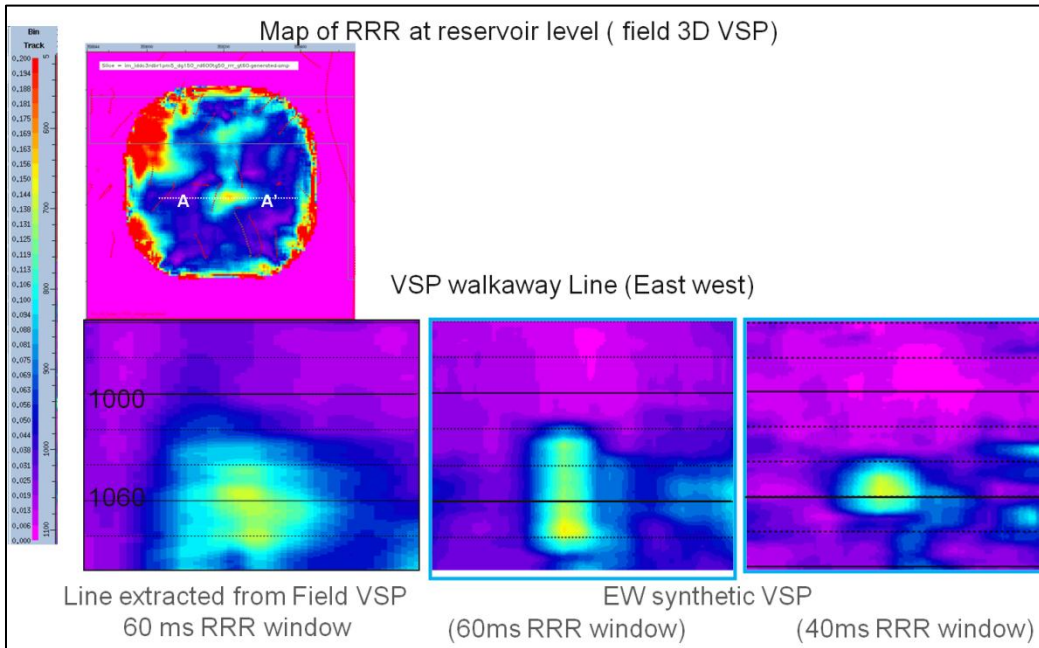


Figure 4.28: Comparison of field VSP (processed commercially) and synthetic VSP. Results are very similar, although the synthetic VSP underwent minimal processing.

## Chapter Five: PP and PS amplitude analysis

### 5.1 PP and PS in steam-flooded zones

The ultrasonic S-wave velocity is reported to decrease with increasing temperature and increase with pressure (Han 2006). Kato (2010) also mentioned that  $V_S$  drops as pore fluid pressure increases. In most measurements, the S-wave velocity is reported to be insensitive to change. We know that  $V_P / V_S$  drops in thermally treated reservoirs and because  $V_P$  decreases are significantly larger than changes in  $V_S$ , it is difficult to predict how  $V_S$  is changing.

No dipole sonic log was recorded after the steam injection in the Oman field. The pressure change due to steam injection is not great in Oman. The model-derived velocities probably show more density dropping effects after the steam injection.

The  $V_P/V_S$  always decreases in thermally treated reservoirs, although this does not necessarily say much about  $V_S$ . We know that even if  $V_P$  lowers, the  $V_P / V_S$  can drop, even if  $V_S$  stays insensitive, because the magnitude of  $V_P$  drop is much higher. In fact, a slight increase in  $V_S$  also produces a decrease in  $V_P/V_S$ . Consequently, looking at only  $V_P/V_S$  will not be sufficient for steam monitoring purposes. The PS reflection does not only depend on the velocities; density also plays a major role. With more steam in the reservoir, the density decreases. In this chapter, we investigate how PP and PS reflection change with greater steam saturation (and amounts) in the reservoir. There is not much scope to change  $V_S$  velocity, but changing density and steam saturation play vital roles in modifying the existing PS reflection along with PP.

## 5.2 PS reflections in walkway synthetic VSP

After successful imaging of the TL anomaly, we next examined the PS reflection. The horizontal component of the field VSP was not processed by the operator. The horizontal components for the baseline (April 2009) field data was available. A quick look shows there are elastic events visible (Figure 5.1), but no field monitor horizontal components were readily available to observe measurable changes. As the synthetic was very comparable to the field (as seen in Figure 4.2) and noise free, we decided to first analyze PS in the synthetic, and, upon success, then investigate field data. In Figure 5.2, a) is a reminder of how PP and PS reflections are generated at a reflector; b) shows events in a VSP section. Figure 5.3 shows how it should look when we try to see a PS reflection in a TL VSP section. This series of images are helpful to identify events such as PP and PS. It is easy to identify different events in shot gather because they appear in different time and slope. The slope is defined by the velocity of the type of waves (P or S). In a shot gather section, slower events appear steeper as they take more time to travel the same distance. Normally, amplitude analysis is done in a receiver gather, but it is very difficult to distinguish and differentiate wavefields in this way. It takes several steps to separate events before VSP data can be plotted in a receiver gather for amplitude analysis (as discussed below).

For the synthetic VSP of the Oman EOR field, we extracted amplitudes to observe the difference between monitor and baseline. We note an observable difference in the PP amplitude, but almost no difference in PS amplitude. Figure 5.4 is a plot of amplitude

difference between monitor and baseline for PP reflections plotted for receiver 900; for PS reflections, all data points cluster near zero.

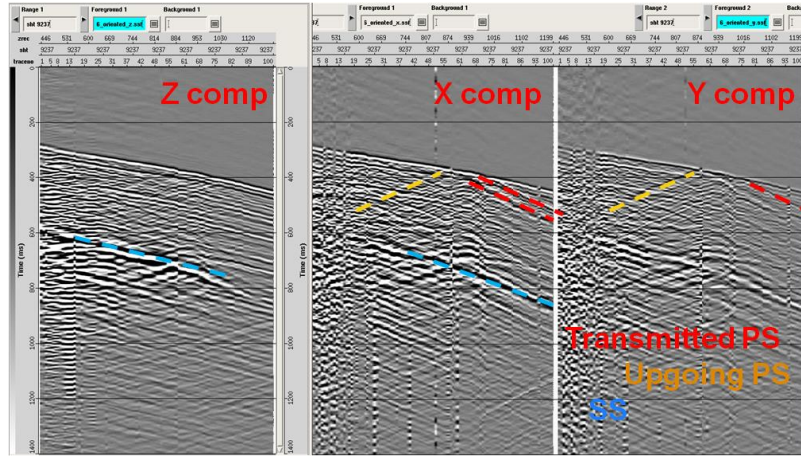


Figure 5.1: Horizontal components from baseline field VSP (April 2009) showing no upgoing PS reflections.

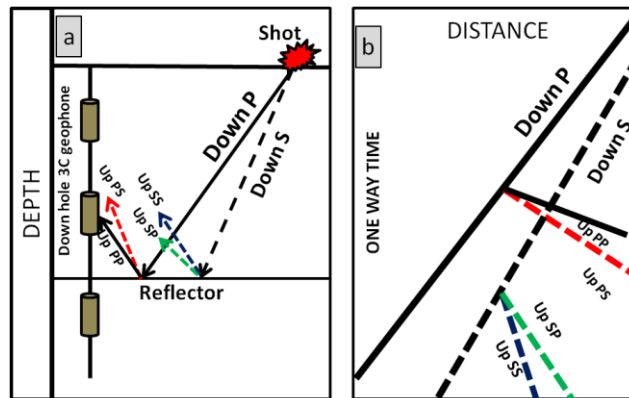


Figure 5.2: Schematic diagrams: a) how P- and S-waves travel from source and generate different events as it hits a reflector and get recorded in a 3C down hole geophone.; b) annotated schematic diagram with different seismic events in VSP.

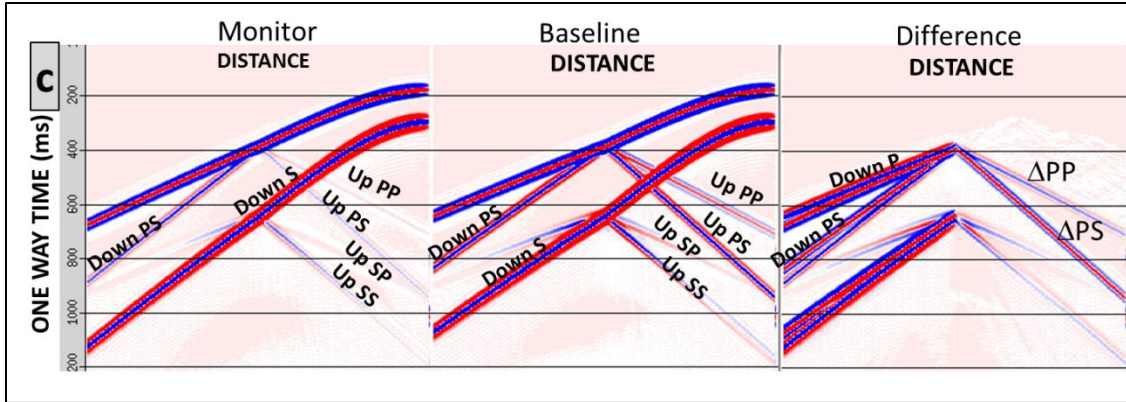


Figure 5.3: Annotated VSP events for baseline, monitor, and their 4D difference.

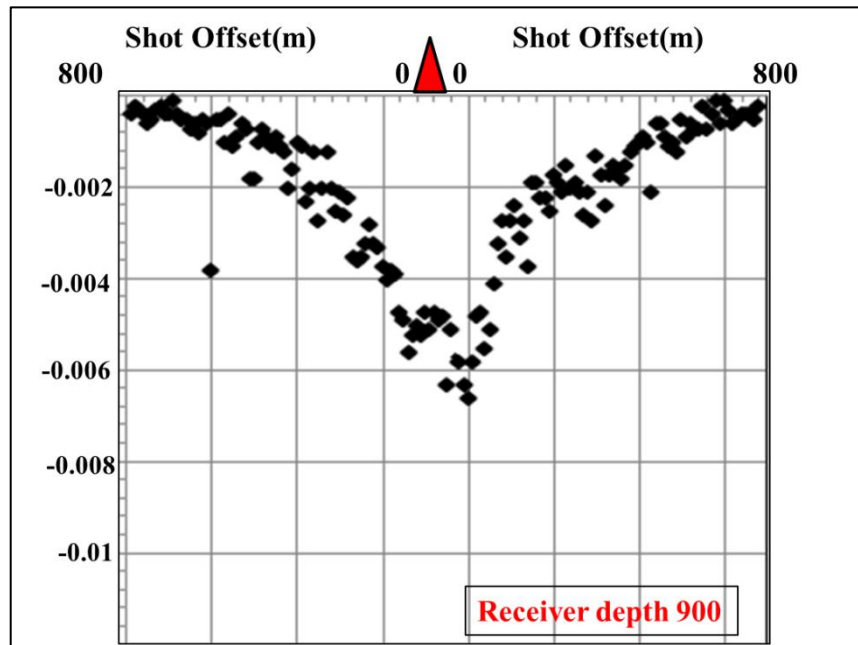


Figure 5.4: Difference of PP amplitude (monitor-baseline) for walkaway synthetic VSP. The amplitude difference between the two datasets is maximum at zero-offset and it decreases at larger offsets.

### 5.3 Theoretical reflectivity analysis (PP and PS)

To verify the authenticity of amplitude behavior, we used the CREWES reflectivity explorer Applet from the University of Calgary. We used an average velocity

and density for the perforation zone from the well for a baseline. Figure 5.5 shows the reflectivity behavior for PP and PS as  $R_{PP}$  and  $R_{PS}$ . The underlying equations may be expressed as:

$$R^{PP}(\theta) \sim \frac{1}{2} \left( 1 - 4 \sin^2 \theta \right) \frac{\Delta \rho}{\rho} + \frac{1}{2 \cos^2 \theta} \frac{\Delta \alpha}{\alpha} - \frac{4 \beta^2}{\alpha^2} \sin^2 \theta \frac{\Delta \beta}{\beta} \quad (5.1)$$

and

$$R^{PS}(\theta) \sim - \frac{\alpha \tan \phi}{2 \beta} \left( \begin{array}{l} \left( 1 - 2 \frac{\beta^2}{\alpha^2} \sin^2 \theta + 2 \frac{\beta}{\alpha} \cos \theta \cos \phi \right) \frac{\Delta \rho}{\rho} - \\ \left( 4 \frac{\beta^2}{\alpha^2} \sin^2 \theta + \frac{4 \beta}{\alpha} \cos \theta \cos \phi \right) \frac{\Delta \beta}{\beta} \end{array} \right) \quad (5.2),$$

where  $\alpha$ ,  $\beta$ , and  $\rho$  are P- and S-wave and density,  $\theta$  is the average of the P-wave angle of incidence on and transmission through the interface,  $\phi$  is the average of the SV-wave angle of reflection and its associated transmission,  $\Delta \alpha$ ,  $\Delta \beta$ , and  $\Delta \rho$  are the P-wave and S-wave velocity changes, and density changes across the interface (Aki and Richards, 1980).

This applet calculates reflectivity for surface seismic geometry, which is somewhat different than VSP geometry. Nonetheless, it gives a basic idea about amplitude behavior when plotted as angle of incidence. In a repeat acoustic log, we observe a slight increase in S-wave velocity and drop in P-wave velocity. We increased the  $V_S$  by 2 percent, dropped  $V_P$  by 5 percent, dropped density by 2 percent, and recalculated the reflectivity for PP and PS (Figure 5.5). Comparing the plots, it is clear that PP amplitude decreases, but PS stays almost unchanged. The Haradh top is already a weak reflector; the changes in petrophysical parameters (P- and S-wave velocity and density) that occurred due to steam injection are too low to create any measurable PS

reflection change. Though the changes in PS reflection are not strong enough yet in our Oman field, we reiterate that we are looking at changes due to steam injection in only a one-year window. As more steam is injected in the reservoir in the future, and with more production of oil, the petrophysical numbers will change significantly. Therefore, we widened the scope of calculations to estimate how much change in petrophysical properties would be needed to observe some measurable amount of PS change in the future. We performed a series of theoretical reflectivity analyses to determine how PS reflection changes with changing velocities and densities before calculating the minimum change needed to see optimum PS reflections. Finally, we created a series of two-layer elastic synthetic models to verify the theoretical PP and PS reflectivity as a function of changing velocities and density ( $\alpha$ ,  $\beta$ ,  $\rho$ ).

Based on well logs from the present study and literature surveys, we varied  $\Delta\alpha$ ,  $\Delta\beta$ ,  $\Delta\rho$  in step-wise units (given in Table 5.1) and created ten different scenarios. The units of  $\Delta$  are 5 percent for  $\alpha$  and 2 percent for  $\beta$  and  $\rho$ . In the models,  $\alpha$  and  $\rho$  always decrease, while change in  $\beta$  varies from -2 percent to 2 percent. We observe in the series of theoretical curves how PP (thick line) and PS (thin line) change as we change the  $\alpha$ ,  $\beta$ , and  $\rho$ . Until model M7, the PP response drops significantly, but the change in PS for low angles (below 30 degrees) is significantly small. In real seismic data, that small of a change would be buried below the noise. Only after a density drop of 8 percent or more do PS curves change significantly. It is clear that the density change overshadows S-wave velocity effects. We generated several synthetic VSPs and plotted their PP and PS amplitudes as a function of shot-offset to see how much they agree with the theoretical

curves, which are designed for surface seismic data. The results are quite similar and discussed and shown later in the chapter.

Table 5.1: Two-layer modeling parameters.

<b>Model</b>	$\Delta\alpha$	$\Delta\beta$	$\Delta\rho$	<b>Comment</b>
<b>Base model</b>	NA	NA	NA	Oman prototype
<b>Model 1 (M1)</b>	-5%	-2%	-2%	From well log after one year. PP reflection drops but PS change is very minor.
<b>Model 2 (M2)</b>	-10%	0%	-2%	PP reflectivity change for larger angles. In VSP geometry reflectivity changes will not be much different than M1
<b>Model 3 (M3)</b>	-10%	2%	-2%	PP reflectivity change for larger angles. In VSP geometry reflectivity changes will not be much different than M1
<b>Model 4 (M4)</b>	-10%	-2%	-2%	Drop in $\Delta\beta$ along with density lowers the PS reflectivity.
<b>Model 5 (M5)</b>	-10%	0%	-4%	Density drop started affecting both PP and PS
<b>Model 6 (M6)</b>	-10%	2%	-4%	Density drop started affecting both PP and PS
<b>Model 7 (M7)</b>	-10%	-2%	-4%	Drop in $\Delta\beta$ along with density lowers the PS reflectivity than usual. This type of effect theoretically can be visible in a high pore fluid zone
<b>Model 8 (M8)</b>	-10%	0%	-8%	density drops dominates,
<b>Model 9 (M9)</b>	-10%	2%	-8%	density drops dominates,
<b>Model 10 (M10)</b>	-10%	-2%	-8%	PS reflection changes polarity

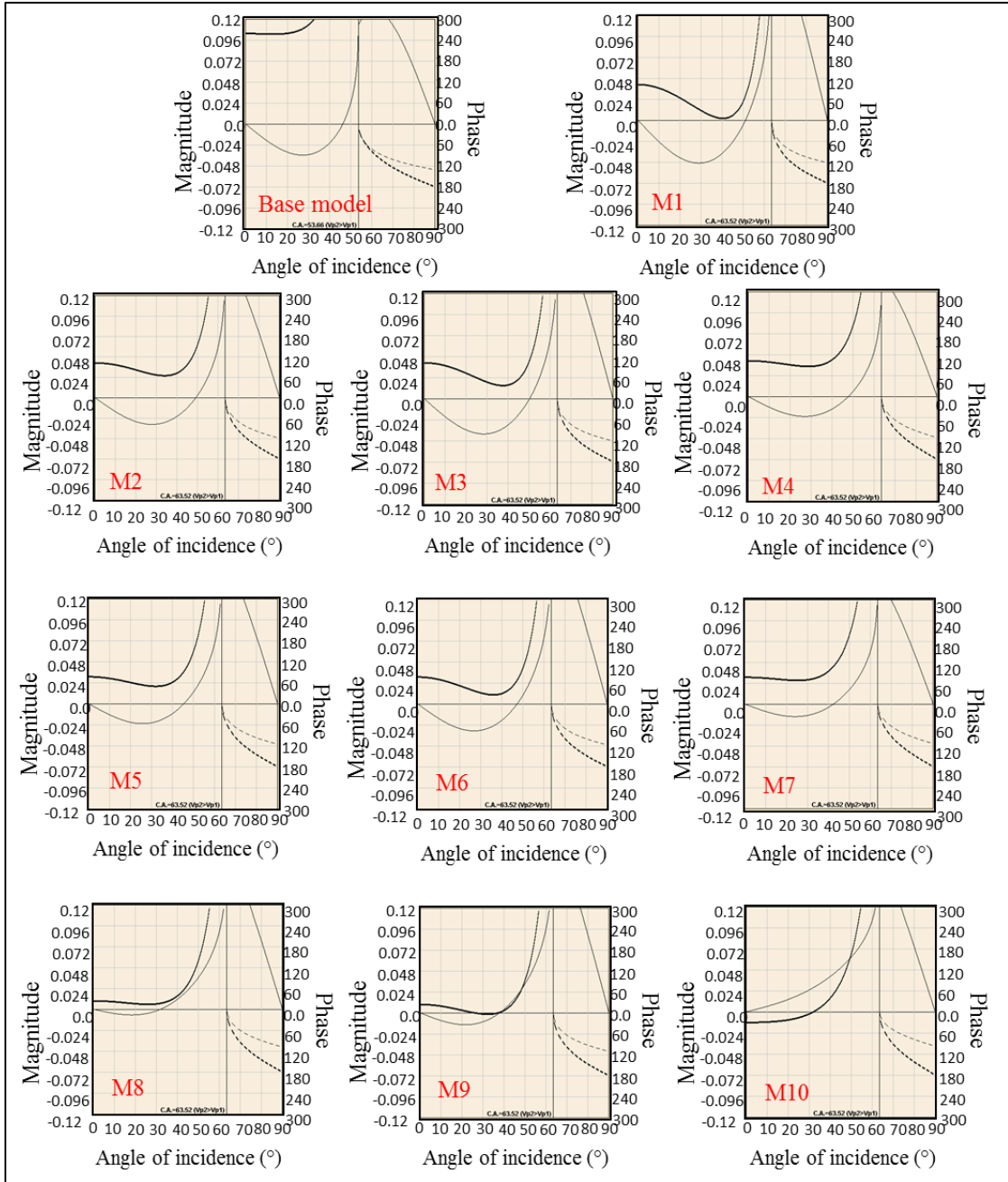


Figure 5.5: Theoretical simulation using CREWES Explorer applet showing how PP and PS reflectivity changes with different combinations of changed  $\alpha$ ,  $\beta$ , and  $\rho$ .

## 5.4 Factors that control PS reflections

As steam gets into the reservoir, it changes its compressibility, dropping the P-wave velocity; normally, the  $V_P$  decrease is significant. PS increases due to density change, but changes in  $V_S$  are not as dramatic as  $V_P$ . Most researchers have reported that any  $V_S$  change is very small; in a few cases, it is unchanged.  $V_S$  can also decrease as pore fluid pressure increases. In fact, two things happen simultaneously: as steam gets into the reservoir, it both increases the pore fluid pressure and decreases the density. These two events have opposite effects on  $V_S$ . That may be why  $V_S$  is often measured as insensitive in thermally treated reservoirs. But unless there is a significant drop in density (in this case 8 percent or more), it is unlikely to find a measurable PS reflectivity difference between baseline and monitor. The density decrease is directly associated with the steam saturation within the reservoir. The higher the steam saturation gets, the lower the density becomes, making the PS difference brighter.

## 5.5 Two-layer elastic modeling for theoretical validation

We generated a series of 3C walkaway VSP by using WFD modeling elastic wave equations to validate the theoretical PP and PS reflectivity as a function of offset. This iterative modeling is the first step to developing a detailed workflow for a PS feasibility test for TL seismic. We began with simple two-layer, laterally-constant density and velocity models. Later, we compared the results with theoretical reflectivity. Upon success, we modeled PP and PS reflections for steam chambers of variable thicknesses, with variable steam saturation.

In the following section, we discuss how the modeling was achieved and optimized, followed by a TL, PP, and PS event identification discussion. We also discuss the amplitude extraction and describe the amplitude versus shot offset curves for various models.

### 5.5.1 Modeling parameters

We generated two constant layer velocity and density models using Shell's in-house software (ndi). The upper layer was modeled with P- and S-velocity and density of the seal above the Haradh portion of the reservoir; it remained constant throughout. We changed the lower layer P- and S-wave velocities and densities according to Table 5.1. We used those model velocities and densities in both WFD and generated VSP. All other components remained as described in Chapter 4 (Section 4.3), except the elastic wave equation was used in this application. Acquisition parameters are given in Table 5.2. Figure 5.6 shows snapshots of density and velocity models used in the modeling.

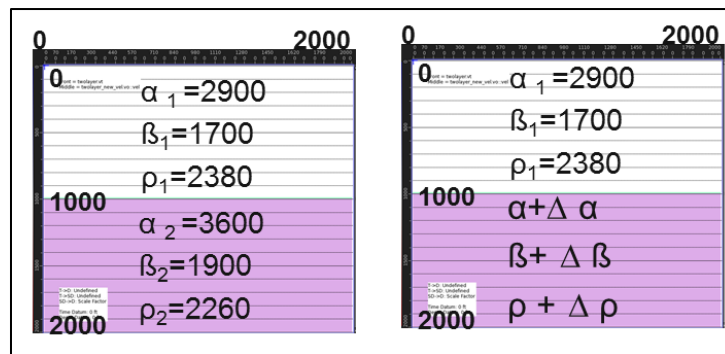


Figure 5.6: Two-layer velocity and density models used in WFD. The top layer remained unchanged, while in the bottom layers, velocity and density were modified to simulate different mode monitor situations.

We iteratively created several models to discover the best combination of modeling parameters to create artifact-free models. Figure 5.7 indicates how increasing extra points, or a thicker absorbing boundary, helps to generate cleaner models; however, at the same time it increases computation time.

Table 5.2: VSP acquisition parameters for PS modeling.

Wellbore	Vertical well
Source type	Vertical force
Receiver interval	10 m
Number of receiver	200
Total shot	199 (99 shots in each side and one on the top of the well)
Shot interval	10 m

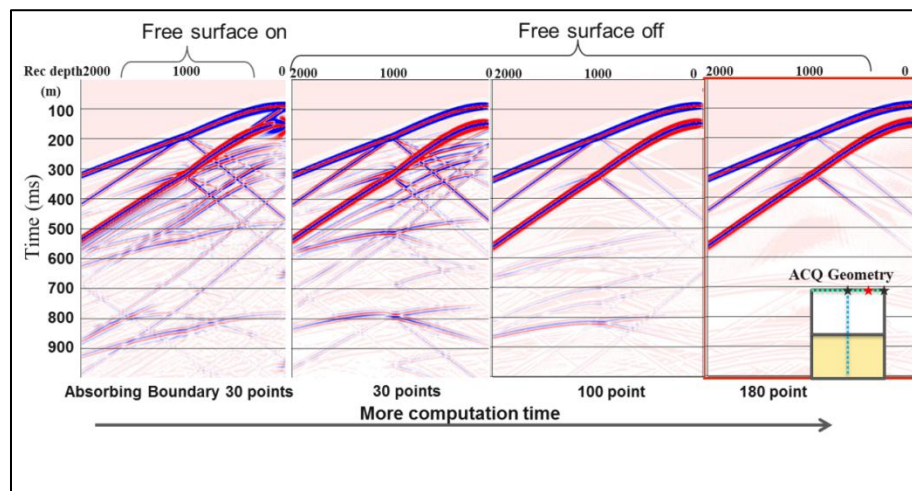


Figure 5.7: VSP modeling optimization to generate clear reflections.

### 5.5.2 Data description and event identification

Figure 5.8 displays a plot of the X and the Z components of the walkaway synthetic VSP for the Oman prototype baseline model. Here, the PP and PS events are fairly distinct. Figure 5.9 shows similarly plotted results for model 10 (M10). Figure 5.10 shows the difference between the X component of M10 and the baseline. In this case, we note that the PS amplitude gets much stronger as we subtract data of different polarity so they add up. As we know, the total energy for PS amplitude is given as:

$$\text{Energy (A)} = A_x \cos\alpha + A_z \sin\alpha$$

This equation explains why we see small PS reflections in Z component and vice-versa.

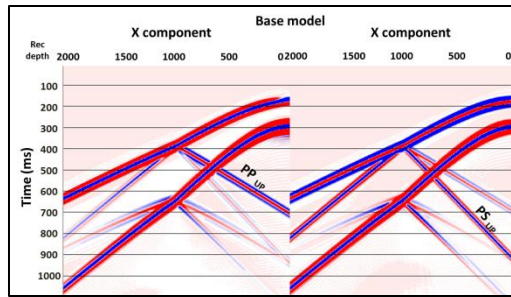


Figure 5.8: Horizontal and vertical components of two-layer baseline VSP.

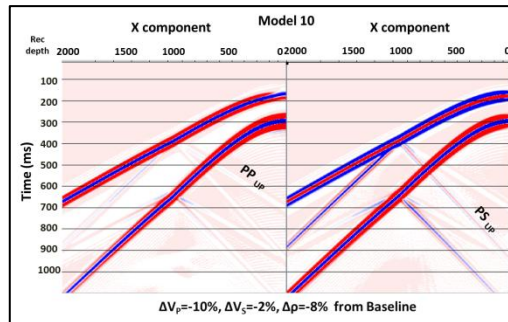


Figure 5.9: Horizontal and vertical components of model 8 VSP.

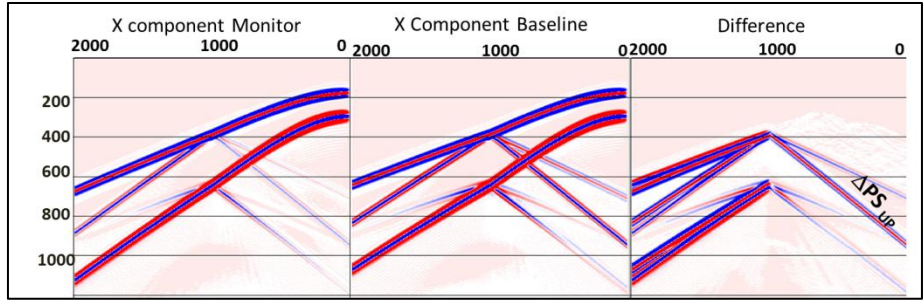


Figure 5.10: Horizontal components of baseline and M8 and the difference.

### 5.5.3 Data preparation to extract amplitudes

For VSP geometry, if we plot all shots with respect to a receiver depth (receiver gathers), it gives us the angles for the particular depth. For PS reflection, because a particular receiver gives a limited coverage of angles, it is important to look at various receiver gathers for amplitude analysis in VSP. The relation between shots and angles for PS is given by the following, as illustrated in Figure 5.11:

$$X_s/y = \tan \phi \text{ and}$$

$$X_p/Z = \tan \theta, \text{ where}$$

$$V_p/V_s = \sin\theta/\sin\phi \text{ and } X = X_p + X_s \quad (5.3).$$

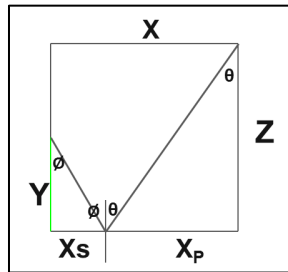


Figure 5.11: Diagram showing relationship between angles for PS reflection for a fix receiver.

In order to extract the PP or PS reflection, it is very important to separate them from the total wavefield. This process differs from up-down wavefield separation. After the upgoing and downgoing wavefields are separated using median filter or FK, the upgoing portion of data contains the reflected PP and PS events, along with many upgoing events. One must try to keep the real amplitude as little affected as possible, otherwise Amplitude vs. Offset (AVO) plots are compromised. Figure 5.12 shows FK plots demonstrating how upgoing events (both PP and PS) are separated from the total wavefield. We then took the upgoing events and selected the PS reflections as first break picking in normal VSP processing. We then used these PS events to flatten the data at PS. We used a dip-median filter, along with a gated window along, that flattened PS to filter out the PP and any other events that came later in time. We used an 11-point dip median filter. Panels of Figure 5.13 show dip-median filtering; Figure 5.14 shows extracted PS unflatten. We observe that the dip-median filter works better in deeper sections as the slope separation of PP and PS is greater.

This extensive process is needed for most of the receivers, especially those close to the reflector, because reflections for PP and PS are too close. As they move away from each other, they appear well separated. Figure 5.15 is an animated illustration of the process of PS amplitude extraction steps. The PS amplitudes are extracted, gained for spherical divergence and the total energy is calculated for baseline and different models. The plot in the following section shows how these extracted amplitudes are related with theoretical AVA (Amplitude vs Angles) plots.

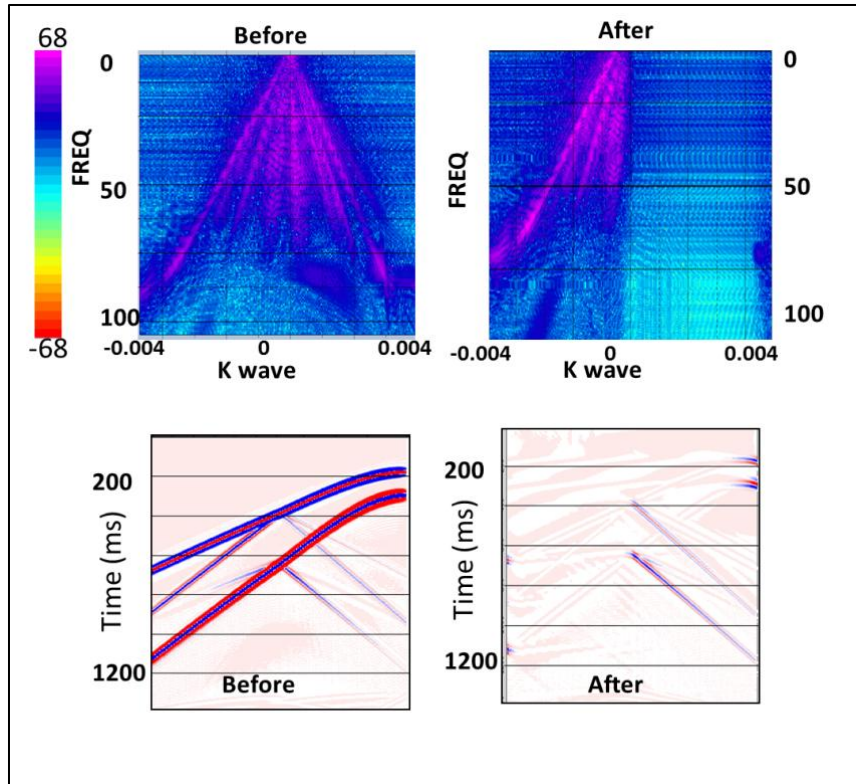


Figure 5.12: FK plots showing how upgoing events (both PP and PS) are separated from the total wavefield.

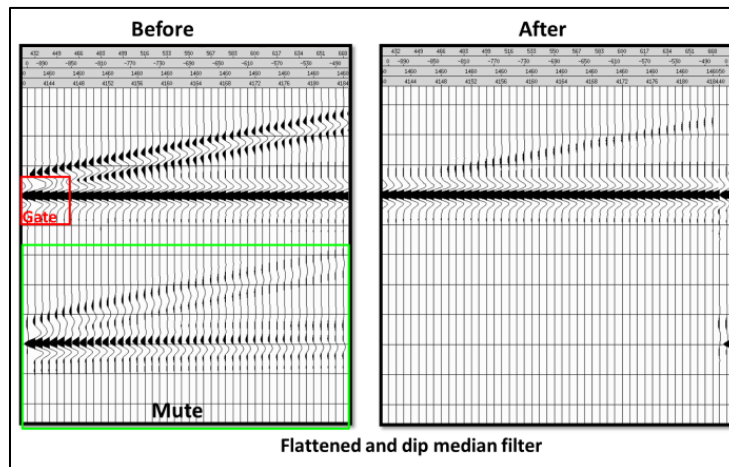


Figure 5.13: Dip median filtering and gating along PS event.

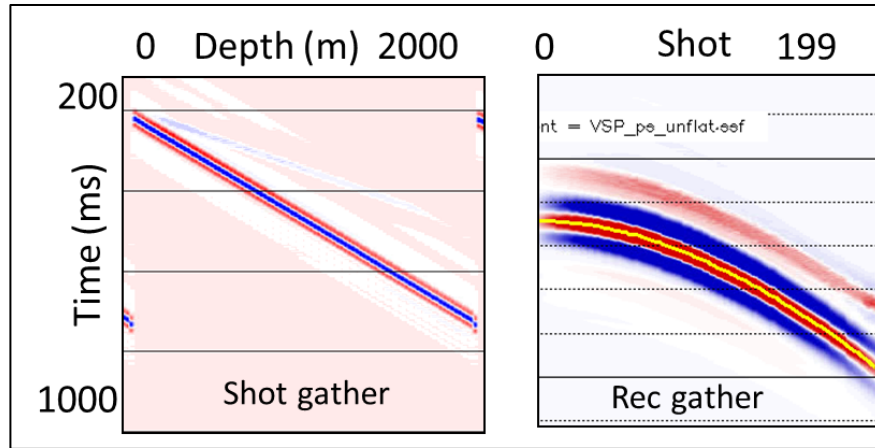


Figure 5.14: Extracted PS unflattened; amplitudes are extracted along the yellow event in the receiver gather panel.

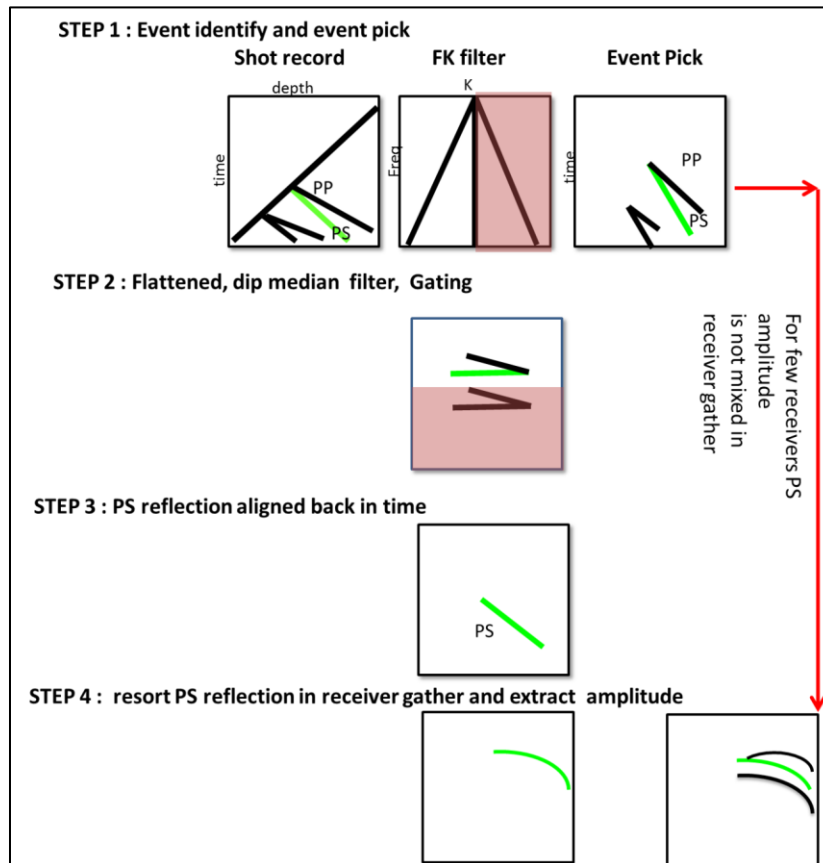


Figure 5.15: Schematic stepwise illustration of data preparation to extract PS amplitude in a receiver gathers.

### 5.5.4 Theoretical Validation

Figure 5.16 shows a plot of PS amplitudes as a function of offset for 4 models. We can see they are very similar. Though the slopes are not exactly replicating, as previously discussed, this is a plot of amplitudes as a function of shot offset; and theoretical curves are designed for surface seismic. Overall, it matches well.

From these plots, we note that the PS reflection is stronger when density change is significantly higher. Otherwise, only P- and S-wave changes are incapable of producing measurable PS difference that can be used further in joint inversion.

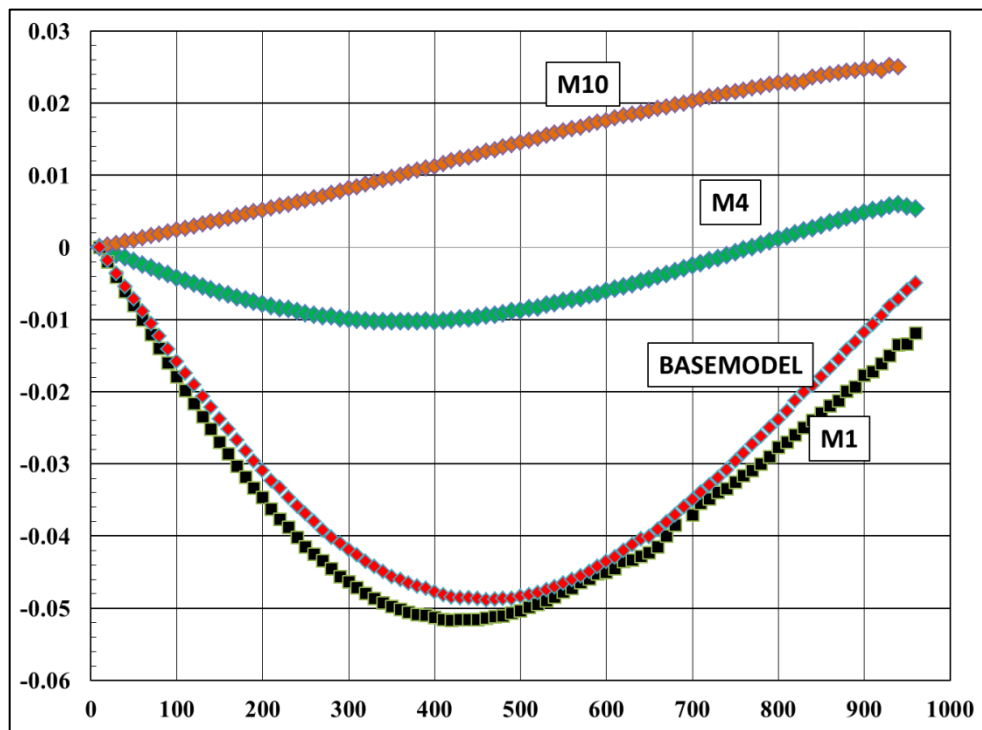


Figure 5.16: plot of PS amplitudes as a function of offset for 4 models. The PS amplitude behavior is very similar to the theoretical curves shown in Figure 5.5.

## 5.6 Three-layer steam modeling with variable steam thickness

After successful modeling of PS response for the simple two-layer case, we introduce a third layer in modeling to simulate a steam layer within reservoir. In this step, the seal and the initial reservoir property stay the same, while both petrophysical property of the steam layer and thickness of the steam layer change.

We used Gassmann substitution to calculate the changed  $V_P$ ,  $V_S$ , and density for the steam-saturated layer. We used constant steam saturation (30 percent) for recalculation. In this section, we only consider the effect of changing thickness on PS reflectivity. We modeled the minimum thickness of the steam needed to get a clear reflection from the top of the steam layer. It is very important to get a reflection from the top of the steam for amplitude analysis for AVO. If the steam layer is not thick enough, the whole steam layer will act as a single reflector and amplitude will be contaminated. This thickness of the steam layer is a function of the initial impedance contrast to the boundary and wavelength.

We generated VSPs for three different steam layer thicknesses; Figure 5.17 displays the different steam layers. We modified density velocity models, used as inputs to WFD, accordingly. Table 5.3 shows the fluid parameters from the wells that are used in the Gassmann substitution. Figure 5.18 shows that, in the case of a steam layer of 150 m, the top and base reflections are clearly separated. In the case of 100 m, it is still separated, but for a 50 m steam layer thickness, top and base reflections coincide. The wavelength is 130 m, so it needs to have at least 1/3 of a wavelength to get clean amplitude from the top of the steam layer.

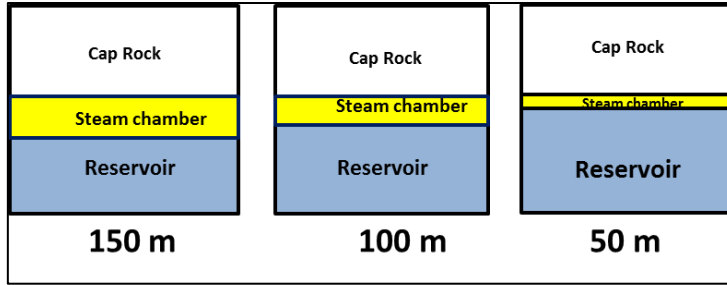


Figure 5.17: Schematic diagram shows variable steam thickness.

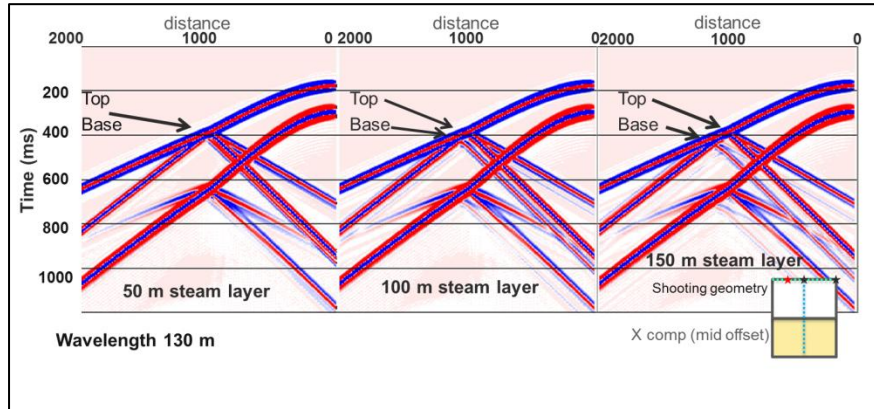


Figure 5.18: X component VSP with various steam thicknesses. In the case of steam of 150 m, the top and base reflections are clearly separated; in the case of 100 m, it is still separated, but for 50 m steam, top and base reflections coincide.

Table 5.3: Fluid properties of inputs used for the Gassmann substitution.

Porosities	0.23
Density of the oil	783 kg/m <sup>3</sup>
Oil velocity	750 m/s
Steam density	26 kg/m <sup>3</sup>
Steam velocity	498 m/s

## 5.7 Three-layer steam modeling with variable steam saturation and steam width

Once the steam layer thickness was calculated, we determined the effect of various steam saturations in PS reflection. We used Shell's internal Gassmann calculator "Promise" to calculate changed velocities and densities for various steam saturations. In this case, steam saturation is actually the proportion of steam in pore space by volume. For example, 30 percent steam saturation means that 30 percent of the pore volume is steam and 70 percent is another fluid. This term does not reflect steam quality.

In Gassmann's substitution, the  $V_P$  drops and  $V_S$  increases when we used a steam saturation below 0.1 (10 percent of the pore volume of pure); both  $V_P$  and  $V_S$  increased afterwards. Initially, this might seem unusual: as steam makes the rock more compressible,  $K$  will drop and that will make  $V_P$  drop. A question emerged regarding what was causing the increase in  $V_P$  with increased steam saturation.

Looking at the expression for  $V_P = \sqrt{((K_b + 4/3 * \mu_b) / \rho_b)}$ , it is a function of both  $K_b$  and  $\rho_b$ . If  $\rho_b$  was a constant, one would expect the  $V_P$  to decrease as  $K_b$  decreases. If  $K_b$  was a constant, a decrease in  $\rho_b$  would result in an increase in  $V_P$ . But both  $K_b$  and  $\rho_b$  are decreasing as steam saturation increases, meaning one needs to consider the combined effect. At low steam saturations, the reduction of  $K_b$  is greater than  $\rho_b$  so the velocity decreases; however, at higher steam saturations, the decrease in  $K_b$  'flattens out'

and the decrease in  $\rho_b$  overtake it, resulting in a  $V_p$  increase. Plotting the  $K_{new}$  and new rock properties  $Rho$  versus steam saturation shows this effect.

Lastly, we generated two more synthetic VSP with laterally variable widths from 100 m and a 50 m from the well (Figure 5.19). We extracted the PP and PS amplitudes for 50 m thick steam and calculated the total energy for various receiver gathers for amplitude analyses discussed in the next section.

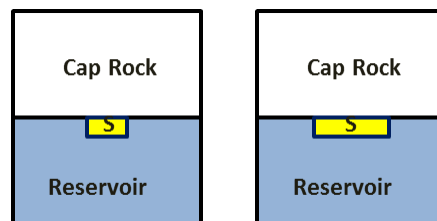


Figure 5.19: Schematic diagram showing variable steam width.

## 5.8 Amplitude as a function of shot offset

We extracted the PP and PS amplitudes for the 30 percent steam-saturated three-layered model with a 50 m wide steam chamber. We also extracted the amplitude for the very base two-layer models, which have the petrophysical parameters of the seal and initial reservoir. We plotted the amplitudes as a function of shot offset. As our model was bilaterally symmetrical, we plotted one-half on the well for each model to see how amplitude behaves as a function of shot offset and changed fluid in the host rock. Figures 5.20 to 5.23 show amplitude plots for four different receiver gathers from 600 to 900 m. Each plot consists of 4 curves, two (PP and PS) for each baseline and monitor. A few common observations from the experiments are as follows:

- 1) The magnitude of amplitudes for monitor PP decreases;
- 2) PP difference between baseline and monitor is maximum at zero-offset and it reduces with offsets;
- 3) Monitor PS amplitudes decreases than baseline;
- 4) For both baseline and monitor, PS reflection is practically zero for near offsets;
- 5) As we move too close to the well, both PP and PS reflections get mixed and contaminated.

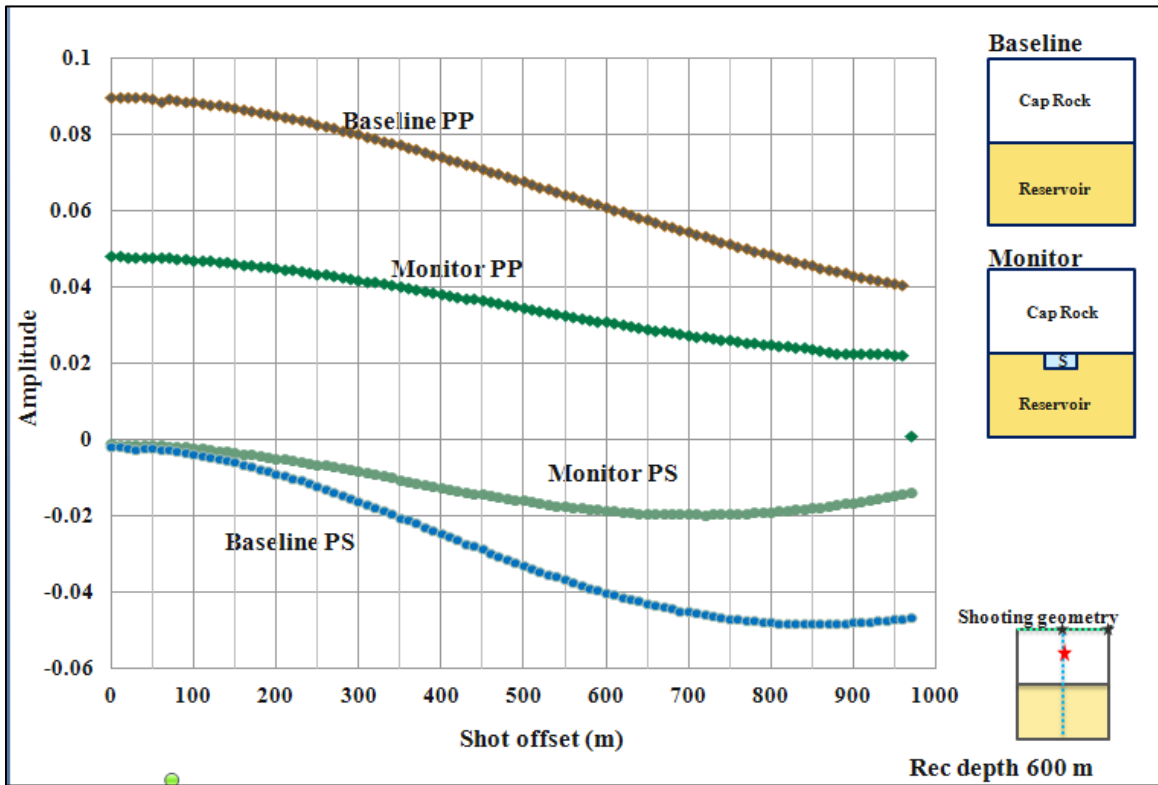


Figure 5.20: Amplitude for PP and PS for baseline and monitor plotted as a function of shot offset for receiver depth 600 m. Insets show a schematic diagram of the baseline and monitor models and shooting geometry.

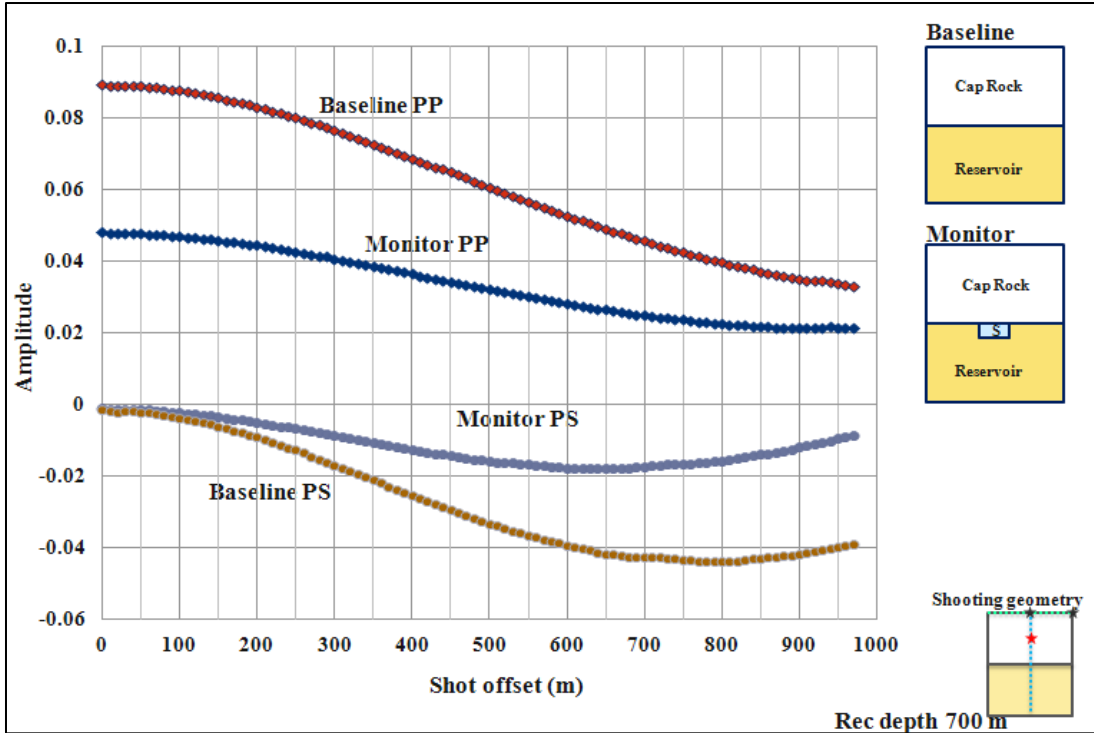


Figure 5.21: Amplitude for PP and PS for baseline and monitor plotted as a function of shot offset for receiver depth 700 m. Insets show a schematic diagram of the baseline and monitor models and shooting geometry.

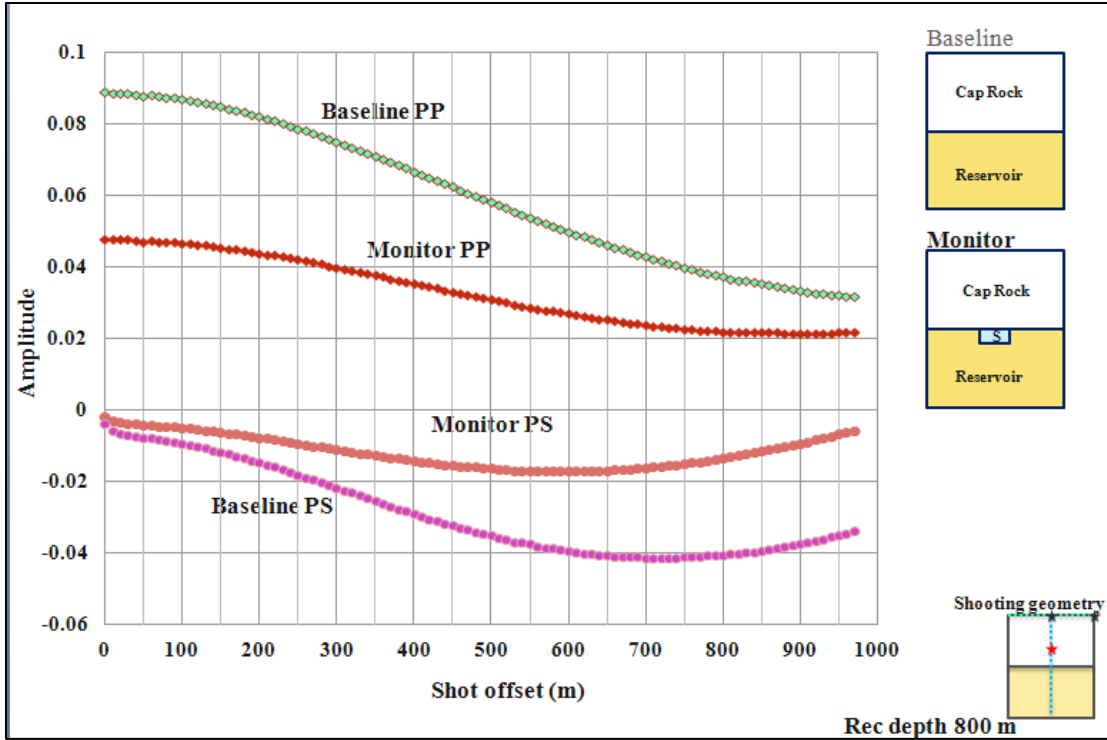


Figure 5.22: Amplitude for PP and PS for baseline and monitor plotted as a function of shot offset for receiver depth 800 m. Insets show a schematic diagram of the baseline and monitor models and shooting geometry.

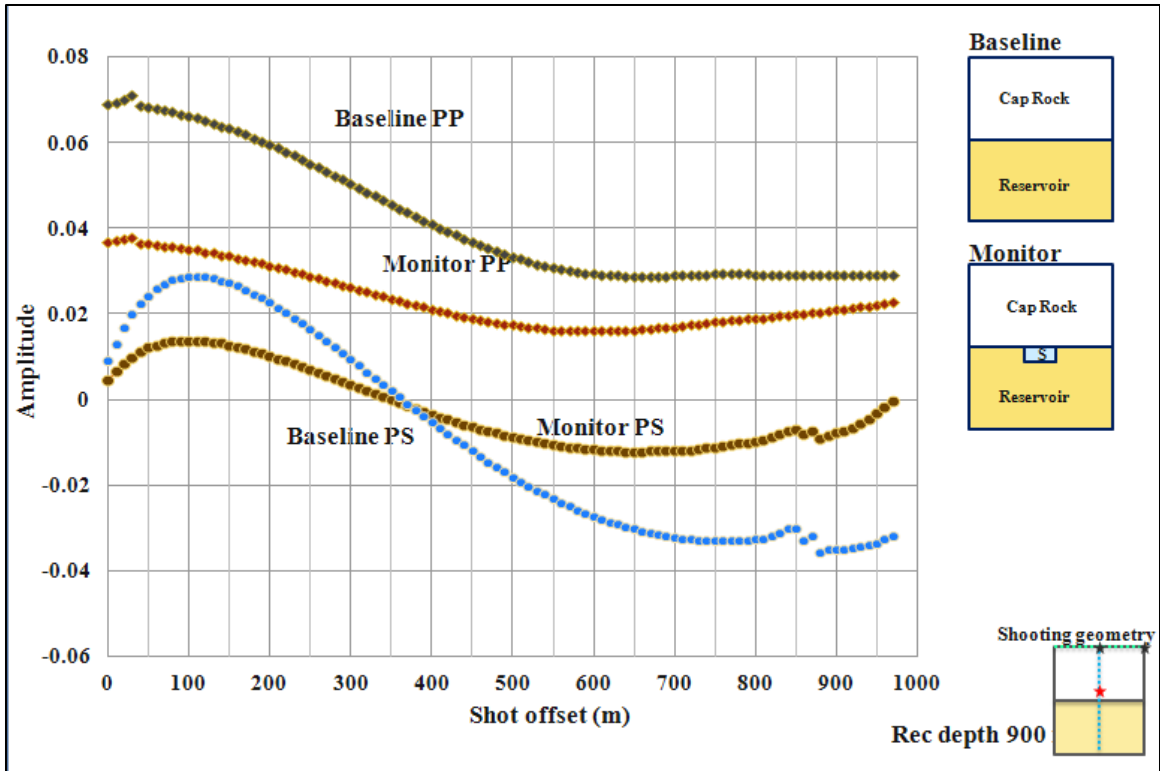


Figure 5.23: Amplitude for PP and PS for baseline and monitor plotted as a function of shot offset for receiver depth 900m. Insets show a schematic diagram of the baseline and monitor models and shooting geometry. Here extracted amplitudes are contaminated as the receiver is too close to the reflector.

## 5.9 Interpretation

In Figures 5.19 to 5.21, we plotted the amplitude responses for both PP and PS as a function of shot offset for various receiver depths. The two-layer model with initial reservoir parameter is taken as a baseline in this case because it replicates the scenario before the steam injection. We used the 50 m thick and 100 m wide (50 m each side of the well) with 50 percent steam saturation situation as our final monitor case.

We observe that the PP reflections are higher for baseline and dropped from 0.09 to 0.05 in monitor (almost about 50 percent) at zero-offset. The PP amplitude difference is higher at zero offset and gets lower as we reach far offset.

We also note that the reflection is weaker for monitor than baseline. At zero offset, they are the same and zero for obvious reasons. At mid offset, the monitor PS amplitude gets about 50 percent less negative than that of baseline.

The joint PP and PS inversion is a very useful tool to delineate density information. In the above-mentioned modeling, we saw that we had enough difference in both PP and PS reflections for a mid-offset dataset; therefore,  $\Delta PP$  and  $\Delta PS$  can be very useful in joint intersection.

## **5.10 Summary**

Steam injection rapidly changes the temperature of the surrounding area of the injector, which affects the  $V_P$  very strongly. Because of this, we do not have to wait for the steam chest to grow to see 4D effects in a PP TL image. But if we really want to see a map of the steam chest, we need to look at a PS difference map between baseline and monitor.

In this chapter, we developed a methodical approach to check PS amplitude behavior as the field matures in steam injection. It is wiser to generate multiple synthetic seismic with the help of well data and keep checking if the reservoir has reached the right combination of density and velocity changes due to steam injection. This would help to

maximize the chance of success in PS imaging and also provides a good way to optimize rig time.

## **Chapter Six: Conclusions and recommendations**

The goal of this dissertation has been to understand and analyze steam injection in a mature oil field in southern Oman. The approach we have used was to develop a complete workflow for quantitative reservoir characterization via VSP processing for steam monitoring.

For this pilot steam injection project, we considered it essential to understand the relationship between reservoir properties (such as permeability distribution) and seismic properties (reflectivity) and how this changes with steam injection (increasing temperature, pressure and saturation due to steam). We developed a methodical workflow to choose suitable permeability distributions and update existing initial reservoir models with the help of seismic sensitivity analysis and attribute studies. We have noted that these methods can be used as generic aid to reduce uncertainty of steam propagation prediction in the early stages of steam injection in a field with limited or no real data available.

We executed the workflow using synthetic data generated from an existing reservoir model. These different scenarios are different from each other in terms of their permeability distributions, but give similar temperature effects. The selection of the most suitable reservoir was possible after careful quantitative comparison, which yielded results that were counter-intuitive to initial observations. We established a quantitative CtL workflow to analyze six different reservoir models, then selected the most suitable reservoir model. We undertook two quantitative approaches for attribute comparison (the

similarity attribute and difference of RRR energy plot). We have observed that both work consistently with each other to identify the scenario that honors the data and hence provides an accurate representation of the subsurface.

There were only repeat temperature logs available from three observation wells from the injection area (the 1-acre hexagonal area around the injector); no repeat sonic logs were taken after the steam injection. We designed a full-wave walkway VSP with minimum model and predicted velocity and density change (-5 percent  $V_P$  and -2 percent density). We made these predictions using both Gassmann substitution and FLAG modeling. We successfully processed the synthetic VSP to investigate the seismic detectability of TL anomalies. We have also suggested various ways to increase the signal-to-noise ratio to enhance weak TL signals. The synthetic results were similar to the field VSP, which was processed afterwards. We performed theoretical calculations to see how the PS curves change with changing petrophysical parameters for smaller incident angles. We have indicated that VSP geometry does not provide larger angle coverage for AVO/A studies.

As there no velocity information was available from after the steam injection, it was difficult to predict changes in  $V_S$ . We found that Gassmann substitution does not work properly because the combined effect of changing temperature and pore-pressure provide a scope of error in  $\Delta V_S$  calculations. We investigated theoretical PS reflectivity for a series of scenarios where changes in  $V_S$  are positive (increased  $V_S$  according to Gassmann substitution) to negative (Kato's pore pressure effect). We have observed that, for PS reflectivity at smaller angle of incidence, the density effect of the reservoir

overrides the effect of  $V_S$ . For our study field in southern Oman, a 6 to 8 percent decrease in density was needed for measurable PS for walkaway VSP (offset to reflector depth is 1). We have also calculated that the minimum thickness of the steam layers needs to be more than 1/3 of the wavelength to expect a clear PS reflection from the top of the steam. We have also found the necessary stand-off distance of the receiver gather to be one wavelength above from the top of the steam to avoid mixed amplitudes. We have shown that a 6 percent decrease in density due to steam saturation would be sufficient for the study oil field in Oman to have sufficient changes in the PP and the PS amplitudes for joint inversion. After successful density inversion, the density information will be used to reinforce permeability pattern within the reservoir. This information further can be fed back to the current reservoir model for better simulation.

A summary of my conclusion includes the following:

1. Sensitivity analysis is done for six reservoir models with different density distribution; synthetic seismic section and TL attribute maps are generated for quantitative comparison;
2. Full waveform Walkaway VSP is generated; velocity and density changes due to steam injections are modeled using Gassmann and FLAG; a 5% P-wave velocity and 2% density decrease are sufficient to produce TL anomaly in migrated VSP sections;
3. Synthetic VSP shows a signature similar to field VSP; petrophysical property changes are sufficient for PP imaging; PS reflections were negligible;

4. Theoretical reflectivity study shows that for small angles of incidence (VSP geometry) a minimum of 6% density decrease is required for measurable changes in the PS reflection.

We also developed a diagram that explains one complete integrated loop (Figure 6.1). We believe this image serves as a good conclusion because it simply illustrates the processes undertaken in this study.

At Step I, the reservoir model is built using initial well and temperature data from the field. Several scenarios, which are the same as the reservoir models but have different permeability distributions, can provide similar initial temperature responses. We produced zero-offset synthetic seismic data and calculated TL attributes for six such scenarios and compared results. This quantitative comparison helped to choose a best-match scenario and was used to update the reservoir model in further studies.

In Step II, multi-offset time lapse VSP is generated. A repeat sonic velocity is recommended at this step, but simple model velocity can also work with some restrictions. After successful attempts to image the PP TL anomaly, a repeat field VSP should be ventured to optimize rig time in an onshore running production field like in Oman. Results from the field VSP will be helpful to update petrophysical information and some idea about permeability paths by looking at the trend of heat effect. At an early stage of steam injection, it's unlikely to develop an actual steam chest within the reservoir thus TL PP imaging is more helpful. The PS reflections for smaller angles will not be very useful. In this case, a larger angle gathers (wide azimuth surface seismic)

should work the best. But this Oman field is known for its bad surface seismic data quality due to near-surface complexity. Step III describes the scope of an extensive PS modeling. It is done and indicates desirable changes in petrophysical parameter needed for successful density inversion. Once the usefulness of the PS reflectivity is proved theoretically, it is recommended to repeat 3CVSP surveys after a reservoir has gone under sufficient steam injection to produce similar changes (marked in orange). This will help to produce a density map directly correlating with steam movement within the reservoir. This information will be used as the final ground truth which will be fed back to the reservoir model for final updating. The density map can be used for many other aspects for a steam injection feasibility study, such as position or need for new injector location, amount of steam, or need for artificial fracking.

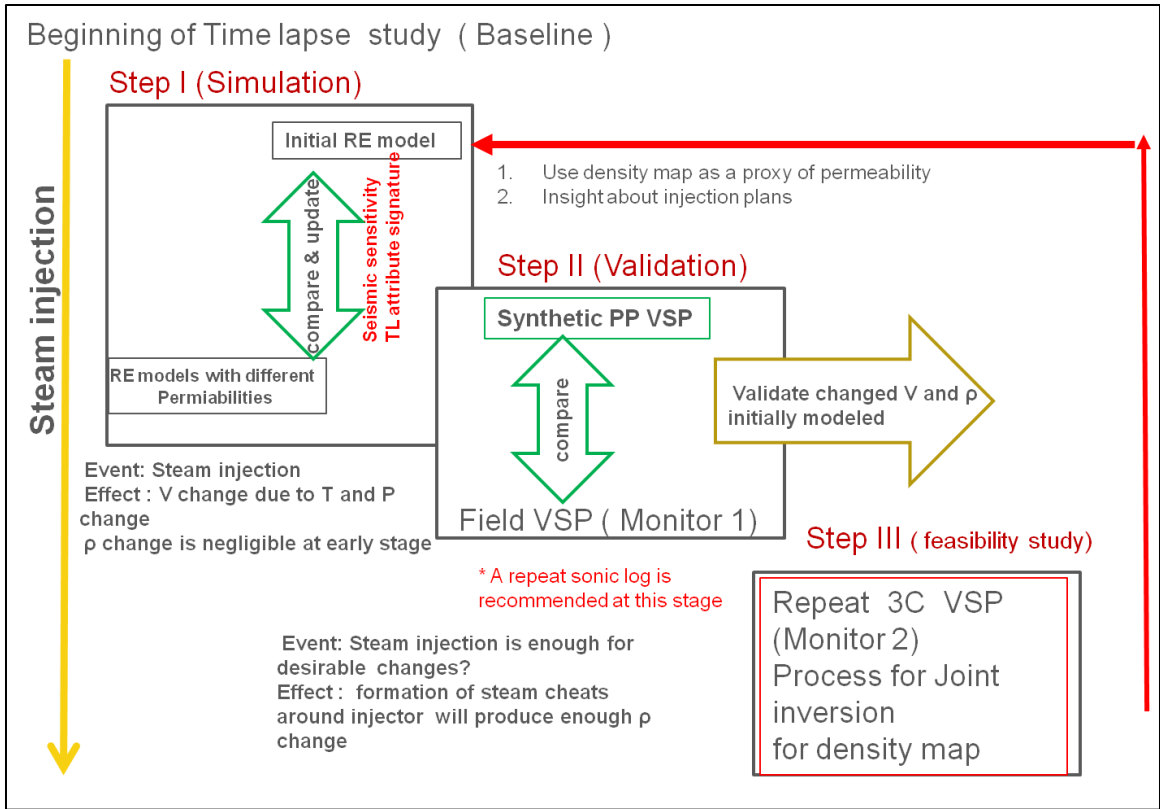


Figure 6.1: Integrated flowchart explaining reservoir model updating for TL.

## REFERENCES

- Aki, K., and P. G. Richards, 1980, Quantitative seismology: Theory and methods: W. H. Freeman and Company.
- Anderson, P. and F. Gray, 2001 Using LMR for dual attribute lithology identification. SEG Technical Program Expanded Abstracts, 201-202.
- Batzle, M., R. Hofmann, D.-H. Han, 2006, Heavy oils-seismic properties: The Leading Edge, **25**, 750-757.
- Castagna, J. P. M. L. Batzle, and R. L. Eastwood, 1985, Relationships between compressional-wave and shear-wave velocities in clastic silicate rocks: Geophysics, **50**, 571-581.
- Castagna, J. P., 1993, AVO analysis - Tutorial and review, *in* Castagna, J. P. and M. M. Backus, eds., Offset-dependent reflectivity - Theory and practice of AVO analysis: SEG, 3-36.
- Chopra, S., L. Lines, D Schmitt, and M Batzle, 2010, Heavy-oil reservoirs characterization and production monitoring, Society of Exploration Geophysicists
- DiSiena, J.P., Byun, B.S., Fix, J.E., and Gaiser, J.E., 1984, F-K analysis and tube wave filtering, *in* Toksoz, N.M. and Stewart, R.R., Eds., Vertical Seismic Profiling, Part B: Advanced Concepts: Geophysical Press.
- Eastwood, J., 1993, Temperature-dependent propagation of P-waves and S-waves in Cold Lake oil sands: Comparison of theory and experiment: Geophysics, **58**, 863-872.

- Eastwood, J., P. Lebel, A. Dilay, and S. Blakeslee, 1994, Seismic monitoring of steambased recovery of bitumen: The Leading Edge, **13**, 242-251.
- Eaton, D.W.S., R.R. Stewart and M.P. Harrison 1991. The Fresnel zone for P-SV waves. Geophysics, **56** (3), 360-364.
- Fomel, S., and L. Jin, 2009, Time-lapse image registration using the local similarity attribute: Geophysics, **74** (2), A7-A11
- Gardner, G. H. F., L. W. Gardner, and A. R. Gregory, 1974, Formation velocity and density-the diagnostic basics for stratigraphic traps: Geophysics, **39**, 770-780.
- Gassmann, F., 1951, Über die elastizität poröser medien: Vierteljahresschrift der Naturforschenden Gesellschaft in Zurich, **96**, 1–23.
- Han, D.-H., J. Liu, and M. Batzle, 2008, Seismic properties of heavy oils – Measured data: The Leading Edge, **27**, 1108-1115.
- Hardage, B.A., 1983, Vertical Seismic Profiling: Principles: Geophysical Press, 12-119.
- Hardage, B.A., 2001, Developments, trends and future directions in vertical seismic profiling and crosswell seismic profiling: Recorder, September, 72-78.
- Hashin, Z., and S. Shtrikman, 1963, A variational approach to the elastic behavior of multiphase materials: Journal of the Mechanics and Physics of Solids, **11**, 127-140.
- Hinds, R. C., and Kuzmiski, R.D., 1996, VSP interpretative processing: theory and practice: Society of Exploration Geophysicists, 56-67.

Hinds, R. C., and Kuzmiski, R.D., 2001, VSP for the interpreter/processor for 2001 and beyond: part 1: Recorder, 84-95.

Hughes Clarke, M.W., 1988, Stratigraphy and rock unit nomenclature in the oil-producing area of interior Oman, *Journal of Petroleum Geology*, **11**(1), 5-60.

Issac, J. H., 1996, Seismic methods for heavy oil reservoir monitoring: Ph.D. dissertation, University of Calgary.

Kato, A. and S. Onozuka, 2007, Oil sands rock physics databook in Hangingstone field: Japan Oil, Gas and Metals National Corporation.

Kato, A., S. Onozuka, and T. Nakayama, 2008, Elastic property changes in bitumen reservoir during steam injection: *The Leading Edge*, **27**, 1124-1131.

Kato, A., and D.-H. Han, 2009, Volume viscosity and it-induced bulk modulus of heavy oil: 71th Conference and Technical Exhibition, EAGE, Extended Abstract, Z023.

Kato, A., 2010, Reservoir characterization and steam monitoring in heavy oil reservoirs: Ph.D dissertation, University of Houston.

Kiyashchenko, D., and A. Maamari, 2010, 3DVSP and cross-well surveys for deep EOR target imaging in Oman: 80th Annual International Meeting, SEG, Expanded Abstracts, 4324-4328.

Kiyashchenko, D., K. Mehta, J. Lopez, A.Maamari, S.Busaidi, Y.Maskari, and G. Rocco: 2011, Time-lapse down-hole seismic surveys for deep EOR target monitoring in South Oman: 81th Annual International Meeting, SEG Expanded Abstracts, 4244-4248.

Koster, K., P.Gabriels, M. Hartung, J. Verbeek, G. Deinum, R. Staples, 2000, Time-lapse

seismic surveys in the North Sea and their business impact, *The Leading Edge*, **19(3)**, 286-293.

Kragh, E., and P. Christie, 2002, Seismic repeatability, normalized rms and predictability: *The Leading Edge*, **21**, 640–647.

Liu, J., 2006, Description of models used in the programs FLAG: 2006 annual meeting of Fluids/DHI consortium.

Lumley, D. E., Behrens, R. A., Wang, Z., 1997, Assessing the technical risk of a 4D-seismic project: *The Leading Edge*, **16(9)**, 1287-1292.

Marfurt, K. J. , R. L. Kirlinz, S. L. Farmer, M. S. Bahorich, 1998; 3-D seismic attributes using a semblance-based coherency algorithm, *Geophysics*, **63(4)**, 1150–1165.

Mavko, G., T. Mukerji, and J. Dvorkin, 1998, *The rock physics handbook*: Cambridge University Press, 389-391.

Mukherjee, T., K. Mehta, J. Lopez, R.R Stewart, 2012, Closing the Loop via scenario modeling in a time-lapse study of an EOR target in Oman: SEG technical program expanded abstracts, 1-5.

Nakayama, T., A. Takahashi, L. Skinner, and A. Kato, 2008, Monitoring an oil-sands reservoir in northwest Alberta using time-lapse 3D seismic and 3D P-SV converted-wave data: *The Leading Edge*, **27**, 1158-1175.

Nur, A., C. Tosaya, and D. V. Thanh, 1984, Seismic monitoring of thermal enhanced oil recovery processes: 54th Annual International Meeting, SEG, Expanded Abstracts, 118-121.

Pullin, N., Matthews, L., and Hirshe, K., 1987, Techniques applied to obtain very high

resolution 3-D seismic imaging at an Athabasca tar sands thermal plot: The Leading Edge, **6 (12)**, 10–15.

O'Brien, J., F. Kilbride, F. Lim, 2004, Time-lapse VSP reservoir monitoring, The Leading Edge, **23(11)**, 1178-84.

Rocco, G., R. Adavi, F. Kindy, S. Busaidi, S. Farsi, A. Maamari, P. Jorgensen, D. Kiyashchenko, K. Mehta, J. Lopez, and M. Zwaan, 2010, Steam development areal surveillance programme in Petroleum Development Oman: SPEEOR Conference at Oil and Gas West Asia, Society of Petroleum Engineers.

Stewart, R.R., 1984, VSP interval velocities from travelt ime inversion: Geophysical Prospecting, **32**, 608-628.

Stewart, R.R., 2001, VSP: An in-depth seismic understanding: Recorder, **7**, 79-83.

Stewart, R.R., and Di Siena, J.P., 1989, The values of VSP in interpretation: The Leading Edge, **8**,16-23.

Stewart, R. R., 1990, Joint P and P-SV inversion: The CREWES Research Report, **3**,112-115.

Sun, Z., 1999, Seismic methods for heavy oil reservoir monitoring and characterization: Ph.D. dissertation, University of Calgary.

Taner, M. T., F. Koehler, R. E. Sheriff, 1979, Complex seismic trace analysis, Geophysics, **44(6)**, 1041-1063.

Thomas S., F. Ali S.M., 1993, Field experience with chemical oil recovery methods, proceeding of the 21<sup>st</sup> Australian Chemical Engineering Conference (Chemeca 93), Melbourne, Australia, Sept. 26-29, 45-3-49-3.

Thomas S., 2008; Enhanced Oil Recovery – An Overview, Oil & Gas Science and Technology, **63 (1)**, 9-19

Traub, B., A. K. Nguen, and M. Riede, 2009, Fast free-surface multiples attenuation workflow for threedimensional ocean bottom seismic data: Geophysical Prospecting, **57**, no. 5, 785–802,

Toksöz, M.N., and Stewart, R.R., 1984, Vertical seismic profiling: advanced concept: Geophysical Press, 87-91.

Yilmaz, O., 2001, Seismic data processing: Society of Exploration Geophysicists

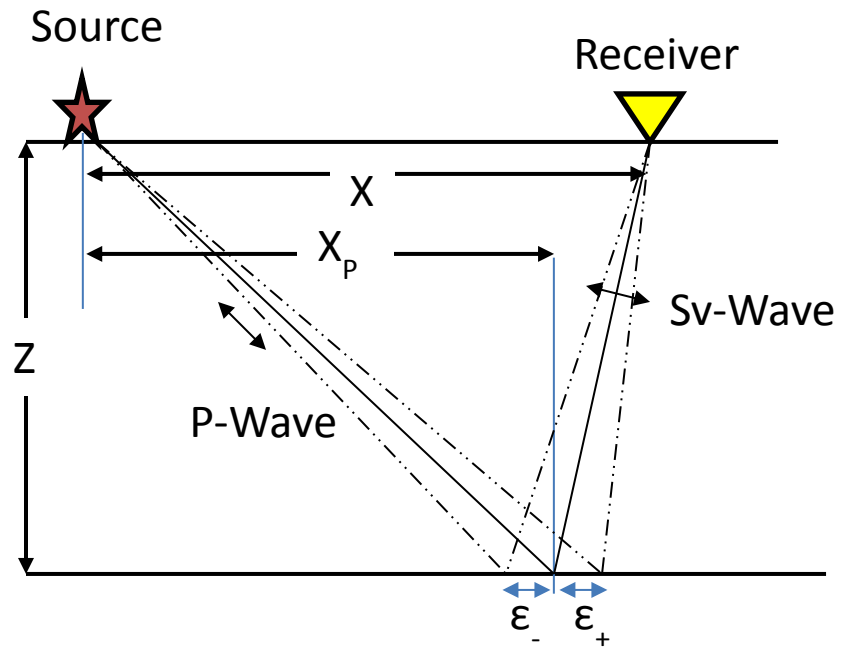
## Appendix A: Fresnel zone calculation

According to Eaton, *et al.* (1991), for a horizontal reflecting surface, the shape of the non-zero offset surface-to-surface Fresnel zone is ellipsoidal, with the long axis in the source-receiver plane. The inline Fresnel radii,  $\varepsilon_+$  and  $\varepsilon_-$  satisfy the equality

$$T/2 = \frac{[(x_p \pm \varepsilon_{\pm})^2 + Z^2]^{1/2} - (x_p^2 + Z^2)^{1/2}}{V_P} + \frac{[(x - x_p \pm \varepsilon_{\pm})^2 + Z^2]^{1/2} - [(x - x_p)^2 + Z^2]^{1/2}}{V_S}$$

where  $x_p$  is the offset of the mode-conversion point from the source. Similarly, the cross line  $P$ - $S$  Fresnel radius (denoted  $\varepsilon_x$ ) can be determined using

$$T/2 = \frac{(x_p^2 + \varepsilon^2 + Z^2)^{1/2} - (x_p^2 + Z^2)^{1/2}}{V_P} + \frac{[(x - x_p)^2 + \varepsilon^2 + Z^2]^{1/2} - [(x - x_p)^2 + Z^2]^{1/2}}{V_S}$$



Appendix A: Geometry and symbols used for calculating inline radii for the non-zero offset Fresnel zone (Eaton, *et al.*,1991).